Modelling of Thermal Radiation Exchange at Glass-Covered Greenhouse Surfaces under Different Climatic Conditions

Von der Naturwissenschaftlichen Fakultät
der Gottfried Wilhelm Leibniz Universität Hannover
zur Erlangung des Grades

Doktor der Gartenbauwissenschaften

- Dr. rer. hort. -

genehmigte Dissertation

von

Erick Kiplangat Ronoh, M.Sc. (Kenia)

geboren am 20.06.1982 in Sotik, Kenia

2016

"The formulation of a problem is often more essential than its solution, which may be merely a matter of mathematical or experimental skill. To raise new questions, new possibilities, to regard old problems from a new angle requires creative imagination and marks real advances in science."

— Albert Einstein (1879 - 1955), Physicist & Nobel Laureate

ABSTRACT

Modelling of thermal radiation exchange at glass-covered greenhouse surfaces under different climatic conditions

Precise determination of heat consumption in greenhouses requires accurate heat transfer models. Nowadays energy analysis in greenhouses is inadequate because it is based on an inaccurate overall heat transfer coefficient (U_{cs}-value). At the greenhouse surfaces, there is an interaction between radiative and convective heat transfer mechanisms. The relative contributions of these mechanisms to the U_{cs}-value need to be accurately determined. Therefore this study aims to model the thermal radiation exchange between glass-covered greenhouse surfaces and the sky considering representative test conditions under both day and night conditions.

The research work mainly focused on radiative heat transfers and their significance in the U_{cs}-value model. The investigations were done with a south-facing thermal box under outdoor conditions. In addition, four other thermal boxes were developed to check the effects of greenhouse surface inclination and orientation on the thermal radiation exchange. The surface design properties and meteorological data were necessary for the prediction of the thermal radiation at the study location. The interactions between the radiative and the convective heat transfers at the greenhouse surfaces are also quantified in this study.

If all the required parameters can be accurately determined, the prediction models provide a more realistic understanding of the radiation exchange at the exterior surfaces. Although the effect of orientation on the radiation exchange was negligible, the effect of surface inclination was evident especially on clear-sky nights. A strong interaction between the radiative and the convective heat transfers at the surface was found to be dependent on wind speed. Overall, the results form a basis for decisions on greenhouse design improvements and climate control interventions in the horticultural industry. The study also fills a knowledge gap in the U_{cs}-value model for greenhouse simulation.

Keywords: Greenhouse surfaces, sky, thermal box, thermal radiation exchange, model, U_{cs}-value, energy

ZUSAMMENFASSUNG

Modellierung des Austauschs von Wärmestrahlung an Gewächshausglasflächen unter verschiedenen Klimabedingungen

Eine präzise Bestimmung des Wärmebedarfs in Gewächshäusern erfordert genaue Wärmeaustauschmodelle. Die heutigen Energieverbrauchsanalysen sind ungenau, da sie auf den ungenauen Wärmeverbrauchskoeffizienten (U_{cs}-Wert) beruhen. An Gewächshausoberflächen gibt es eine Wechselwirkung zwischen strahlungsbedingten und konvektiven Wärmeübergängen. Ihr relativer Anteil am U_{cs}-Wert muss genauer ermittelt werden. Deshalb beschäftigt sich die vorliegende Arbeit mit der Modellierung des Austauschs von Wärmestrahlung zwischen den Glasoberflächen von Gewächshäusern und dem Himmel unter Berücksichtigung von repräsentativen Testbedingungen bei Tag und bei Nacht.

Der Schwerpunkt der Untersuchungen wurde hauptsächlich auf den Strahlungsaustausch und seine Bedeutung im U_{cs}-Modell gelegt. Die Versuche wurden mit Hilfe von einer südlich ausgerichteten Isolationsbox unter Außenbedingungen durchgeführt. Zusätzlich wurden vier weitere Isolationsboxen entwickelt, um die Einflüsse der Dachneigung und Flächenausrichtung auf den Strahlungsaustausch zu ermitteln. Die Oberflächenbeschaffenheit sowie meteorologische Daten waren für die Vorhersage der Wärmestrahlung am Standort notwendig. Die Wechselwirkung zwischen dem strahlungsbedingten und konvektiven Wärmeübergang an Bedachungsmaterialien wurde in dieser Arbeit ebenfalls quantifiziert.

Wenn alle benötigten Parameter genau bestimmt werden können, liefern die Vorhersagemodelle ein realistischeres Verständnis über den Strahlungsaustausch an Außenflächen. Obwohl der Einfluss der Himmelsrichtung auf den Strahlungsaustausch vernachlässigbar klein war, war der Neigungswinkel besonders an sternklaren Nächten offensichtlich von Bedeutung. Eine große Wechselwirkung zwischen dem strahlungsbedingten und konvektiven Wärmeübergang wurde in Abhängigkeit der Windgeschwindigkeit ermittelt. Zusammenfassend können die Ergebnisse dieser Arbeit bei der Entscheidung bezüglich des Gewächshausdesigns oder Klimaregelstrategien im

Gartenbau helfen. Durch die Untersuchungen konnte eine Wissenslücke im U_{cs}-Modell zur Gewächshausmodellierung geschlossen werden.

Schlagworte: Gewächshausoberflächen,   Himmel,   Isolationsbox,   Wärmeaustausch, Modell, U_{cs}-Wert, Energie

TABLE OF CONTENTS

SYMBOLS AND ABBREVIATIONS

(a) Symbols

Symbol	Description	Unit
a	factor splitting sky and ambient radiation	[-]
$a_0, a_1, ..., a_4$	empirical constants	[-]
A_s	total surface area	[m^2]
b	constant determined experimentally	[-]
b_0, b_1	coefficients determined experimentally	[-]
B	coefficient (Honsberg and Bowden, 2012)	[-]
c	coefficient determined experimentally	[-]
c_k	coefficient = 273.15 (Celsius to Kelvin)	[K]
C_1	coefficient = $3.74 \cdot 10^{-16}$ (Burke, 1996)	[W m^{-2}]
C_2	coefficient = $1.44 \cdot 10^{-2}$ (Burke, 1996)	[m K]
C	cloudiness factor	[-]
CF	correction factor	[-]
C_{maps}	cloudiness factor derived from analysed weather maps	[-]
C_{max}	maximum cloudiness factor	[-]
C_{min}	minimum cloudiness factor	[-]
C_{octas}	cloudiness factor derived from octas	[-]
C_{pa}	specific heat capacity of air	[J kg^{-1} K^{-1}]
d	constant determined experimentally	[-]
d_c	measuring distance of the camera	[m]
e_a	water vapour pressure of air	[Pa]
e_i	estimated value (radiation)	[-]
EoT	equation of time	[min]
f	frequency of photon	[s^{-1}]
F	geometrical factor	[-]
F_{air}	view factor to the air	[-]
F_d	diffuse fraction	[-]
F_{gnd}	view factor to the ground	[-]
F_{sky}	view factor to the sky	[-]
$grayval$	gray value of the region at any given time	[-]
$grayval_{max}$	maximum possible gray value = 256	[-]

$grayval_{offset}$	offset gray value of green background = 35	[-]
Gr	Grashof number	[-]
h	Planck's constant = $6.626 \cdot 10^{-34}$	[J s]
H_1	vertical distance from the lower hot plate	[m]
H_2	vertical distance from the upper cold plate	[m]
H_c	vertical height of camera from the surface	[m]
H_r	vertical height of net radiometers from the surface	[m]
H_t	hour of the day in 24 hour time	[h]
$I_{b,h}$	beam radiation on a horizontal surface	[W m^{-2}]
$I_{b,t}$	beam radiation on a tilted surface	[W m^{-2}]
I_c	clearness index	[-]
$I_{d,h}$	diffuse radiation on a horizontal surface	[W m^{-2}]
$I_{d,t}$	diffuse radiation on a tilted surface	[W m^{-2}]
$I_{e,h}$	extraterrestrial radiation on a horizontal surface	[W m^{-2}]
$I_{g,h}$	terrestrial global radiation on a horizontal surface	[W m^{-2}]
$I_{gr,h}$	ground reflected radiation from a horizontal surface	[W m^{-2}]
$I_{gr,t}$	ground reflected radiation on a tilted surface	[W m^{-2}]
I_n	extraterrestrial radiation on a plane normal to radiation	[W m^{-2}]
$I_{ref,t}$	reflected radiation from a tilted surface	[W m^{-2}]
I_{sc}	solar constant = 1367 (Sukhatme, 2003; Iqbal, 1983)	[W m^{-2}]
$I_{t,t}$	total solar radiation on a tilted surface	[W m^{-2}]
k_a	thermal conductivity of air	[W m^{-1} K^{-1}]
L	characteristic length of the solid surface	[m]
L_d	day length	[h]
L_{loc}	longitude of the location	[°]
L_{st}	standard meridian for local time zone	[°]
LST	local solar time	[-]
LT	local time	[-]
LWR_d	downwelling longwave radiation	[W m^{-2}]
$LWR_{d,t}$	total downwelling longwave radiation	[W m^{-2}]
LWR_u	upwelling longwave radiation	[W m^{-2}]
$LWR_{u,t}$	total upwelling longwave radiation	[W m^{-2}]
m_i	measured value (radiation)	[-]
n	number of observations	[-]

n_d	day of the year	[day]
Nu	Nusselt number	[-]
p	value for testing a statistical hypothesis	[-]
P_d	partial water vapour pressure	[hPa]
Q_{ar}	ambient radiation reflected by the object	[W m^{-2}]
Q_{cv}	heat loss by convection	[W]
Q_{dr}	direct radiation of the measured object	[W m^{-2}]
Q_l	heat flux by air exchange through leakage	[W]
Q_{lir}	heat loss by longwave infrared radiation	[W]
Q_{LW}	pyrgeometer irradiance	[W m^{-2}]
Q_n	emitted radiation normal to the surface	[W m^{-2}]
Q_p	energy of a photon	[J]
Q_{pr}	characteristic radiation of the air path	[W m^{-2}]
Q_{rad}	net flux density from the surface	[W m^{-2}]
Q_s	thermal radiation exchange of the surface	[W m^{-2}]
$Q_{s,eff}$	effective thermal radiation exchange	[W m^{-2}]
$Q_{s,g}$	thermal radiation exchange of glass	[W m^{-2}]
$Q_{s,gb}$	thermal radiation exchange of glazing bars	[W m^{-2}]
Q_{sky}	sky thermal irradiance	[W m^{-2}]
Q_{sw}	pyranometer irradiance	[W m^{-2}]
Q_t	total radiation measured by the thermal camera	[W m^{-2}]
Q^*	amount of radiation emitted by a blackbody	[W m^{-2}]
Q_λ	radiation emitted by the surface at a specific wavelength	[W m^{-2}]
Q_λ^*	blackbody radiation emitted at a specific wavelength	[W m^{-2}]
Q_θ	emitted radiation at an angle θ	[W m^{-2}]
R	thermistor resistance	[Ω]
R^2	coefficient of determination	[-]
R_{cv}	heat resistance due to convection	[m^2 K W^{-1}]
Re	Reynolds number	[-]
RH	relative humidity	[%]
R_l	heat resistance due to leakage	[m^2 K W^{-1}]
R_{lir}	heat resistance due to longwave radiation	[m^2 K W^{-1}]
R_n	net radiation	[W m^{-2}]
$R_{n,lw}$	net longwave radiation	[W m^{-2}]

$R_{n,sw}$	net shortwave radiation	[W m^{-2}]
R_λ	heat resistance due to conduction	[m^2 K W^{-1}]
S	sensitivity	[µV W^{-1} m^2]
SI	sensitivity index	[-]
T	absolute temperature	[K]
T_1	absolute temperature of surface 1	[K]
T_2	absolute temperature of surface 2	[K]
T_a	absolute air temperature	[K]
T_b	pyrgeometer body temperature	[K]
T_c	temperature of cold plate	[K]
T_d	dew point temperature	[K]
T_g	temperature of the glass surface	[K]
T_{gb}	temperature of the glazing bar surface	[K]
T_{gnd}	ground temperature	[K]
T_h	temperature of hot plate	[K]
T_e	environmental temperature	[K]
T_i	inside temperature	[K]
T_o	object temperature	[K]
T_p	air path temperature	[K]
T_s	surface temperature	[K]
$T_{s,eff}$	effective surface temperature	[K]
T_{sky}	sky temperature	[K]
TC	time correction factor	[min]
U	heat transfer coefficient for heat loss through the material	[W m^{-2} K^{-1}]
U_{cs}	overall heat transfer coefficient (U_{cs}-value)	[W m^{-2} K^{-1}]
$U_{cs,n}$	new corrected U_{cs}-value	[W m^{-2} K^{-1}]
$U_{cs,sfg}$	greenhouse U_{cs}-value for a single float glass	[W m^{-2} K^{-1}]
$U_{cs,st}$	standard greenhouse U_{cs}-value at 4 m s^{-1} wind speed	[W m^{-2} K^{-1}]
$U_{cs,v}$	wind-corrected U_{cs}-value	[W m^{-2} K^{-1}]
U_{cv}	convective heat transfer coefficient	[W m^{-2} K^{-1}]
U_l	heat transfer coefficient for heat loss through air leakage	[W m^{-2} K^{-1}]
U_{lir}	radiative heat transfer coefficient	[W m^{-2} K^{-1}]
v	wind speed	[m s^{-1}]
v_{10}	wind speed at 10 m above the ground	[m s^{-1}]

v_s	wind speed close to the wall surface	[m s^{-1}]
V_{emf}	output voltage	[µV]
V_{gi}	inner volume of greenhouse model	[m^3]
V_p	output voltage of a propeller anemometer	[mV]
x_1, x_2, x_3	coefficients (Chen et al., 1995)	[°C^{-1}]
$x_{a,1}, x_{a,2}, x_{a,3}$	coefficients (von Elsner, 1982; Dingman, 2009)	[°C]
$x_{b,n}$	coefficients (n = 1, 2, 3, 4) (sources differ)	[K^4]
$x_{c,1}$	coefficient = 0.0552 (Nijskens et al., 1984)	[K$^{-1.5}$]
$x_{c,2}$	coefficient = 5.6 · 10^{-3} (Berdahl and Martin, 1984)	[K^3]
$x_{c,3}$	coefficient = 7.3 · 10^{-5} (Berdahl and Martin, 1984)	[K^2]
$x_{d,1}$	coefficient = 15 (Berdahl and Martin, 1984)	[° h^{-1}]
$x_{d,2}$	coefficient = 4 (Goswami et al., 2000)	[° min^{-1}]
x_l	coefficient = 1000 (Varioscan Manual, 2000)	[m]
x_λ	coefficient = 2897 (Howell et al., 2011)	[µm K]
$x_{m,1}, x_{m,2}, x_{m,3}$	coefficients (Honsberg and Bowden, 2012)	[min]
$x_{n,1}, x_{n,2}, x_{n,3}$	coefficients (Duffie and Beckman, 1991; Sukhatme, 2003)	[day]
x_p	coefficient = -0.095 (Tantau, 1975)	[hPa^{-1}]
$x_{r,n}$	coefficients (n = 1, 2, 3, 4) (sources differ)	[°]
$x_{t,1}, x_{t,2}$	coefficients (Abdullah and Ali, 2012; FAO, 1998)	[h]
$x_{t,3}$	coefficient = 60 (Honsberg and Bowden, 2012)	[min h^{-1}]
$x_{t,4}$	coefficient = 3600 (Tantau, 2013)	[s h^{-1}]
x_{tr}	coefficient = 100 (Kipp & Zonen, 2009)	[Ω]
$x_{u,n}$	coefficients (n = 1, 2, 3, ……, 12) (sources differ)	[W m^{-2} K^{-1}]
$x_{v,1}$	coefficient = 0.35 (Rath, 1992)	[s m^{-1}]
$x_{v,2}, x_{v,3}$	coefficients (empirical)	[s m^{-1}]
x_w	coefficient = 0.018 (Manual PN 27005-90, 1994)	[m s^{-1} mV^{-1}]
$x_{w,n}$	coefficients (n = 1, 2, 3, ……, 9) (sources differ)	[W s m^{-3} K^{-1}]
X_b	base value of parameter	[-]
X_s	site-dependent coefficient (Iziomon et al., 2003)	[-]
y_0	coefficient = 100 (Kimball et al., 1982; other sources)	[%]
$y_{c,n}$	coefficients (n = 1, 2, 3, ……, 13) (sources differ)	[-]
$y_{d,1}, y_{d,2}$	coefficients ((Swinbank, 1963; Idso and Jackson, 1969)	[K^{-2}]
$y_{p,1}$	coefficient = 610.8 (Dingman, 2009)	[Pa]
$y_{p,2}$	coefficient = 0.643 (Brutsaert, 1975)	[K$^{1/7}$ Pa$^{-1/7}$]

$y_{p,3}$	coefficient = $5.95 \cdot 10^{-7}$ (Idso, 1981)	[Pa^{-1}]
$y_{p,4}$	coefficient = 0.714 (Sugita and Brutsaert, 1993)	[K$^{0.0687}$ Pa$^{-0.0687}$]
$y_{p,5}$, $y_{p,6}$	coefficients (Prata, 1996)	[K Pa^{-1}]
$y_{p,7}$	coefficient = 0.625 (Duarte et al., 2006)	[K$^{0.131}$ Pa$^{-0.131}$]
$y_{p,8}$	coefficient = 0.576 (Kruk et al., 2010)	[K$^{0.202}$ Pa$^{-0.202}$]
$y_{p,9}$	coefficient = 0.6905 (Dos Santos et al., 2011)	[K$^{0.0881}$ Pa$^{-0.0881}$]
$y_{t,1}$, $y_{t,2}$	coefficients (Idso and Jackson, 1969; Idso, 1981)	[K]
$y_{u,1}$	coefficient = 4.17 (Kanthak, 1970)	[W s$^{0.72}$ m$^{-2.72}$ K^{-1}]
$y_{u,2}$	coefficient = 1.32 (Kittas, 1986)	[W m^{-2} K$^{-1.25}$]
$y_{u,3}$	coefficient = 3.12 (Kittas, 1986)	[W s$^{0.8}$ m$^{-2.8}$ K^{-1}]
$y_{u,4}$	coefficient = 6.76 (Papadakis et al., 1992)	[W s$^{0.49}$ m$^{-2.49}$ K^{-1}]
$y_{u,5}$	coefficient = 4.78 (Emmel et al., 2007)	[W s$^{0.71}$ m$^{-2.71}$ K^{-1}]
$y_{u,6}$	coefficient = 1.84 (Suhardiyanto and Romdhonah, 2008)	[W s$^{0.33}$ m$^{-2.33}$ K^{-1}]
$y_{u,7}$, $y_{u,8}$	coefficients (empirical)	[W s^2 m^{-4} K^{-1}]
Y_b	base value of dependent variable	[-]
Y_s	site-dependent coefficient (Iziomon et al., 2003)	[K hPa^{-1}]
z_0	coefficient = 5 (Kimball et al., 1982)	[% °C^{-1}]
z	air exchange rate due to leaks	[h^{-1}]
α	solar altitude	[°]
α_{pt}	constant = $3.908 \cdot 10^{-3}$ (Kipp & Zonen, 2009)	[-]
α_s	albedo of the earth surface	[-]
α_λ	absorptivity at a given wavelength	[-]
β	inclination angle of surface from horizontal	[°]
β_{pt}	constant = $-5.8019 \cdot 10^{-7}$ (Kipp & Zonen, 2009)	[-]
δ	angle of declination	[°]
ΔC	difference in cloudiness factors	[-]
ΔT	air temperature difference between inside and outside	[K]
$\Delta T_{s\text{-}a}$	surface-to-air temperature difference	[K]
$\Delta T_{W\text{-}R}$	deviation between $\Delta T_{s\text{-}a}$ values of the wall and the roof	[K]
$\Delta U_{cs,st}$	difference in standard greenhouse U_{cs}-values	[W m^{-2} K^{-1}]
Δv	difference in wind speeds	[m s^{-1}]
$\Delta X_{b,i}$	change in parameter from base value	[-]
$\Delta Y_{b,i}$	change in dependent output state variable	[-]
ε	emissivity	[-]

ε_1	emissivity of surface 1	[-]
ε_2	emissivity of surface 2	[-]
ε_{12}	effective emissivity between the surfaces	[-]
ε_a	effective atmospheric emissivity	[-]
ε_{cs}	clear-sky atmospheric emissivity	[-]
ε_o	object emissivity	[-]
ε_s	surface emissivity	[-]
ε_{sky}	sky emissivity	[-]
ε_{gnd}	emissivity of surrounding ground objects	[-]
ε_λ	wavelength-dependent emissivity	[-]
γ	solar azimuth angle	[°]
λ	wavelength	[m]
λ_{max}	maximum wavelength	[µm]
ω	hour angle	[°]
ω_1	hour angle at time 1	[°]
ω_2	hour angle at time 2	[°]
ω_s	sunset hour angle	[°]
Φ	tilt angle of surface from vertical plane	[°]
φ	latitude	[°]
Ψ_b	beam radiation conversion factor	[-]
Ψ_d	diffuse radiation conversion factor	[-]
Ψ_r	ground reflected radiation conversion factor	[-]
ρ_a	density of air	[kg m^{-3}]
ρ_g	ground reflectivity	[-]
σ	Stefan-Boltzmann constant = $5.67 \cdot 10^{-8}$	[W m^{-2} K^{-4}]
τ_p	transmission of the air path	[-]
θ	angle of incidence	[°]
θ_{dp}	dew point temperature	[°C]
θ_o	outside air temperature	[°C]
$\theta_{s,app}$	apparent surface temperature	[°C]
θ_z	zenith angle	[°]
υ	hour from midnight	[h]

(b) Abbreviations

Abbreviation	Description
AC	alternating current
AMSL	above mean sea level
ANOVA	analysis of variance
ASTM	American Society for Standards and Measurement
BIAS	bias
DIN	Deutsches Institut für Normung e.V.
DC	direct current
DWD	Deutscher Wetterdienst
ETFE	ethylene tetrafluoroethylene
IMUK	Institut für Meteorologie und Klimatologie
IR	infrared radiation
MAE	mean absolute error
NIR	near infrared
NOAA	National Oceanographic and Atmospheric Administration
NTC	negative temperature coefficient
OAT	one-at-a-time
PAR	photosynthetic active radiation
PE	polyethylene
PMMA	polymethyl methacrylate
PMRE	percentage mean relative error
PVC	polyvinyl chloride
RGB	colour model (red, green and blue colours)
RMSE	root mean square error
Stdev	standard deviation
UV	ultraviolet
UVW	orthogonal wind vectors (U: middle, V: bottom, W: top)
VA	volt-ampere
WebWerdis	web weather request and distribution system

LIST OF FIGURES

LIST OF TABLES

1 INTRODUCTION

Modern protected cultivation is currently faced with a crisis of high energy costs which compromise the profitability of horticultural farming. The protected cultivation is a requirement for an environmentally friendly year-round production. This kind of production has been ascertained to be a highly competitive and profitable sector of agriculture in most countries. During cold seasons, night temperatures and even day temperatures can sink below the biological optimum necessary for sustainable cultivation of a healthy crop (von Zabeltitz, 2011). This is predominant in Europe during winter seasons. Greenhouses are therefore heated in such cases to generate and maintain warmer climate within itself. The production during winter season therefore allows an extension of the cropping period (Tantau, 2013). With increasing energy prices, the related energy costs due to heating of greenhouses during extreme cold seasons significantly contribute to high production costs. According to Sanford (2011), these energy costs represent more than 10 % of greenhouse growers' sales.

Greenhouses are built with different covering materials and designed to fit the local climate (von Elsner et al., 2000). The amount of heat lost through a covering material is usually the main challenge in a greenhouse heating system. The heat retaining properties of the covering system during long nights and cloud-covered days of the cold season are particularly important (Giacomelli and Roberts, 1993). The energy saving potential can therefore be realized by using cover materials which possess good heat insulation characteristics (Basak et al., 2015). They should also be transparent to the visible radiation and opaque to the infrared radiation component (Papadakis et al., 2000). Apart from the cover material, the climatic conditions inside these greenhouses also directly depend upon the thermal radiation intensity, the ambient air temperature, the overall heat transfer coefficient (U_{cs}-value) and the external wind speed (Mashonjowa et al., 2012).

Greenhouses, in general, exhibit a greater degree of thermal radiation interaction with the surroundings than other buildings (Chandra, 1982). A number of greenhouse thermal environment analyses have handled the thermal radiation exchange in different ways (Chandra, 1982; Jolliet et al., 1991; Al-Mahdouri et al., 2014). The thermal radiation dominates the heat transfer mechanisms especially between the cover material surface

and the surrounding atmosphere. The precise determination of the radiation components is essential for a good estimate of the net radiation balance and, consequently, of the radiation and energy balances (Duarte et al., 2006). The radiation balance, the main source of energy available for the physical and biological processes, is the essential component of the energy balance at the surface. With availability of hydro-meteorological data such as air temperature, relative humidity and cloudiness, the longwave radiation can be estimated for any location and at any given time. The understanding of the factors which control the ascending and descending flows in the atmosphere is essential to improve the models used in the various environmental applications (Araújo et al., 2012).

It is desirable to use basic heat transfer principles in adequate representation of the thermal radiation exchange between a greenhouse and its surroundings. Whereas several studies have been conducted on heat transfer measurements, most of the researches have not clearly shown the influence of the thermal radiation on the U_{cs}-value under outdoor conditions. In addition, the impacts of climatic variables on such actual conditions have not been well elucidated (Ajwang, 2005), thus making the accurate prediction of the U_{cs}-value impossible. The standard U_{cs}-values of elements (e.g. greenhouse roofs and walls) represent practical conditions as far as possible. However, the standard U_{cs}-values will not agree exactly with the values measured on site. Building regulations and codes often use the U_{cs}-values to specify targets and limits for thermal insulation and energy use (McMullan, 2012). In greenhouses, the comprehensive U_{cs}-value for any application (roof or wall) should be achieved. The distinct roof and wall U_{cs}-values need to be corrected for the wind and sky conditions. At different surface inclinations and orientations, accurate radiation data and models for the external thermal radiation exchange at representative conditions are therefore required. Additionally, at the greenhouse surfaces, it is necessary to take into account the combined effect of radiation and convection on the greenhouse heat losses. This enhances precise evaluation of the thermal needs (Jolliet et al., 1991). As a result, proper understanding and quantification of the contributions of the radiative and convective heat transfer mechanisms to the U_{cs}-value are critical and hence the need for the present study.

2 LITERATURE REVIEW

2.1 Greenhouse Structures

2.1.1 Types and designs

The efficiency and productivity of a greenhouse operation is largely dependent on the type of growing structure used. If only a single greenhouse is required, it can be built as a stand-alone unit. However, when multiple houses are needed (either initially or as part of a future expansion) the greenhouses should be gutter-connected for more efficient use. Greenhouse construction and operation has developed considerably during the last decades and several greenhouse designs are currently in use. The microclimate inside the greenhouse depends on the outside climatic conditions, the heating system and losses through the cover material due to thermal radiation, conduction, convection and latent heat processes (Geoola et al., 2009). Most of the available greenhouse designs in Europe follow the corresponding national standards and codes of practice (prEN 13031-1, 1997). This development is an attempt to standardize the greenhouse design methodology for commercial production at European level (von Elsner et al., 2000). A wide-span greenhouse is conventional in construction, i.e. with steel or aluminium purlins attached to steel trusses. These purlins together with the steel or aluminium gutter support the glazing bars on which glass is placed. A characteristic feature of the wide-span greenhouse is a continuous ventilation-window over the entire length of the roof. The advantages of a wide-span greenhouse are the bigger area without columns (better mechanization-possibilities), and the better ventilation capacity (von Elsner et al., 2000).

The Venlo-type greenhouse is the most popular design in The Netherlands. It was named after the Dutch town Venlo, where it first appeared (von Elsner et al., 2000). Here only one standard glass pane is placed on glazing bars covering the height from gutter to ridge. The standard bay width of 4 m enhances maximum light levels. Recent Venlo designs have increased heights (above 5 m) for better air movement and in order to create space for crops, thermal screens and light fittings for artificial lighting (van de Braak, 1995). Many German growers favour the Venlo-type greenhouses because they are lighter and cheaper. They are also standardized to a large degree and as a result, their construction and maintenance is easier and cheaper (von Elsner et al., 2000). According to the revised DIN 11535-2 code for the German standard greenhouse (DIN 11535-2, 1994), the main

advances in technology were incorporated and it includes 24° and 26.5° pitch angles of the roof for Venlo-type and wide-span greenhouses, respectively (von Elsner et al., 2000). It also takes into account the possibility of using aluminium as the frame material.

2.1.2 Orientation

A lot of emphasis internationally is placed on a greenhouse orientation that maximizes light interception. Generally, single-span greenhouses are oriented such that the length runs east-west. This orientation maximizes winter sunlight and heat gain in the greenhouse (Sanford, 2011). On the other hand, gutter-connected greenhouses are oriented with the length running north-south. According to Sanford (2011), this ensures that the shadow cast by the gutters moves during the day. If the orientation is east-west in this case, the shadow of the gutter will move very little, resulting in less direct sunlight and thus slowing down the plant growth. Spatial irregularities of irradiance with east-west oriented greenhouses could often be a problem at all latitudes (Gupta and Chandra, 2002). Generally, a specific orientation is suitable for a given purpose and location.

2.2 Greenhouse Cover Surfaces

2.2.1 Covering material

The cover surface is one of the component systems for the greenhouse design. The selection of a covering is crucial for attainment of an optimal controlled environment, particularly relating to the solar radiation intensity and wavelengths. The selection of specific covering alternatives has implications for the greenhouse superstructure and its enclosed crop production system (Giacomelli and Roberts, 1993). The selection of the cover material (generically called glazing, a derivation from the traditional use of glass as the covering material) has a tremendous influence on the crop production capability of the greenhouse system (Giacomelli and Roberts, 1993). Covering materials impact on the level and quality of light available to the crop. In conventional greenhouses, the glazing or covering materials are typically glass, rigid clear plastic or polyethylene. The covering materials for the "commercially built" greenhouses are glass or plastic whereas the covering material for the grower-built greenhouses is almost exclusively plastic film (von Elsner et al., 2000). In general, polyethylene (PE) film is the predominant covering material for all categories (Briassoulis et al., 1997a, 1997b; Tsirogiannis, 1996). A poorly

maintained covering material can lose a lot of energy and significantly increase production costs. There is therefore a growing interest in adoption of greenhouse cover materials which save energy without significantly affecting the crop productivity.

Many new greenhouse cover materials have thus emerged in recent decades. The greenhouses covered with plastic film are extensively common especially in countries with warm climates. They are mainly used for unheated production of vegetables, summer flowers, shrubs and tree nurseries. Plastic-covered greenhouses have undergone several stages of development and remain cheaper than glass types. With the design following certain specifications, they provide important advantages with respect to their functionality (von Elsner et al., 2000). The weatherability of plastic films is being enhanced by ultraviolet (UV) radiation degradation inhibitors, infrared (IR) radiation absorbency, anti-condensation drip surfaces, and unique radiation transmission properties (Giacomelli, 1999). The use of photo-selective films as greenhouse covers has several benefits. Reducing the intensity of near infrared (NIR) radiation (wavelength: 700 nm to 2300 nm) transmitted into a greenhouse contributes significantly to reducing the greenhouse heat load (Hemming et al., 2006). Unfortunately, most of the shading paints that reduce NIR transmission have been shown to significantly reduce the intensity of photosynthetic active radiation (PAR) of wavelength 400 nm to 700 nm (von Elsner, 2006; Mutwiwa, 2007) hence may influence yield. Moreover, blocking the transmission of UV radiation (wavelength: 300 nm to 400 nm) has been reported to enhance the performance of non-chemical plant protection methods (Doukas and Payne, 2007).

Glass has been the traditional greenhouse covering material in Europe even before the introduction of plastic covering materials. It is widely used in cold frames and greenhouses because of its ideal properties of transmitting sunlight and absorbing terrestrial (infrared) radiation (Kacira, 2012). In addition, it has very low degradation due to environmental causes and agrochemicals. The high transmittance glass is also resistant to the UV radiation. An aluminium frame covered with a glass covering provides a maintenance-free, weather-tight structure that minimizes heat costs and retains humidity. Modern glass types consider the need for minimizing energy consumption during cold periods without necessarily reducing the light transmittance (Max et al., 2012). Glass is

available in many forms that would be suitable with almost any style or architecture. Glass-covered greenhouses are mostly of wide-span or Venlo design types. However, glass used as a single layer has the disadvantage of high heat loss (Sanford, 2011). It is also heavy and requires a more expensive structure to support its weight.

The relationship between specific thermal performance of the covering materials of greenhouse systems and energy consumption are useful for energy efficient greenhouse production throughout the year. Overall, the characteristics of the commonly used greenhouse covering materials are presented in Table 2.1. The selected rigid cover materials include horticultural glass, reinforced polyester, bioriented polyvinyl chloride (PVC), double polymethyl methacrylate (PMMA) and double PVC.

Table 2.1. Characteristics of the common rigid materials used as greenhouse covers.

Property	Glass	Reinforced polyester	Bioriented PVC	Double PMMA	Double PVC
Thickness [mm]	4	1	0.9	16	6
Weight [kg m^{-2}]	10	1.5	1.45	5	1.4
Inflammability [-]	No	Easy	No	Medium	Medium
PAR transmissivity [%]	90	80-85	79-85	82	75-80
Longwave IR transmissivity [%]	1	4	1-2	2	5
Durability [years]	≥20	10	10	20	10

(Source: CPA, 1992)

2.2.2 Glazing bars

The technique of securing glass to the superstructure is known as glazing. The greater number and size of the glazing support bars are generally required for glazings that are heavy, less flexible, and have a small unit size and low bending strength. Thus a relatively heavy covering of narrow width, such as glass, would require a greater proportion of supports than a light-weight film or structured panel glazing. In addition, the unit size of the glazing material will also influence infiltration energy losses. A smaller unit width provides a greater proportion of edges that must be kept sealed to prevent infiltration (Giacomelli and Roberts, 1993). Glazing bars are commonly used in the reinforcement of

the glass-covered greenhouses. However, their influence on the heat transfer processes has not been considered in detail.

2.3 Heat Transport Mechanisms at Greenhouse Surfaces

2.3.1 Modes of heat loss

Heat loss from a greenhouse usually occurs by all three modes of heat transfer: conduction, convection and radiation. Usually many types of heat exchange occur simultaneously. Conduction is the transfer of heat occurring through intervening matter without bulk motion of the matter. It occurs when there is a temperature gradient across a body. In this case, the energy is transferred from a high temperature region to low temperature region due to random molecular motion. The rate of conduction between two objects depends on the area, path length, temperature difference and physical properties of the substance(s) (Worley, 2014). For glass greenhouses, conduction involves the movement of heat energy through the glass and frame materials from the air on the warmest side to the air on the colder side. The greater the difference in temperatures, the more the heat flow (Taha, 2003; Meyer, 2010). When a fluid (e.g. air or a liquid) is heated, it carries the thermal energy in the form of convection. Thermal radiation generates from the emission of electromagnetic waves which carry the energy away from the emitting object. Radiation occurs through a vacuum or any transparent medium (Gonzalez, 2015).

2.3.2 U_{cs}-value model

Heating is a major concern to commercial greenhouse producers. This is due primarily to the costs involved in the purchase and operation of heating equipment as well as the potentially disastrous effects of a poorly designed system. According to Canada Plan Service (M-6701), a good heating system is hence essential to the greenhouse operation. Although solar energy represents a significant factor in greenhouse heating, supplemental systems are a necessity for year round production. Greenhouses are essentially all about heat. While in the summer a well-placed greenhouse will gain most of its warmth directly from the sun, in the winter artificial ways of heating the greenhouse – and insulating it from cold prevailing winds – are very necessary. A precise estimation of greenhouse heating inputs and costs is necessary for optimization of the heating equipment and strategy (Baille et al., 2006).

The heat loss through a greenhouse cover material is particularly measured by the overall heat transfer coefficient (U_{cs}-value). The lower the U_{cs}-value, the better the insulation provided by the material (Basak et al., 2015). The U_{cs}-value depends on the cladding material, the sealing of the greenhouse structure, the heating system, the irrigation system, the wind speed, the cloudiness and the rainfall. The U_{cs}-value consists of two parts; the heat transfer coefficient for heat loss by heat transmission through the cladding material U and the heat transfer coefficient for heat loss by air exchange through air leakage U_l (Tantau, 2013; von Zabeltitz, 2011). This is simply expressed as:

$$U_{cs} = U + U_l \qquad\qquad\qquad (2.1)$$

where,

U_{cs} : overall heat transfer coefficient (U_{cs}-value)   [W m^{-2} K^{-1}]

U : heat transfer coefficient for heat loss through the material   [W m^{-2} K^{-1}]

U_l : heat transfer coefficient for heat loss through air leakage   [W m^{-2} K^{-1}]

The value U_l is about 10 % to 30 % of the U_{cs}-value (von Zabeltitz, 2011). The tightness of the greenhouse has a significant influence on the heat loss. The main influencing factors on the U_{cs}-value are the heating system and the cladding material of the greenhouse, including thermal screens for energy-saving (von Zabeltitz, 2011) and the thickness of the construction plus the material.

2.4 Modelling of Thermal Radiation Exchange

2.4.1 Downwelling longwave radiation

Downwelling longwave radiation LWR_d is the thermal radiation emitted by the atmosphere downward to the ground surface. An accurate prediction of this radiation from the sky is needed for many fields in agriculture, ranging from calculation of building energy requirements to estimation of climate change. Unlike shortwave radiation, difficulties and costs associated with longwave radiation measurements have been a major challenge. There is also a void of measurable atmospheric parameters which longwave radiation is dependent upon, such as cloudiness (Marty and Philipona, 2000). More recent studies have focused on quantifying the LWR_d under all-sky (clear and overcast) conditions. A summary of the selected studies on LWR_d in the recent past is presented in Table 2.2.

Table 2.2. Selected studies on downwelling longwave radiation and related parameters.

No.	Area of application	Cloudiness	View factor	Reference
1	Air-ice-ocean interactions	All-sky	-	Guest, 1998
2	Radiation scheme	All-sky	-	Sridhar and Elliott, 2002
3	Lowlands and mountains	All-sky	-	Iziomon et al., 2003
4	Land surfaces - parameters	All-sky	-	Choi et al., 2008
5	Satellite-based radiances	Clear-sky	✓	Tang and Li, 2008
6	Accuracy of algorithms	All-sky	-	Flerchinger et al., 2009
7	Glacier environment	All-sky	-	Sedlar and Hock, 2009
8	Model performance	Clear-sky	-	Dos Santos et al., 2011
9	Model uncertainties	All-sky	-	Gubler et al., 2012
10	Tropical forest	All-sky	-	Marthews et al., 2012
11	Flux monitoring sites	All-sky	-	Choi, 2013
12	Snow surface and trees	Clear-sky	✓	Howard and Stull, 2013

The downwelling longwave radiation flux (irradiance) emitted by the atmosphere and incident onto a horizontal surface can be routinely measured by pyrgeometers. These instruments are widely used in meteorological and climate research. In the past, a number of methods have been developed for estimating LWR_d when measurements of this variable are not available. In all cases, the starting point is that the atmosphere can be considered as a grey body, so LWR_d is determined by the effective atmospheric emissivity and the effective temperature of the overlying atmosphere (Viúdez-Mora, 2011).

Prediction of thermal radiation from the sky is a critical task necessary for many application fields, such as weather predictions, building energy requirements and global climate change (Choi, 2013; Kimball et al., 1982). The sky thermal irradiance reaching the ground surface per unit area is given by (Duffie and Beckman, 1991):

$$Q_{sky} = \varepsilon_{sky} \cdot \sigma \cdot T_{sky}^4 \tag{2.2}$$

where,

$\quad\quad Q_{sky}$: sky thermal irradiance $\quad\quad\quad\quad\quad$ [W m^{-2}]

$\quad\quad \varepsilon_{sky}$: sky emissivity $\quad\quad\quad\quad\quad\quad\quad\quad$ [-]

σ : Stefan-Boltzmann constant = $5.67 \cdot 10^{-8}$ [W m^{-2} K^{-4}]

T_{sky} : sky temperature   [K]

The sky emissivity ε_{sky} can be approximated as a function of the dew point temperature θ_{dp} as (Chen et al., 1995; Kimball et al., 1982):

$$\varepsilon_{sky} = \begin{pmatrix} 0.736 + x_1 \cdot \theta_{dp} \, ; \\ 0.741 + x_2 \cdot \theta_{dp} \, ; \\ 0.732 + x_3 \cdot \theta_{dp} \end{pmatrix} \qquad (2.3)$$

$$\theta_{dp} = \theta_o - \left(\frac{y_0 - RH}{z_0} \right) \qquad (2.4)$$

where,

ε_{sky} : sky emissivity   [-]

θ_{dp} : dew point temperature   [°C]

x_1 : coefficient = 0.0058 (Chen et al., 1995)   [°C^{-1}]

x_2 : coefficient = 0.0062 (Chen et al., 1995)   [°C^{-1}]

x_3 : coefficient = 0.0063 (Chen et al., 1995)   [°C^{-1}]

θ_o : outside air temperature   [°C]

y_0 : coefficient = 100 (Kimball et al., 1982)   [%]

z_0 : coefficient = 5 (Kimball et al., 1982)   [% °C^{-1}]

RH : relative humidity   [%]

Although it is slightly dependent on the water vapour, the usual value of ε_{sky} is about 0.74 (Romila, 2012).

The sky temperature T_{sky} is an important parameter for the simulation models in building studies (Adelard et al., 1998). The equivalent T_{sky} has been estimated differently by various researchers. Some of the common equations for computing the T_{sky} are given in Table 2.3.

Table 2.3. Equations for the computation of the sky temperature.

Author	Equation	No.
Tantau (1975)	$T_{sky} = T_a \cdot \left(x_{b,1} + x_{b,2} \cdot 10^{x_p \cdot P_d} \right)^{\frac{1}{4}}$	(2.5)
Von Elsner (1982)	$T_{sky} = \left(y_{c,1} \cdot \theta_o + x_{a,1} + C \cdot (x_{a,2} + y_{c,2} \cdot \theta_o) \right) + c_k$	(2.6)
Nijskens et al. (1984)	$T_{sky} = x_{c,1} \cdot T_a^{1.5}$	(2.7)
Berdahl and Martin (1984)	$T_{sky} = T_a \cdot \left(x_{b,3} + x_{c,2} \cdot T_d + x_{c,3} \cdot T_d^2 + x_{b,4} \cdot \cos(x_{d,1} \cdot \upsilon) \right)^{\frac{1}{4}}$	(2.8)

where,

T_{sky}	: sky temperature	[K]
T_a	: absolute air temperature	[K]
$x_{b,1}$	: coefficient = 0.82 (Tantau, 1975)	[K^4]
$x_{b,2}$	: coefficient = -0.25 (Tantau, 1975)	[K^4]
x_p	: coefficient = -0.095 (Tantau, 1975)	[hPa^{-1}]
P_d	: partial water vapour pressure	[hPa]
θ_o	: outside air temperature	[°C]
C	: cloudiness factor	[-]
$y_{c,1}$	: coefficient = 1.2 (von Elsner, 1982)	[-]
$y_{c,2}$	: coefficient = -0.26 (von Elsner, 1982)	[-]
$x_{a,1}$	: coefficient = -21.4 (von Elsner, 1982)	[°C]
$x_{a,2}$	: coefficient = 20.6 (von Elsner, 1982)	[°C]
c_k	: coefficient = 273.15 (Celsius to Kelvin)	[K]
$x_{c,1}$	: coefficient = 0.0552 (Nijskens et al., 1984)	[K$^{-0.5}$]
$x_{b,3}$	: coefficient = 0.711 (Berdahl and Martin, 1984)	[K^4]
$x_{c,2}$	: coefficient = $5.6 \cdot 10^{-3}$ (Berdahl and Martin, 1984)	[K^3]
$x_{c,3}$	: coefficient = $7.3 \cdot 10^{-5}$ (Berdahl and Martin, 1984)	[K^2]
$x_{b,4}$	: coefficient = 0.013 (Berdahl and Martin, 1984)	[K^4]
$x_{d,1}$	: coefficient = 15 (Berdahl and Martin, 1984)	[° h^{-1}]
T_d	: dew point temperature	[K]
υ	: hour from midnight	[h]

In recent decades, successful techniques have been developed to estimate the downwelling longwave radiation LWR_d based on the near-surface humidity and air temperature (Cheng and Nnadi, 2014; Sridhar and Elliot, 2002). According to Rizou and Nnadi (2007), either air temperature or humidity parameters can capture all LWR_d over a wide range of climatic conditions. This is because of the compensating effects of temperature and water vapour. In this regard, the equation for clear-sky LWR_d can be expressed as (Jacobs et al., 2004; Iziomon et al., 2003):

$$LWR_d = \varepsilon_{cs} \cdot \sigma \cdot T_a^4 \qquad\qquad (2.9)$$

where,

        LWR_d : downwelling longwave radiation   [W m^{-2}]

        ε_{cs} : clear-sky atmospheric emissivity   [-]

        σ : Stefan-Boltzmann constant = $5.67 \cdot 10^{-8}$ [W m^{-2} K^{-4}]

        T_a : absolute air temperature   [K]

Under all-sky conditions (clear-sky and overcast), an effective atmospheric emissivity ε_a is very useful in the calculation of LWR_d. Due to the presence of clouds, the clear-sky LWR_d formulation requires appropriate modification (Jacobs et al., 2004; Iziomon et al., 2003). Thus, the all-sky LWR_d can be expressed as (Choi et al., 2008; Dos Santos et al., 2011):

$$LWR_d = \varepsilon_a \cdot \sigma \cdot T_a^4 \qquad\qquad (2.10)$$

where,

        LWR_d : downwelling longwave radiation   [W m^{-2}]

        ε_a : effective atmospheric emissivity   [-]

        σ : Stefan-Boltzmann constant = $5.67 \cdot 10^{-8}$ [W m^{-2} K^{-4}]

        T_a : absolute air temperature   [K]

Various parameterizations to estimate the ε_a are found in the literature for different climatic conditions (Flerchinger et al., 2009). Other than the outside air temperature θ_o, the parameterizations require the vapor pressure e_a to be known (Kimball et al., 1982). The value of e_a can be computed as (Dingman, 2009):

$$e_a = y_{p,1} \cdot \exp\left(\frac{y_{c,3} \cdot \theta_o}{\theta_o + x_{a,3}}\right) \cdot \frac{RH}{y_0} \qquad\qquad (2.11)$$

where,

e_a : water vapour pressure of air   [Pa]

θ_o : outside air temperature   [°C]

RH : relative humidity   [%]

$y_{p,1}$: coefficient = 610.8 (Dingman, 2009)   [Pa]

$y_{c,3}$: coefficient = 17.27 (Dingman, 2009)   [-]

$x_{a,3}$: coefficient = 237.3 (Dingman, 2009)   [°C]

y_0 : coefficient = 100 (Kimball et al., 1982)   [%]

2.4.2 Upwelling longwave radiation

The radiation from the surface to the sky accounts for radiation exchange with the sky at a sky temperature T_{sky} rather than an ambient temperature T_a. The sky can be considered as a blackbody at some equivalent T_{sky} to account for the facts that the atmosphere is not at a uniform temperature and that the atmosphere radiates only in a certain wavelength band (Taha, 2003; Duffie and Beckman, 1991). Generally, the upwelling longwave radiation LWR_u can be computed once the surface temperature T_s and emissivity ε_s are known. Some LWR_u studies selected from the literature are given in Table 2.4.

Table 2.4. Recent studies by different researchers on the upwelling longwave radiation.

No.	Area of application	Cloudiness	Temperature	Reference
1	Pine forest	All-sky	✓	Kessler and Jaeger, 2003
2	Plant ecophysiology	-	✓	Jones et al., 2003
3	Greenhouse surfaces	-	✓	Taha, 2003
4	Wetland evapotranspiration	All-sky	✓	Jacobs et al., 2004
5	Satellite-derived data	Clear-sky	✓	Wang et al., 2009
6	Surface radiation budget	Clear-sky	✓	Wu et al., 2012

All bodies emit radiation as a function of their temperature with both the energy emitted and its wavelength distribution changing with temperature according to the Stefan-Boltzmann law and the Planck distribution function, respectively. The exterior surface exchanges longwave radiation with other elements such as sky, ground and other surfaces

like other buildings, shading devices as well as more distant objects like mountain slopes (Fig. 2.1). Vegetation cover also affects the influence of other surfaces (Evins et al., 2014).
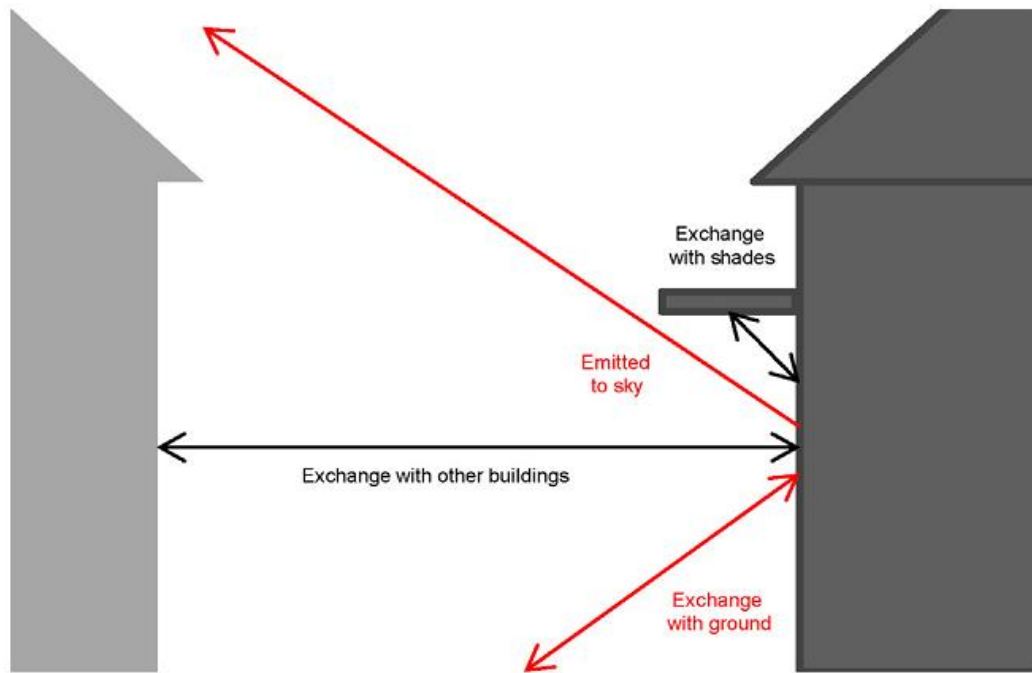
Fig. 2.1. Longwave radiation exchange processes at an exterior building surface
(Source: Evins et al., 2014).

The total energy emitted by a surface is a function of its temperature according to the Stefan-Boltzman law (Jones et al., 2003). The longwave radiation heat flux emitted by the exterior cover surface can be performed with the relation (Jones et al., 2003):

$$LWR_u = \varepsilon_s \cdot \sigma \cdot T_s^4 \tag{2.12}$$

where,

LWR_u : upwelling longwave radiation   [W m^{-2}]

ε_s : surface emissivity   [-]

σ : Stefan-Boltzmann constant = $5.67 \cdot 10^{-8}$ [W m^{-2} K^{-4}]

T_s : cover surface temperature   [K]

The view factor gives the fraction of the view from a base surface obstructed by a given other surface (Evins et al., 2014). It can be calculated numerically or analytically (Howell, 1982). A horizontal surface can see the whole sky, hence it radiates to the whole sky and its view factor with respect to the sky F_{sky} is 1. For a non-horizontal surface (e.g. roof and wall), the view factor has to be used since this is less than one. A vertical surface (tilt angle

from the vertical plane Φ = 0°) will only see half of the sky. The radiation that leaves the inclined surface is either incident on the ground or it goes to the sky and according to Arora (2010), the following relation applies.

$$F_{gnd} + F_{sky} = 1 \tag{2.13}$$

where,

F_{gnd} : view factor to the ground   [-]

F_{sky} : view factor to the sky   [-]

2.4.3 Solar radiation

Solar radiation is the primary energy source of the earth-atmosphere system, which derives the formation and evolution of weather and climate processes (Bi et al., 2013; Yang et al., 2010). It is of economic importance to renewable energy alternative. The solar radiation reaching the earth's surface depends on the climatic condition of the specific site location, and this is essential for accurate prediction and design of a solar energy system (Burari and Sambo, 2001). In the recent past, solar irradiances on both horizontal and inclined surfaces have been taken into consideration (Table 2.5).

Table 2.5. Selected researches on solar radiation incident on various surfaces.

No.	Area of application	Cloudiness	Inclination	Reference
1	Radiation transmittance	All-sky	✓	Pollet et al., 2002
2	Pine forest	All-sky	-	Kessler and Jaeger, 2003
3	Evapotranspiration	All-sky	-	Jacobs et al., 2004
4	Correlation models	All-sky	-	Jacovides et al., 2006
5	Models - tilted surfaces	All-sky	✓	Evseev and Kudish, 2009
6	Surfaces: horizontal, tilted	-	✓	El-Sebaii et al., 2010
7	Inclined surfaces	-	✓	Ibrahim et al., 2011
8	Solar collector and factors	-	✓	Abdullah and Ali, 2012
9	Model uncertainties	All-sky	-	Gubler et al., 2012
10	Semi-arid climate	Clear-sky	-	Bi et al., 2013
11	Complex topography	All-sky	✓	Formetta et al., 2013

According to Garg and Prakash (2000) and Al-Ajlan et al. (2003), the solar radiation incident on external greenhouse surfaces can be broken down into three main components (Fig. 2.2):

   a) direct (beam) radiation emanating from the region of the sky near to the sun's disc

   b) diffuse radiation from the sky vault

   c) radiation scattered or reflected by the ground
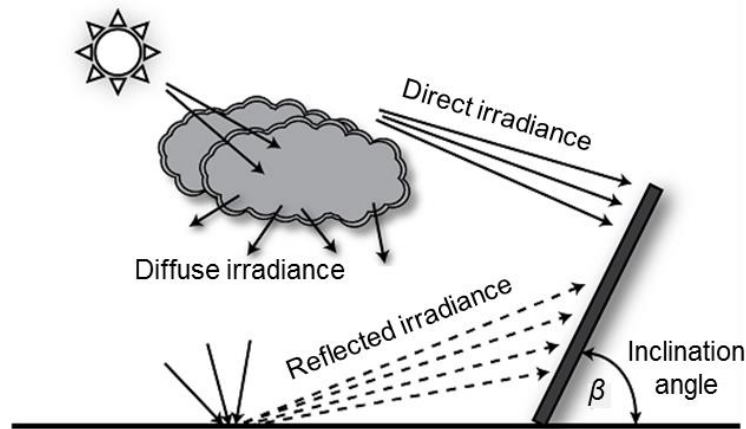
Fig. 2.2. Solar irradiance components (Source: modified after Gulin et al., 2013).

The solar radiation reaching the earth's surface is expressed in terms of the solar constant, I_{sc}. It is defined as the total radiation energy received from the sun per unit area in a unit time on the earth's surface perpendicular to the sun's rays at a mean distance of the earth from the sun ($1.496 \cdot 10^8$ km). The I_{sc} is valued at 1367 W m^{-2} (Sukhatme, 2003; Iqbal, 1983) and this is accepted by many standard organizations including the American Society for Standards and Measurement (ASTM). Although the National Oceanographic and Atmospheric Administration (NOAA) uses a value of 1376 W m^{-2}, the fluctuations are normally small (Howell et al., 2011). Due to the elliptical orbiting of the earth around the sun, the distance between the earth and the sun fluctuates annually and this makes the amount of energy received on the earth's surface fluctuate in a manner given by (Duffie and Beckman, 1991):

$$I_n = I_{sc} \cdot \left(1 + y_{c,4} \cdot \cos \left(\frac{x_{r,1} \cdot n_d}{x_{n,1}} \right) \right) \qquad (2.14)$$

where,

   I_n : extraterrestrial radiation on a plane normal to the radiation   [W m^{-2}]

   I_{sc} : solar constant = 1367 (Sukhatme, 2003; Iqbal, 1983)   [W m^{-2}]

$y_{c,4}$: coefficient = 0.033 (Duffie and Beckman, 1991)   [-]

$x_{r,1}$: coefficient = 360 (Duffie and Beckman, 1991)   [°]

$x_{n,1}$: coefficient = 365 (days in a year) (Duffie and Beckman, 1991) [day]

n_d : day of the year   [day]

The value of n_d ranges from 1 (on 1st January) to 365 or 366 (on 31st December).

Hourly global radiation on horizontal surfaces are available for many stations, but relatively few stations measure the hourly diffuse radiation (Abdullah and Ali, 2012; Ibrahim et al., 2011; El-Sebaii et al., 2010; Wong and Chow, 2001). The hourly extraterrestrial solar radiation on a horizontal surface $I_{e,h}$ for a period defined by hour angles ω_1 and ω_2 (where ω_2 is larger than ω_1) can be calculated using the following equation (El-Sebaii et al., 2010; Duffie and Beckman, 1991):

$$I_{e,h} = \frac{12 \cdot I_n}{y_{c,5}} \cdot \left(\frac{y_{c,5} \cdot (\omega_2 - \omega_1)}{x_{r,2}} \cdot \sin\varphi \cdot \sin\delta + \cos\delta \cdot \cos\varphi \cdot (\sin\omega_2 - \sin\omega_1) \right) (2.15)$$

where,

$I_{e,h}$: extraterrestrial radiation on a horizontal surface   [W m^{-2}]

I_n : extraterrestrial radiation on a plane normal to the radiation [W m^{-2}]

$y_{c,5}$: coefficient = π = 3.142 (Duffie and Beckman, 1991)   [-]

$x_{r,2}$: coefficient = 180 (Duffie and Beckman, 1991)   [°]

φ : latitude   [°]

δ : angle of declination   [°]

ω_1 : hour angle at time 1   [°]

ω_2 : hour angle at time 2   [°]

The angle of declination δ can be evaluated from the following expression (Sukhatme, 2003; Ezekoye and Enebe, 2006):

$$\delta = x_{r,3} \cdot \sin\left(x_{r,1} \cdot \left(\frac{x_{n,2} + n_d}{x_{n,1}} \right) \right) \qquad (2.16)$$

where,

δ : angle of declination   [°]

$x_{r,3}$: coefficient = 23.45 (earth's tilt) (Sukhatme, 2003)   [°]

$x_{r,1}$: coefficient = 360 (Sukhatme, 2003)   [°]

$x_{n,2}$: coefficient = 284 (Sukhatme, 2003)   [day]

$x_{n,1}$: coefficient = 365 (days in a year) (Sukhatme, 2003)   [day]

n_d : day of the year   [day]

The hour angle ω is computed as a function of the hour of the day in 24 hour time H_t as (Abdullah and Ali, 2012; Sukhatme, 2003):

$$\omega = \frac{H_t - x_{t,1}}{x_{t,2}} \cdot x_{r,1}$$
(2.17)

where,

ω : hour angle   [°]

H_t : hour time   [h]

$x_{t,1}$: coefficient = 12 (Abdullah and Ali, 2012)   [h]

$x_{t,2}$: coefficient = 24 (Abdullah and Ali, 2012)   [h]

$x_{r,1}$: coefficient = 360 (Sukhatme, 2003)   [°]

This means that the hour angle has a negative value before local solar noon, a positive value after local solar noon and is zero at local solar time (Abdullah and Ali, 2012). According to Honsberg and Bowden (2012), the local solar time (LST) can be found by using two corrections to adjust the local time (LT).

$$LST = LT + \frac{TC}{x_{t,3}}$$
(2.18)

where,

LST : local solar time   [h]

LT   : local time   [h]

TC   : time correction factor   [min]

$x_{t,3}$: coefficient = 60 (Honsberg and Bowden, 2012)   [min h^{-1}]

The time correction factor (TC) accounts for the variation of the LST within a given time zone due to the longitude variations within the time zone (Duffie and Beckman, 1991; Goswami et al., 2000; Honsberg and Bowden, 2012) and also incorporates the equation of time (EoT).

$$TC = (x_{d,2})^{-1} \cdot (L_{st} - L_{loc}) + EoT \qquad\qquad (2.19)$$

where,

      TC : time correction factor   [min]

      $x_{d,2}$: coefficient = 4 (Goswami et al., 2000)   [° min^{-1}]

      L_{st} : standard meridian for local time zone   [°]

      L_{loc} : longitude of the location   [°]

      EoT : equation of time   [min]

The *EoT* is calculated from the following expression (Honsberg and Bowden, 2012):

$$EoT = x_{m,1} \cdot \sin(2 \cdot B) - x_{m,2} \cdot \cos(B) - x_{m,3} \cdot \sin(B) \qquad\qquad (2.20)$$

The coefficient *B* is given by (Honsberg and Bowden, 2012):

$$B = \frac{x_{r,1}}{x_{n,1}} \cdot (n_d - x_{n,3}) \qquad\qquad (2.21)$$

where,

      EoT : equation of time   [min]

      B : coefficient (Honsberg and Bowden, 2012)   [°]

      $x_{m,1}$: coefficient = 9.87 (Honsberg and Bowden, 2012)   [min]

      $x_{m,2}$: coefficient = 7.53 (Honsberg and Bowden, 2012)   [min]

      $x_{m,3}$: coefficient = 1.5 (Honsberg and Bowden, 2012)   [min]

      $x_{r,1}$: coefficient = 360 (Honsberg and Bowden, 2012)   [°]

      $x_{n,1}$: coefficient = 365 (days in a year) (Sukhatme, 2003) [day]

      n_d : day of the year   [day]

      $x_{n,3}$: coefficient = 81 (Honsberg and Bowden, 2012)   [day]

An overview of the solar angles involved in calculating the amount of solar irradiance on tilted surfaces is shown in Fig. 2.3. The angle of incidence θ for a surface inclined to the south towards the equator (northern hemisphere) is dependent on the inclination angle (Twidell and Weir, 2005). The zenith angle θ_z is the angle between the line that points to the sun and the vertical. At solar noon θ_z is zero, while in the sunrise and sunset this angle is 90°. The solar azimuth angle γ is the deviation of the projection on a horizontal plane of the normal to the surface from the local meridian, with zero due south, east negative and

west positive (Sahin and Sen, 2008). This angle is only measured in the horizontal plane and thus neglects the height of the sun. The solar altitude α (also known as solar elevation angle) is the angle between the horizon and the centre of the sun's disc.
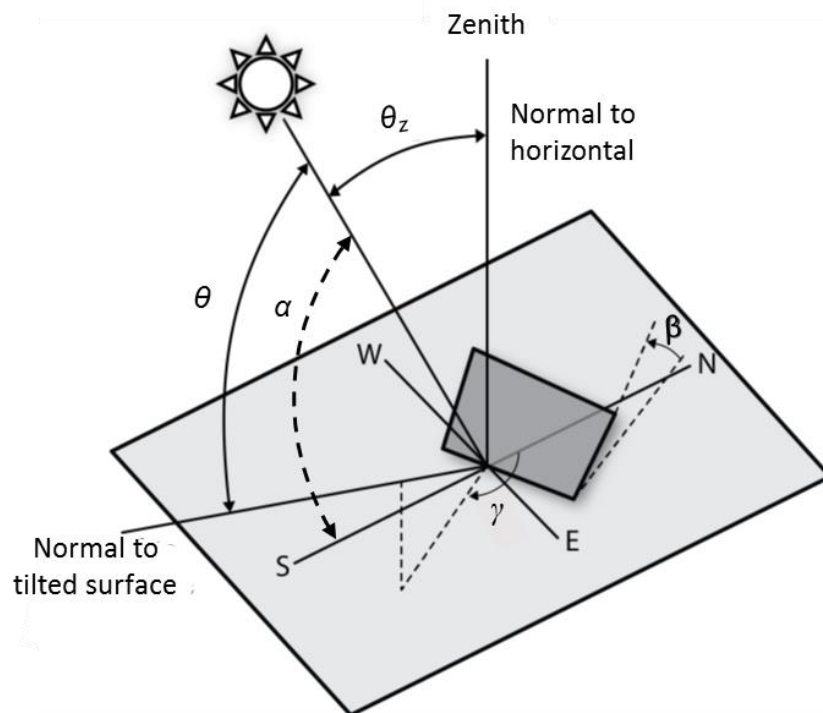
Fig. 2.3. Detailed description of solar angles for a tilted surface (Source: modified after Twidell and Weir, 2005).

The angle of incidence, the solar altitude, the zenith angle and the solar azimuth angle are generally expressed as (Yang et al., 2012; Shamim et al., 2015; Twidell and Weir, 2005; Bolsenga, 1979):

$$\theta = \arccos\left(\cos\delta \cdot \cos\left(\varphi - \beta\right) \cdot \cos\omega + \sin\delta \cdot \sin\left(\varphi - \beta\right)\right) \qquad (2.22)$$

$$\theta_z = \arccos\left(\cos\delta \cdot \cos\varphi \cdot \cos\omega + \sin\delta \cdot \sin\varphi\right) \qquad (2.23)$$

$$\alpha = \arcsin\left(\cos\delta \cdot \cos\varphi \cdot \cos\omega + \sin\delta \cdot \sin\varphi\right) \qquad (2.24)$$

$$\gamma = \arccos\left(\frac{\sin\delta \cdot \cos\varphi - \cos\delta \cdot \sin\varphi \cdot \cos\omega}{\cos\alpha}\right) \qquad (2.25)$$

where,

θ	: angle of incidence	[°]
θ_z	: zenith angle	[°]
α	: solar altitude	[°]

γ : solar azimuth angle   [°]

δ : angle of declination   [°]

φ : latitude   [°]

β : inclination angle   [°]

ω : hour angle   [°]

This implies, therefore, that the zenith angle θ_z and the solar altitude α are related as:

$$\alpha = x_{r,4} - \theta_z \tag{2.26}$$

where,

α : solar altitude   [°]

$x_{r,4}$: coefficient = 90° (vertical plane)   [°]

θ_z : zenith angle   [°]

If latitude and declination are known, the day length can be calculated as (FAO, 1998):

$$L_d = \frac{x_{t,2}}{x_{r,2}} \cdot \omega_s \tag{2.27}$$

where,

L_d : day length   [h]

$x_{t,2}$: coefficient = 24 (FAO, 1998)   [h]

$x_{r,2}$: coefficient = π rad = 180° (FAO, 1998)   [°]

ω_s : sunset hour angle   [°]

The hourly clearness index I_c is another critical parameter and can be estimated as the ratio of global radiation on the horizontal surface $I_{g,h}$ to the extraterrestrial radiation on the horizontal surface I_o (El-Sebaii et al., 2010; Abdullah and Ali, 2012):

$$I_c = \frac{I_{g,h}}{I_{e,h}} \tag{2.28}$$

where,

I_c : clearness index   [-]

$I_{g,h}$: global solar radiation on a horizontal surface   [W m^{-2}]

$I_{e,h}$: extraterrestrial radiation on a horizontal surface   [W m^{-2}]

The diffuse radiation $I_{d,h}$ is that portion of solar radiation that is scattered downwards by the molecules in the atmosphere. The hourly values of $I_{d,h}$ can be calculated as (Miguel et al., 2001):

$$\frac{I_{d,h}}{I_{g,h}} = \begin{pmatrix} 0.995 - 0.081 \cdot I_c & ; & \text{if } I_c < 0.21 \\ 0.724 + 2.738 \cdot I_c - 8.32 \cdot I_c^2 + 4.967 \cdot I_c^3 & ; & \text{if } 0.21 \le I_c \le 0.76 \\ 0.18 & ; & \text{if } I_c > 0.76 \end{pmatrix} \quad (2.29)$$

where,

$I_{d,h}$: diffuse radiation on a horizontal surface $\quad$ [W m^{-2}]

$I_{g,h}$: global solar radiation on a horizontal surface $\quad$ [W m^{-2}]

I_c $\quad$: clearness index $\quad\quad\quad\quad\quad\quad\quad\quad\quad\quad$ [-]

The beam radiation $I_{b,h}$ reaching a unit area of a horizontal surface on the earth in the absence of the atmosphere can be expressed by (Ibrahim et al., 2011):

$$I_{b,h} = I_{g,h} - I_{d,h} \quad\quad\quad\quad\quad\quad\quad\quad\quad (2.30)$$

where,

$I_{b,h}$: beam radiation on a horizontal surface $\quad$ [W m^{-2}]

$I_{g,h}$: global solar radiation on a horizontal surface $\quad$ [W m^{-2}]

$I_{d,h}$: diffuse radiation on a horizontal surface $\quad$ [W m^{-2}]

2.4.4 Net Radiation

Net radiation is the difference between the energy received and the energy lost by radiation (Hanan, 1997). It is a critical component of the surface energy budget and is an essential variable for understanding the interaction between surfaces and the atmosphere (Choi, 2013; Brutsaert, 1975; Sugita and Brutsaert, 1993; Crawford and Duchon, 1999; Offerle et al., 2003). During the day, the sun which generally provides a large amount of radiation assures a net gain of energy, because the losses are much smaller. This net gain of energy causes a subsequent greenhouse air temperature rise. However, at night, the warm masses within the greenhouse (earthen floor, concrete paths, metal benches, plants, etc) produce significant radiation losses to the colder outdoor environment. The net energy loss is caused by transmission of infrared and thermal radiation through the cover, as well as emission of radiation from the cover to the cold

sky. The amount of this radiation energy loss depends, not only on the properties of the cover, but also on the temperature of the cover, and the atmospheric conditions (Hanan, 1997; Giacomelli and Roberts, 1998).

Under daytime and nighttime situations, the net radiation of the greenhouse is important for evaluation of the greenhouse energy situation (Hanan, 1997). A combination of night sky conditions (e.g. cloudiness, atmospheric emissivity, relative humidity) and the location of adjacent surfaces (such as other greenhouses or buildings) can directly affect the net radiation losses. For a dry greenhouse system (with no plants), energy balance requires knowledge of air exchange rate. The determination of the air exchange rate due to leaks in a greenhouse is possible with a tracer gas (Tantau, 2013). The overall heat transfer coefficient (U_{cs}-value) is of greater importance in the assessment of energy balance at the greenhouse surfaces. Past research has focused on the net radiative flux over many surfaces including greenhouses. Some of the selected studies are summarized in Table 2.6. However, a few of these studies have taken into account the U_{cs}-value of the system.

Table 2.6. Some past researches on surface net radiation and energy balance.

No.	Area of application	Orientation/ Inclination	U_{cs}-value effect	Reference
1	Snow surface	-	-	Ambach, 1974
2	Energy consumption	✓	✓	Jolliet et al., 1991
3	Topographic effects	✓	-	Nie et al., 1992
4	Greenhouse design	✓	-	Gupta and Chandra, 2002
5	Pine forest	-	-	Kessler and Jaeger, 2003
6	Cooled greenhouse	✓	✓	Abdel-Ghany and Kozai, 2006
7	Unheated greenhouse	✓	-	Mesmoudi et al., 2010
8	Thermal performance	✓	-	Berroug et al., 2011
9	Radiation balance	-	-	Ferreira et al., 2012
10	Thermography	✓	✓	Lehmann et al., 2013
11	Building surfaces	✓	-	Evins et al., 2014

2.5 Modelling of Convective Heat Exchange at Greenhouse Surfaces

Convection refers to the heat transfer process between the surface and the surrounding air (Mammeri et al., 2015). The convective heat transfer occurs in two ways: the natural convection caused by the temperature gradient between the exterior surface and the outdoor air, and the forced convection caused by the pressure gradient due to the prevailing outside wind (Liu and Harris, 2013). The convective heat transfer coefficient U_{cv} for a greenhouse covering is the heat flux density of the covering to its surroundings induced by a unit temperature difference between the covering and the air remote from the covering (Papadakis et al. 2000). Heat transfer by convection includes not only the movement of air but also the movement of water vapor (Worley, 2014).

According to Mesmoudi et al. (2010), a more accurate determination of the convective heat transfer coefficient U_{cv} at the outside cover of the greenhouse would require an expression which takes into account not only the effect of the wind but also the flow regime and the effect of the temperature difference when the wind speed is low. In this prospect, the following expression seems more adapted (Mesmoudi et al., 2012):

$$U_{cv} = b_0 + b_1 \cdot v^c \tag{2.31}$$

where:

    U_{cv} : convective heat transfer coefficient   [W m^{-2} K^{-1}]

    b_0, b_1 : coefficients determined experimentally   [-]

    c : coefficient determined experimentally   [-]

    v : wind speed   [m s^{-1}]

The parameter U_{cv} depends on convection modes and flow types (laminar or turbulent) and is deduced from the appropriate Nusselt number (Nu) according to the laminar boundary layer theory (Holman, 1986) and this is expressed as:

$$h_{cv} = \frac{k_a \cdot \mathrm{Nu}}{L} \tag{2.32}$$

where:

    k_a : thermal conductivity of air   [W m^{-1} K^{-1}]

    L : characteristic length of the solid surface   [m]

    Nu   : Nusselt number   [-]

The characteristic length is related to the shape of the object and measures the length of the surface covered by the laminar flow. For the greenhouse cover, the roof slope length (length of glass panes or any other cover material) is generally used (Roy et al., 2002). The greenhouse cover exchanges energy at the inner surface to the greenhouse air and to outside air at the outer surface. The ratio between Gr (Grashof) and Re (Reynolds) numbers indicates whether the exchange is due to natural or forced convection. Local air velocities inside the greenhouse are in the order of 0.1 m s^{-1} (Re $\approx$ 10^4) and the temperature differences of about 10 K (Gr $\approx$ 10^{10}) and therefore natural convection is the prevailing form of heat transfer (Bot and van de Braak, 1995). Under natural (free) convection mode, heat transfer takes place through the fluid motion induced by temperature gradients (Roy et al., 2002). A few of the existing U_{cv} models are presented in Table 2.7.

Table 2.7. List of empirical formulae for convective heat transfer coefficients between the exterior cover surface and the air according to different authors.

Surface conditions	Source	Equation	No.
Greenhouse surface	Kanthak (1970)	$U_{cv} = y_{u,1} \cdot v^{0.72}$	(2.33)
Tunnel-type greenhouse (PE – polyethylene film)	Garzoli and Blackwell (1981)	$U_{cv} = x_{w,1} \cdot v + x_{u,1}$	(2.34)
Venlo-type greenhouse	Bot (1983)	$U_{cv} = x_{w,2} \cdot v + x_{u,2}$	(2.35)
Building surfaces	Sharples (1984)	$U_{cv} = x_{w,3} \cdot v + x_{u,3}$	(2.36)
Tunnel-type greenhouse (PE cover film)	Kittas (1986)	$U_{cv} = y_{u,2} \cdot (\Delta T_{s-a})^{\frac{1}{4}} + y_{u,3} \cdot v^{0.8}$	(2.37)
Twin-span greenhouse (PE cover film; $v \leq 6.3$ m s^{-1})	Papadakis et al. (1992)	$U_{cv} = y_{u,4} \cdot v^{0.49} + x_{u,4}$	(2.38)
Walls of low-rise buildings	Emmel et al. (2007)	$U_{cv} = y_{u,5} \cdot v_{10}^{0.71}$	(2.39)
Greenhouses in humid regions	Suhardiyanto and Romdhonah (2008)	$U_{cv} = y_{u,6} \cdot v^{0.33} + x_{u,5}$	(2.40)
Roof wind speed	Liu and Harris (2013)	$U_{cv} = x_{w,4} \cdot v + x_{u,6}$	(2.41)
Wall wind speed	Liu and Harris (2013)	$U_{cv} = x_{w,5} \cdot v_s + x_{u,7}$	(2.42)

where,

U_{cv} : convective heat transfer coefficient   [W m^{-2} K^{-1}]

v : local wind speed   [m s^{-1}]

v_{10} : wind speed at 10 m above the ground   [m s^{-1}]

v_s : wind speed close to the wall surface   [m s^{-1}]

ΔT_{s-a} : surface-to-air temperature difference   [K]

$y_{u,1}$: coefficient = 4.17 (Kanthak, 1970)   [W s$^{0.72}$ m$^{-2.72}$ K^{-1}]

$x_{w,1}$: coefficient = 3.8 (Garzoli and Blackwell, 1981)   [W s m^{-3} K^{-1}]

$x_{u,1}$: coefficient = 7.2 Garzoli and Blackwell (1981)   [W m^{-2} K^{-1}]

$x_{w,2}$: coefficient = 1.2 (Bot, 1983)   [W s m^{-3} K^{-1}]

$x_{u,2}$: coefficient = 2.8 (Bot, 1983)   [W m^{-2} K^{-1}]

$x_{w,3}$: coefficient = 1.7 (Sharples, 1984)   [W s m^{-3} K^{-1}]

$x_{u,3}$: coefficient = 5.1 (Sharples, 1984)   [W m^{-2} K^{-1}]

$y_{u,2}$: coefficient = 1.32 (Kittas, 1986)   [W m^{-2} K$^{-1.25}$]

$y_{u,3}$: coefficient = 3.12 (Kittas, 1986)   [W s$^{0.8}$ m$^{-2.8}$ K^{-1}]

$y_{u,4}$: coefficient = 6.76 (Papadakis et al., 1992)   [W s$^{0.49}$ m$^{-2.49}$ K^{-1}]

$x_{u,4}$: coefficient = 0.95 (Papadakis et al., 1992)   [W m^{-2} K^{-1}]

$y_{u,5}$: coefficient = 4.78 (Emmel et al., 2007)   [W s$^{0.71}$ m$^{-2.71}$ K^{-1}]

$y_{u,6}$: coefficient = 1.84 (Suhardiyanto and Romdhonah, 2008) [W s$^{0.33}$ m$^{-2.33}$ K^{-1}]

$x_{u,5}$: coefficient = 1.78 Suhardiyanto and Romdhonah (2008)   [W m^{-2} K^{-1}]

$x_{w,4}$: coefficient = 1.825 (Liu and Harris, 2013)   [W s m^{-3} K^{-1}]

$x_{u,6}$: coefficient = 2.815 (Liu and Harris, 2013)   [W m^{-2} K^{-1}]

$x_{w,5}$: coefficient = 5.67 (Liu and Harris, 2013)   [W s m^{-3} K^{-1}]

$x_{u,7}$: coefficient = 3.25 (Liu and Harris, 2013)   [W m^{-2} K^{-1}]

Generally, forced convection is expected at the outside due to air velocities generated by the wind field (van de Braak, 1995). According to previous studies, the variation in the convective heat transfer models depended on the greenhouse geometry (Suhardiyanto and Romdhonah, 2008).

3 RESEARCH OBJECTIVES

Accurate and detailed prediction of heat consumption of greenhouses is necessary in modern protected cultivation. For this purpose, an accurate and reliable greenhouse-sky heat transfer model is required. Most researches have not studied in detail the thermal radiation exchange under both day and night situations. None of these researches considered factors like the cover surface components (cover material and glazing bars), surface orientation, inclination angle and prevailing climatic factors (especially cloudiness and rain). Thus, the available models until now are not entirely useful in practical situations. The main objective of this study is therefore to model the thermal radiation exchange between the glass-covered greenhouse surfaces and the sky considering representative test conditions.

To achieve this goal, the specific objectives of this study are as follows:

a) To determine the influence of glass-covered greenhouse surface inclination and orientation on the exterior thermal radiation exchange.

b) To model the individual or combined effects of different climatic variables and design factors on the thermal radiation exchange.

c) To establish the significance of the thermal radiative heat transfer coefficient in the overall heat transfer coefficient (U_{cs}-value) model which is used today.

4 MATERIALS AND METHODS

4.1 General

4.1.1 Overview

A summarized representation of the parameters and factors considered in this study is presented in Fig. 4.1. It applies to the external greenhouse cover surface and its exchange of thermal radiation with the sky. Glass and steel glazing bars constituted the cover surface components of the developed big south-facing thermal box. With this information, the developed radiation models were tested and compared with the measurements from the experimental setup under both day and night situations. The nighttime measurements were utilized to understand the influence of the radiative heat transfer coefficient on the overall heat transfer coefficient (U_{cs}-value). The same cover design parameters were applied for the miniaturized thermal boxes (oriented to south, west, north and east) in determining the surface inclination and orientation effects on the radiation exchanges.

■ Material data
- Type (float glass)
- Nature of surface
- Other properties (emissivity, thermal conductivity, etc)

■ Climatic factors
- Air temperature
- Wind speed and direction
- Relative humidity
- Cloudiness
- Rain
- Radiation

Thermal radiation exchange

■ Design data
- Composition (glass and glazing bars)
- Orientation (east, west, north, south)
- Inclination angle
- Wall and roof type
- Surface area

■ Heat loss assessment
- Heat requirement or consumption
- U_{cs}-value

Fig. 4.1. Parameters and factors related to the thermal radiation exchange at greenhouse surfaces.

Heating of the big south-facing thermal box was necessary at night and the experiments were therefore done during winter periods (2013/2014 and 2014/2015). The developed system was placed outdoors at the Biosystems Engineering Section, Institute of Horticultural Production Systems, Leibniz Universität Hannover (52.39° N, 9.706° E and altitude 52.3 m above mean sea level (AMSL)). This measurement site is located in Lower Saxony, Germany. The city of Hannover lies in the north of Germany (Fig. 4.2). This helped in understanding the influence of atmospheric conditions such as air temperature, wind speed and direction, relative humidity, cloudiness and rain on the determined U_{cs}-value. During the spring period of 2014, the measurement data was used in validating the solar radiation models. Some of the parameters were also applied in checking the effects on the thermal radiation exchange brought about by the cover surface inclination and orientation. This required nighttime data from the four miniaturized thermal boxes during the months of October 2014 to March 2015.

Study site in Hannover, Germany
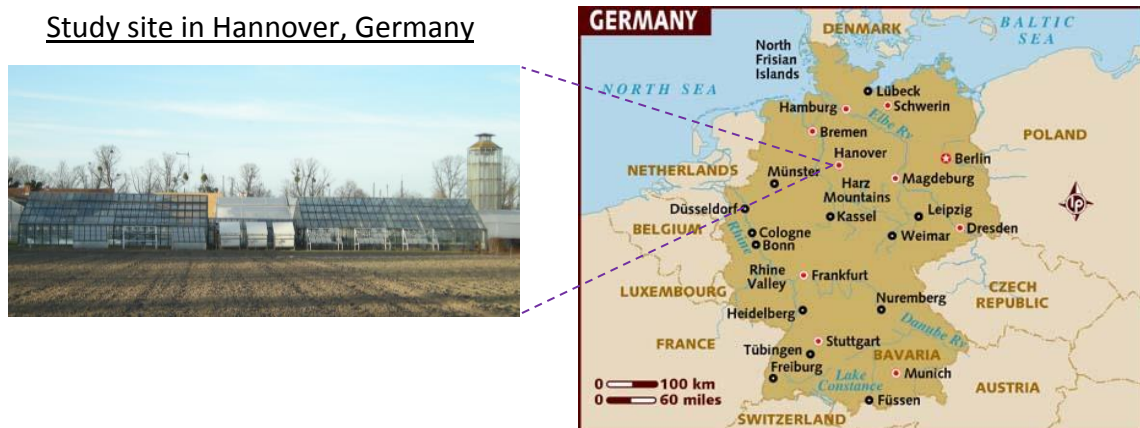
Fig. 4.2. Study location on the map of Germany (Source, right map: Lonely Planet, 2015).

The U_{cs}-value consists of the heat transfer coefficients due to transmission through the material U and that due to air leakages U_l. Through the schematic diagram (Fig. 4.3), the radiative heat transfer coefficient U_{lir} and the convective heat transfer coefficient U_{cv} can be associated to other parameters or effects. It is a representation of the heat transfers inside and outside a greenhouse. This scheme was necessary to identify the key parameters which influence the thermal radiation models and ultimately establish the interactions between the U_{lir} and the U_{cv}.
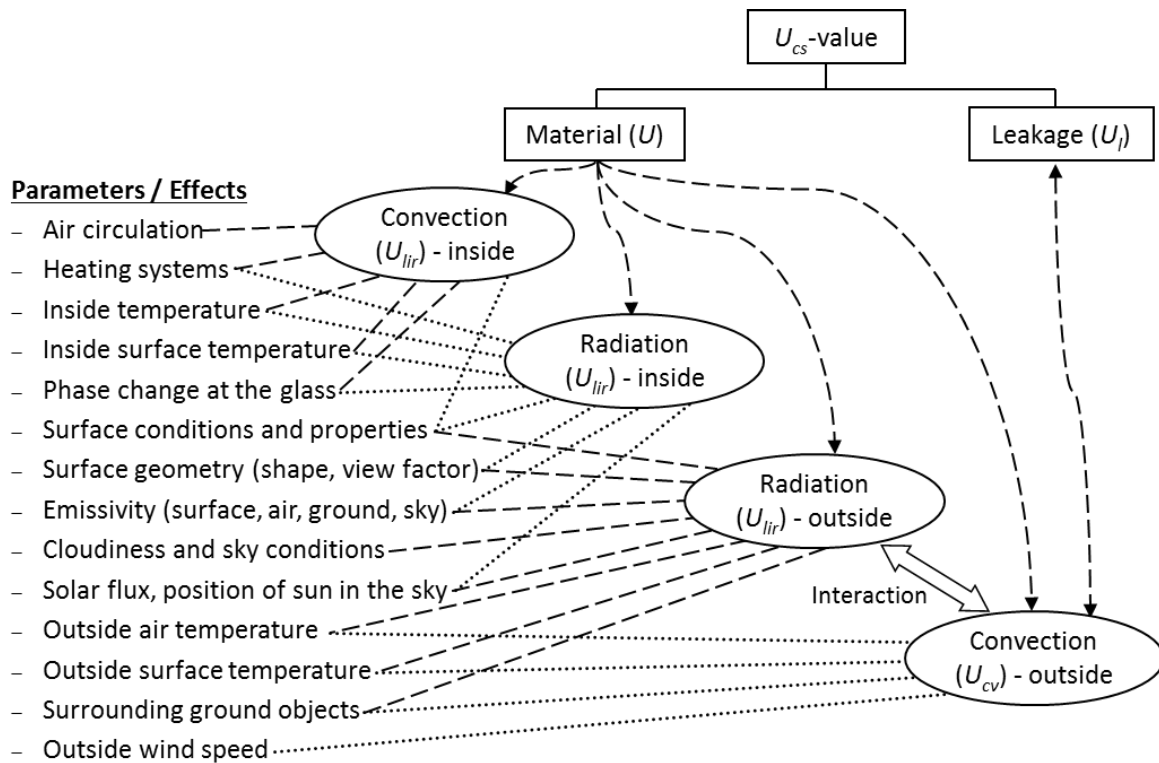
Fig. 4.3. Schematic of the heat transfer coefficients and the related parameters.

4.1.2 Calibration and preliminary tests

Initially, precalibration checks on the net radiometers were carried out before the actual measurements began. A newly acquired CNR 4 net radiometer was used to calibrate the 240-8110 net radiometer models. This was done to ascertain the estimated sensitivity values of these measuring instruments. Signal outputs from the radiometers were obtained in form of millivolts (mV) using a 6.5 digit precision multimeter (Fluke 8846A, USA). A desired response time of about 45 seconds was considered in order to achieve reliable data (Kipp & Zonen, 2009).

In order to establish the optimal positioning of the net radiometer from the cover surface, a setup with two aluminium plates was used for the study (Fig. C1, Appendix C). The schematic setup had a provision to vary the vertical height between the plates. The plates measured 0.5 m long, 0.5 m wide and 0.0025 m thick. Thermal radiation measurement is strongly temperature-dependent and high temperature difference is therefore necessary for better analysis of radiation effects. Thus, the lower plate was heated to approximately 65 °C using a Haake thermostat (Berlin, Germany). On the other hand, the upper plate was cooled to about 18 °C using the copper plate attached to the thermocouples.

Aluminium surfaces are so shiny and thus reflective in the infrared such that accurate temperature measurements are not possible. For this reason, a black paint (einzA Schultafellack, Germany) was evenly applied on the plate surfaces to avoid reflection effect during the experiment. The vertical height between the plates was subjectively set at 0.35 m, 0.50 m and 0.65 m. In addition, the position of the net radiometer was varied at a vertical distance H_1 from the lower hot plate and a distance H_2 from the upper cold plate (Fig. 4.4). The net radiation measurements above the surface of interest were similarly obtained using the precision multimeter.
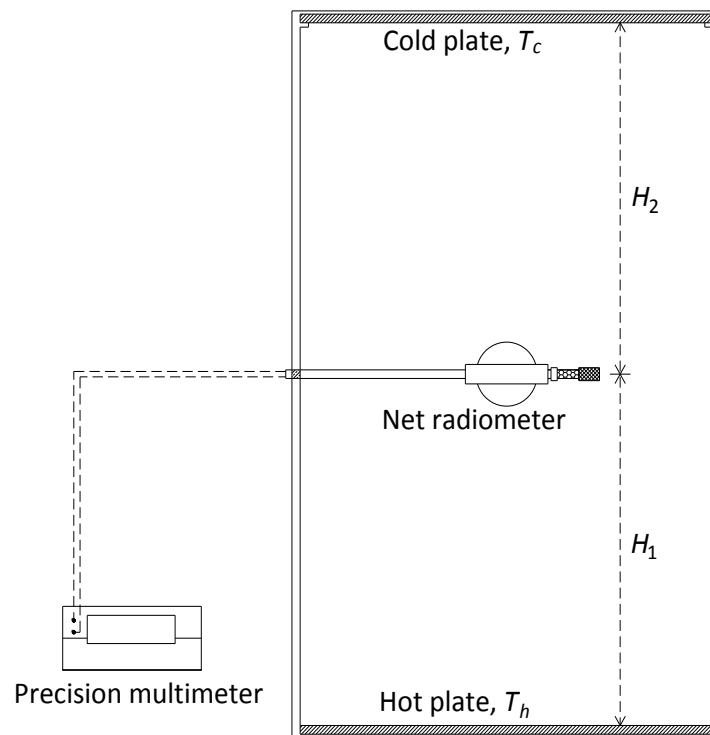
Fig. 4.4. Schematic showing the positioning of the net radiometer from the aluminium cold and hot plates.

4.2 Big Thermal Box Experiments

4.2.1 Big south-facing thermal box

A developed thermal box (Fig. 4.5) was used to represent conditions similar to those of real greenhouses. The box measured 2.4 m long, 1.9 m wide and 1.2 m high. It was inclined at 26.5° from the horizontal and oriented with the south-facing direction. The provision for mounting the cover material in the hinged lid measured 2 m long by 1.5 m wide. The cover surface is the top part of the box enclosure representing a dry

greenhouse (with no plants). A 4 mm float glass was used as the cover material with steel glazing bars being incorporated on the surface design to reinforce the glass. The area under glass and glazing bars amounted to 86 % and 14 %, respectively. An infrared thermal camera (Varioscan 3022, Jenoptic Laser, Jena, Germany) was useful for external inspection of the cover surface.

Fig. 4.5. South-facing thermal box for thermal radiation exchange measurements.

Heating elements (type 01.123: 800 W, Cr/Ni tubes, 6.9 mm diameter and 1.11 m length; type 02.251: 2000 W, Cr/Ni tubes, 8.5 mm diameter and 1.11 m length) were used to provide a heat distribution inside the box. Base plate and side walls of the developed system were made from 0.2 m thick sandwich insulation panels (ESP 040, UNIDEK GEFINEX GmbH, Steinhagen, Germany). The inner and outer surfaces of the system were lined with white lacquered aluminium sheets. To increase the reflection of longwave thermal radiation, an additional cover of unlacquered aluminium sheet was added on the interior walls (Max et al., 2012). The overall heat transfer coefficient (U_{cs}-value) measurement was conducted using this system (Langner and Rath, 2014) which was further implemented into the HORTEX tool (Rath, 1992). To avoid interference from solar radiation, the measurements were carried out at night (Tantau, 2013). A calibrated power

meter (EEM12-25 A, ShellCount, Ahrensburg, Germany) with accuracy of ±1 % was installed in the box to record the energy consumption during heating of the system. Additionally, a 1 m^2 wet felt mat was placed inside the box to generate condensation on the interior glass surface and thereby simulate crop transpiration (Max et al., 2012).

4.2.2 Measurement of parameters

4.2.2.1 Net radiation

Net radiation between the glass-covered surface and the sky was measured using net radiometers (Fig. 4.6). A CNR 4 net radiometer (Kipp & Zonen, Delft, The Netherlands) was the main instrument used in the radiation balance measurement. The CNR 4 design was such that both the upward facing and downward facing instruments measured the energy that was received from the whole hemisphere. The temperature sensors incorporated in the CNR 4's body near the pyrgeometer sensing element measured its temperature, which was taken into account in correcting the measured longwave irradiance (Kipp & Zonen, 2009). In order to obtain average net radiation values at the surface, four readily available 240-8110 net radiometers *(Schenk,* Vienna, Austria; NovaLynx Corporation, California, USA) were also utilized in the investigation. The 240-8110 net radiometer model is an instrument for direct and instantaneous determination of net radiation (difference between incident and reflected radiation) in short and long wavelength ranges. The receiver plate facing up measures shortwave global radiation and longwave radiation of the atmosphere according to its temperature. The receiver plate facing down measures reflected shortwave radiation and longwave radiation according to the temperature emitted by the surface beneath the sensor. Both of the receiver plates are electrically cross connected, thus, a direct determination of net radiation is possible.

Fig. 4.6. CNR 4 (left) and 240-8110 (right) net radiometers used in thermal radiation exchange measurements (Sources: Kipp & Zonen, 2009; NovaLynx, 2013).

The key specifications of the net radiometers used in this study are presented in Table 4.1. The two radiometer models (240-8110 and CNR 4) are intended for continuous outdoor use. Generally the accuracy of the CNR 4 is higher than that of competitive net radiometers (Kipp & Zonen, 2009). The connector with the 4 sensor outputs is indicated with an S on the back of the CNR 4 while the temperature connector is indicated with a T (Fig. C2, Appendix C).

Table 4.1. Specifications of the net radiometers used in the measurement.

Specifications	Unit	240-8110 net radiometer	CNR 4 net radiometer	
			Pyranometer	Pyrgeometer
Spectral sensitivity	µm	0.3 - >30	0.3 - 2.8	4.5 - 42
Measurement range	W m^{-2}	0 - 1500	0 - 2000	-250 - 250 (net)
Response time	s	<25	<18	<18
Cosine response	%	<5	<2	<2
Linearity	%	<2	<1	<1
Sensitivity	µV W^{-1} m^{-2}	15	10 - 20	5 - 15
Impedance	Ω	5	50 (20 - 200)	50 (20 - 200)
Ambient temperature	°C	-40 - 60	-40 - 80	-40 - 80
Temperature effect	%	<2 (-20 - 40 °C)	<4 (-10 - 40 °C)	<4 (-10 - 40 °C)
Non-stability	%	<3	<1	<1

(Sources: Kipp & Zonen, 2009; NovaLynx, 2013)

To keep the inner sensor compartment free from moisture, the 240-8110 net radiometer uses silica gel in a desiccant tube while the CNR 4 design has a drying cartridge. Horizontal adjustment for the 240-8110 model is permitted by the two bull's-eye levels while the CNR 4 model has one level with a bubble level sensitivity of < 0.5° (bubble half inside ring).

The calibration of the four-channel CNR net radiometer was done by the manufacturer and the certificate was supplied with the instrument. The sensitivity values of the upper and the lower sensors of the longwave detector (pyrgeometer) were 7.31 µV W^{-1} m^{-2} and 9.71 µV W^{-1} m^{-2}, respectively. For the shortwave detector (pyranometer), the sensitivity

values of the upper and the lower sensors were 13.58 µV W^{-1} m^{-2} and 10.83 µV W^{-1} m^{-2}, respectively. The spectral properties of the pyrgeometer are mainly determined by the properties of the absorber paint and the silicon window (Fig. C3, Appendix C). The silicon window is coated on the inside with an interference filter, which blocks the solar radiation. Theoretically, this sensitivity equals the spectral selectivity of the total instrument (Kipp & Zonen, 2009). The measurement of the radiation falling on a surface requires that the sensor has to comply with the cosine response. Between 0° and 90°, the sensitivity should be proportional to the cosine of the angle of incidence. The spectral properties of the pyranometer are mainly determined by the properties of the absorber paint and the glass dome (Fig. C4, Appendix C). The pyranometer generates a millivolt (mV) signal that is simply proportional to the incoming solar radiation. The pyranometer irradiance is expressed as (Kipp & Zonen, 2009):

$$Q_{SW} = \frac{V_{emf}}{S} \qquad (4.1)$$

where,

Q_{SW}	: pyranometer irradiance	[W m^{-2}]
V_{emf}	: output voltage	[µV]
S	: sensitivity	[µV W^{-1} m^2]

The signal that is generated by the pyrgeometer represents the exchange of far infrared (thermal) radiation between the pyrgeometer and the object that it is facing. The calculation of the far infrared irradiance is done according to the following equation (Kipp & Zonen, 2009):

$$Q_{LW} = \frac{V_{emf}}{S} + \sigma \cdot T_b^4 \qquad (4.2)$$

where,

Q_{LW}	: pyrgeometer irradiance	[W m^{-2}]
V_{emf}	: output voltage	[µV]
S	: sensitivity	[µV W^{-1} m^2]
σ	: Stefan-Boltzmann constant = $5.67 \cdot 10^{-8}$	[W m^{-2} K^{-4}]
T_b	: pyrgeometer body temperature	[K]

The CNR 4's body temperature T_b was measured with an in-built Pt-100 using the 4-wire mode as this compensates for longer wires. To obtain a signal from the Pt-100, a current of about 1 mA is fed through two wires on either side of the Pt-100. The voltage that is generated was measured using the other pair of wires which are connected in parallel with the Pt-100. T_b was then computed as (Kipp & Zonen, 2009):

$$T_b = \frac{-\alpha_{pt} + \sqrt{\alpha_{pt}^2 - 4 \cdot \beta_{pt} \cdot \left(\dfrac{-R}{x_{tr}} + 1\right)}}{2 \cdot \beta_{pt}} + c_k \qquad (4.3)$$

where,

T_b	: body temperature of CNR 4 net radiometer	[K]
R	: thermistor resistance	[Ω]
α_{pt}	: constant = 3.908 · 10^{-3} (Kipp & Zonen, 2009)	[-]
β_{pt}	: constant = -5.8019 · 10^{-7} (Kipp & Zonen, 2009)	[-]
x_{tr}	: coefficient = 100 (Kipp & Zonen, 2009)	[Ω]
c_k	: coefficient = 273.15 (Celsius to Kelvin)	[K]

4.2.2.2 Temperature

The air and surface temperatures (for glass and glazing bars) were measured with the precision temperature sensors (TS-NTC-104, Hygrosens, Germany). These sensors have a wide temperature range of -60 °C to 150 °C and with an accuracy of ±0.12 K at 25 °C. In the temperature range of -60 °C to 85 °C, the maximum error is around ±0.5 K. In comparison to other temperature sensors, the type used offers a substantially higher sensitivity and thus the desired accuracy. Due to its miniaturized dimensions (3.8 mm by 2.8 mm by 17 mm), low thermal mass and high upward gradient enables simple evaluation circuits. A small measuring current of about 0.15 mA was supplied due to its high impedance and thus the energy consumption is minimized in its application. The sensor also has a fast response time of 15 seconds. The sensors were glued to the surface using a 2-component epoxy resin adhesive (UHU plus endfest 300, Bühl/Baden, Germany) which works within 90 minutes although the setting time and final strength depend on the temperature.

Since all the data were to be relayed to a single recording point, a 4-wire method (also called Kelvin method) was used specifically for temperature measurement. This method of measurement provides the highest accuracy, since it fully compensates for cable wire resistances. For temperature measurement inside each of the miniaturized thermal boxes, the NTC sensor was situated at a height of about 20 cm above the aluminium sheet which was attached to the heating pad. In every situation, the air temperature adjacent to the measurement site was always included during the data recording.

4.2.2.3 Wind speed and direction

Outdoor wind speed and direction were measured with the Gill UVW anemometer (model 08254, R. M. Young Company, Michigan, USA). It is a three component wind instrument for direct measurement of the U, V and W orthogonal wind vectors (Fig. 4.7). Three propeller anemometers are mounted at right angles to each other on a common mast with spacing to minimize wake effects.
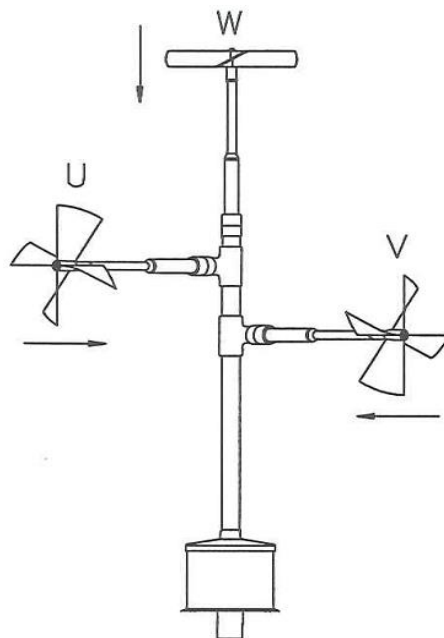
Fig. 4.7. The Gill UVW anemometer with three propellers on a common vertical mast

(Source: Manual PN 27005-90, 1994).

The individual anemometers are low threshold precision air speed measuring sensors using fast response helicoid propellers. In each anemometer, a tachometer-generator coupled to the propeller shaft converts propeller rotation to a DC voltage which is linearly

proportional to wind velocity. The horizontal U and V anemometers produce a positive output voltage with wind flow from the front of the sensor (counterclockwise propeller rotation) and a negative voltage with wind flow from behind. The socket for the vertical W anemometer is wired such that the output is negative for downdrafts and positive for updrafts.

According to the Manual PN 27005-90 (1994), the wind speed was computed from the following calibration formula:

$$v = x_w \cdot V_p \qquad\qquad\qquad (4.4)$$

where,

v : wind speed $[m\ s^{-1}]$

x_w : coefficient = 0.018 (PN 27005-90, 1994) $[m\ s^{-1}\ mV^{-1}]$

V_p : output voltage of a propeller anemometer $[mV]$

The propeller response as a function of wind angle approximates the cosine law, allowing true wind velocity and direction to be calculated (Fig. C5, Appendix C). Thus, the instrument may be oriented such that the sensor faces the prevailing wind or direction of primary interest. This minimizes non-cosine response errors and has the shortest effective distance constant. It also minimizes possible wake effect errors (Manual PN 27005-90, 1994). However, cosine correction factors are available (Table B1, Appendix B) depending on the angle between the propeller axis and the wind vector.

4.2.2.4 Cloudiness factors

Various attempts have been made to quantify cloud cover in numerical weather prediction models. The improvements of analyses and forecasts is small, yet the authors consider the procedure promising (van der Veen, 2013; Vukicevic et al., 2004; Bayler et al., 2000). Cloudiness influences the weather on earth in general and especially longwave radiation emitted by the atmosphere downward to the earth's surface. Precise estimation of cloudiness is therefore important for numerous applications in agriculture and horticulture requiring rainfall, surface radiation and energy balance.

The cloudiness factor C is a very important parameter in the longwave radiation exchange (Ronoh and Rath, 2015a). This was established using two approaches (Table 4.2). Firstly, the weather maps were acquired from the web service *Weather Online* (www.wetteronline.de) at intervals of 5 minutes. These maps provide sufficient weather elements over a geographical area at a specified time. Secondly and for purposes of comparison, cloud cover in octas (eighths) was also obtained from the German Weather Service (www.dwd.de). The hourly octa values rely on visual inspection of the sky by experienced weather watchers and express the number of eighths of the sky that is cloud-covered. Based on these octa values (ranging from 0 to 8), a cloudiness factor C_{octas} (ranging from 0 to 1) was then attained. For both cases, the hourly means were computed and used in the analysis.

Table 4.2. Approaches considered in prediction of the cloudiness factors.

No.	Approach	Frequency	Technique	Source
1	Weather watcher (octas)	Once per hour	Manual inspection	www.wetteronline.de
2	Weather maps*	Every 5 minutes	Computer-based image analysis	www.dwd.de

*Weather maps: satellite images; located in Hannover-Langenhagen Airport, Germany; resolution of 1.25 miles per pixel (2 km per pixel)

Within a given region, the weather map shows the cloud cover intensity and distribution. It also shows whether rain or snow is falling (Fig. 4.8). A green background on the map characterizes a clear-sky condition. The intensity of white, blue and pink colours vary depending on the occurrence of cloudiness, rain and snow, respectively.

(a)   (b)

(c)   (d)
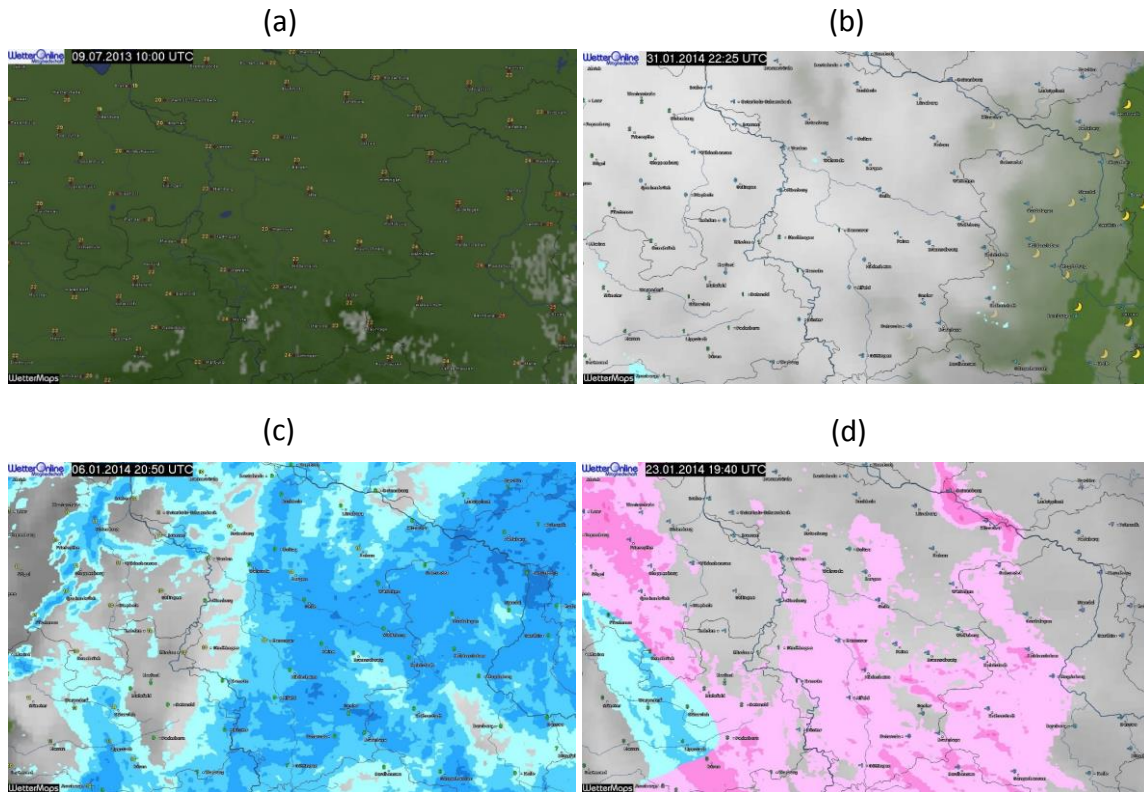
Fig. 4.8. Weather maps: (a) green background (clear-sky), (b) white showing clouds distribution and intensity, (c) blue representing rain, and (d) pink indicating presence of snow (Source: www.wetteronline.de).

A computer vision-based algorithm (Appendix D) was developed in Halcon 11.0 (HALCON 11.0.3, 2012) which identifies selected regions of interest on the maps and calculates the cloudiness situation at a given location, thus yielding a cloudiness factor C_{maps}. Halcon is generally a comprehensive standard software for machine vision with an integrated development environment that is used worldwide. Fig. 4.9 summarizes the procedure and the operators used in the developed algorithm.
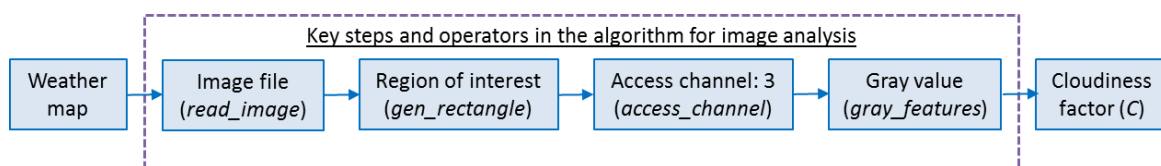
Fig. 4.9. Procedure overview for the image analysis with Halcon 11.0.

Three rectangles were subjectively set as regions of interest (Fig. 4.10). The coordinates in pixels of the chosen rectangles 1, 2 and 3 are (467, 693, 470, 700), (485, 690, 487, 694) and (489, 713, 491, 718), respectively.
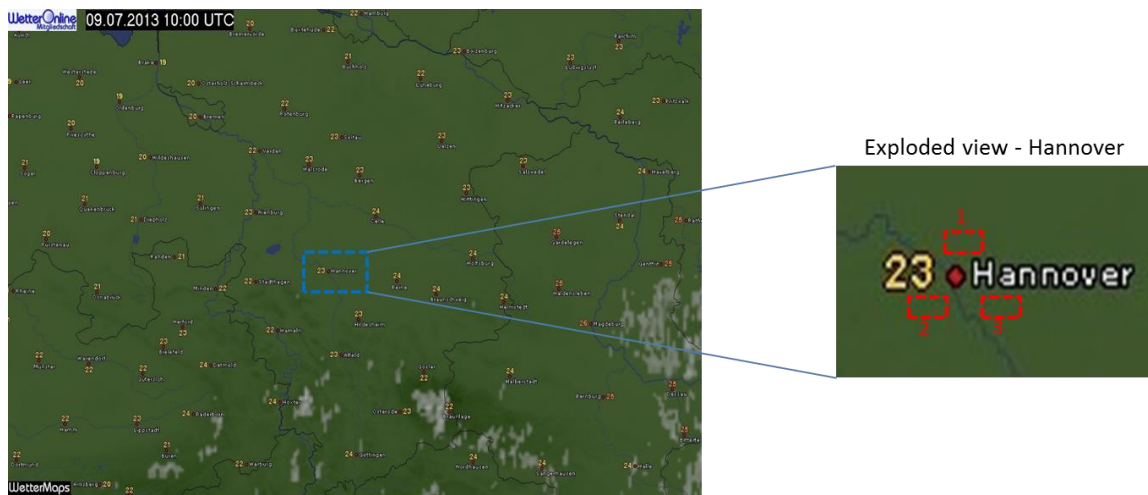
Fig. 4.10. A weather map (left) and an exploded view of the region under study (right).

A linear interpolation method was then used to compute the cloudiness factors for the three regions. This was done using the *gray_features* operator which gives the mean gray value of the selected region. RGB colour images are a combination of the three primary colours red (R), green (G) and blue (B). RGB values are positive and range from 0 to 255. Due to presence of white, blue and pink colours on the map, channel 3 (blue colour) was considered for this analysis. This channel ensured that the presence of rain on the map (intensity of blue colour) was taken into consideration while computing the cloudiness factors. The cloudiness factor *C* ranges from 0 (clear-sky) to 1 (cloudy).

$$C = C_{min} + \left(\frac{grayval - grayval_{offset}}{grayval_{max} - grayval_{offset}} \right) \cdot \left(C_{max} - C_{min} \right) \qquad (4.5)$$

where,

C	: cloudiness factor	[-]
C_{max}	: maximum cloudiness factor = 1	[-]
C_{min}	: minimum cloudiness factor = 0	[-]
$grayval$	: gray value of the region at any given time	[-]
$grayval_{offset}$	: offset gray value of green background = 35	[-]
$grayval_{max}$	: maximum possible gray value = 255	[-]

An illustration of different regions on the weather map with different intensities of white, blue and pink colours is shown in Fig. 4.11. It also includes the RGB values of these regions as read in the Halcon algorithm.
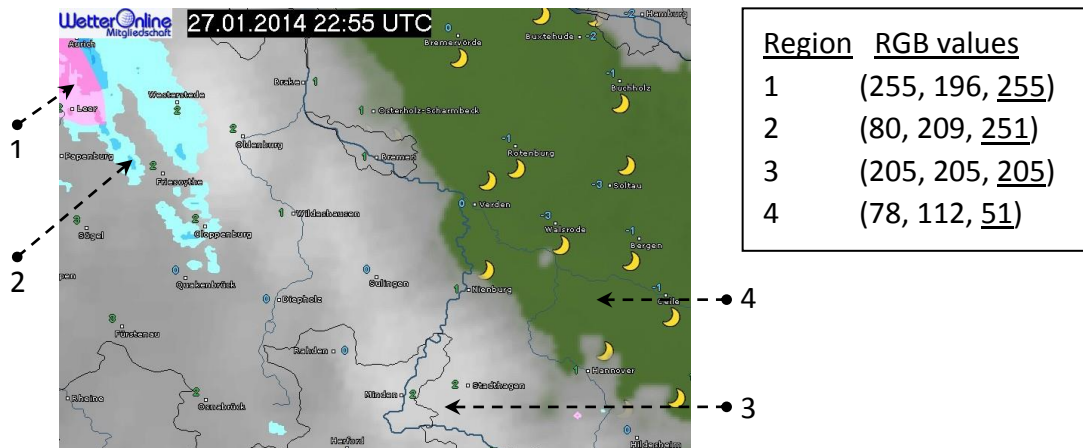
Fig. 4.11. Regions with different colours on the weather map and their RGB values.

Using an interpolation method (Eq. (4.5)), the cloudiness factor C for region 1 is computed and obtained as 1. In a similar way, the cloudiness factors for regions 2, 3 and 4 are obtained as 0.982, 0.773 and 0.073, respectively.

4.2.2.5 Relative humidity

The relative humidity RH of the surrounding air was measured with a handheld psychrometer. Two NTC temperature sensors were used in the dry bulb and the wet bulb temperature measurements. The measurements were checked with data obtained from the Institute of Meteorology and Climatology (www.imuk.de). In addition, hourly RH values were acquired through the time series category of web weather request and distribution system (WebWerdis) of the German Weather Service (www.dwd.de).

4.2.2.6 Rain

Hourly rainfall amount for the study location (Herrenhausen, Hannover) during the measurement period was computed from the measured data (recorded at 1-minute interval) provided by the Institute of Meteorology and Climatology. To counter-check the computed values, the hourly sum of precipitation (in mm) provided by the WebWerdis platform of the German Weather Service (www.dwd.de) were also obtained. This was

especially noted whenever it rained during the daytime and nighttime investigation periods.

4.2.3 Data logging

Net radiation, surface temperatures and some of the atmospheric parameters (air temperature, relative humidity, and wind speed and direction) were recorded concurrently during the measurement period. Fig. 4.12 illustrates how the required data were captured from the big south-facing thermal box. Radiation data from the net radiometers required the use of a ME-UBRE desktop relay box (Meilhaus Electronic GmbH, Alling, Germany) with 8 type C relays (5 A, 240 VAC). The 8 relays were sufficient for outputs from the four 240-8110 net radiometers and the four signal outputs of the CNR 4 net radiometer. To amplify the millivolt signal outputs of the net radiometers, a dual programmable gain instrumentation amplifier (EI-1040, LabJack Corporation, Lakewood, USA) was attached to the LabJack U12 (LabJack Corporation, Lakewood, USA) having 8 screw terminals for analog output signals. This was done by simply connecting the power and amplifier outputs to the LabJack. A gain factor of 1000 was selected and this can be programmed by the LabJack by connecting the gain select inputs GSA1 and GSA2 to the LabJack digital outputs.
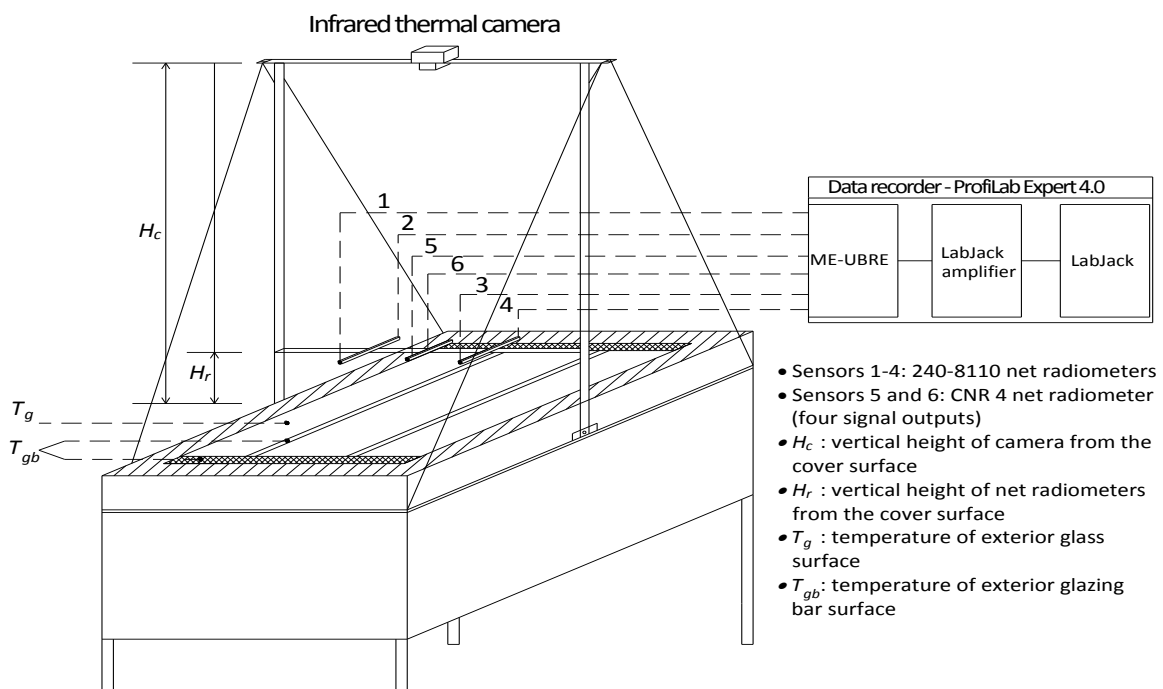
Fig. 4.12. Schematic of data relay and recording from the big thermal box.

For concurrent recording of output signals through the ME-UBRE, the LabJack amplifier and finally to the LabJack U12, the ProfiLab Expert 4.0 software (ABACOM, Ganderkesee, Germany) was used to develop a comprehensive data logging system for both analogue measurements and digital controls. The measured parameters were recorded in the range of 0 V to 10 V and the necessary calibration factors applied to obtain the actual data. The surface temperatures and the atmospheric parameters were recorded at a frequency of 15 seconds. The radiation data were measured every 30 seconds. The time interval was large for the latter since some reasonable time was necessary for the concurrent data acquisition from the 8 relays of ME-UBRE. All data were averaged to obtain the hourly means necessary to verify the radiation estimations.

4.2.4 Thermal inspection of the cover surface

Digital thermal images of the glass-covered surface were obtained using a Varioscan 3022 (Jenoptic Laser, Jena, Germany) thermoelectrically cooled infrared scanning camera with a spectral sensitivity from 2 µm to 5 µm. It operates on the principle of object scanning whereby the object is scanned through a two-dimensional reflecting scanner. It has a geometric resolution of 3 mrad, 240 x 360 pixels focal plane array and a 30° x 20° field of view. Due to this field of view, the camera was fixed at a vertical height of 2.35 m above the cover surface. To avoid any radiation influences, the images were taken from the thermal camera at a distance using an extensible air bulb remote control release (Hama, Japan). When the air bulb is squeezed (Fig. C6, Appendix C), the generated compressed air triggers the camera key in order to save the images in the appropriate storage target (memory card or internal flash memory). The minimum focus distance is 0.2 m and the temperature measuring range is -10 °C to 1200 °C. The temperature resolution at 30 °C object temperature is ±0.003 and the absolute accuracy of temperature measurement being < ±2 K (Varioscan Manual, 2000; InfraTec, 2006). A compact blackbody calibration source (M305, Mikron Instruments Inc., USA) was used to check the suitability of the thermal camera in surface temperature measurement. It has a high emissivity of 0.995 and high accuracy of ±0.25 % of reading ±1 digit.

The digital thermograms were analysed with the software package IRBIS® plus V 2.2 (InfraTec GmbH, Dresden, Germany) which allowed for correction of object emissivity

after images had been recorded (InfraTec, 2006). IRBIS® is a graphics-oriented software which is used to analyse digital thermograms. This software is the ideal tool for fast thermographic image data analysis and creating reports in a comfortable manner (InfraTec, 2006). It allows for correction of the object emissivity after images have been recorded (Oerke et al., 2005). The IRBIS® functions are operated via the pull-down menus, whose top level is a menu line and contains the different menu options. Within the work area, there is a display of the thermogram as well as a temperature scale, measuring values, profiles, a comment field and a parameter field.

The radiation received by the camera in the scanning phase consists of different fractions such as (Fig. 4.13):

a) characteristic radiation emitted by the measured object

b) radiation of surfaces in the ambience of the measured object measured by it

c) characteristic radiation of the atmosphere between object and camera
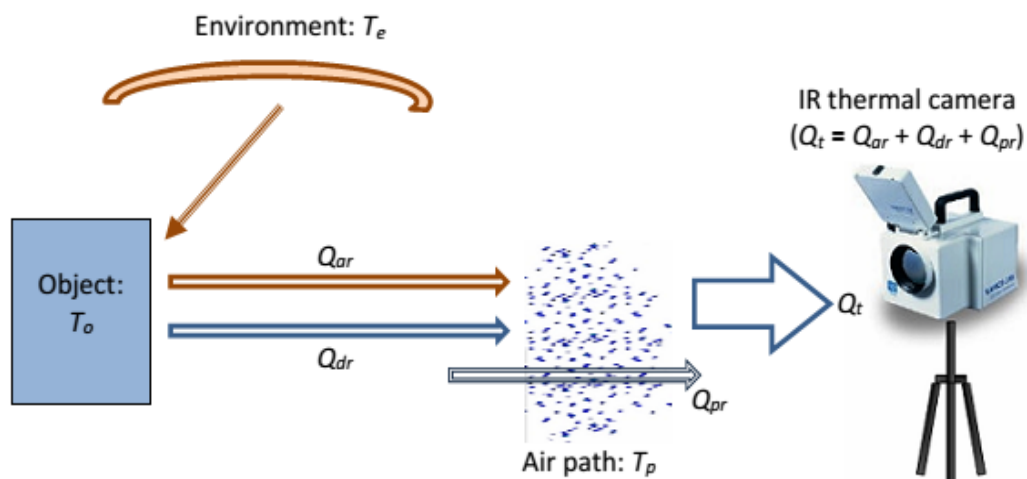
Fig. 4.13. Illustration of radiation components received by the infrared thermal camera.

where,

T_e : environmental temperature   [K]

T_o : object temperature   [K]

T_p : air path temperature   [K]

Q_{ar} : ambient radiation reflected by the object   [W m^{-2}]

Q_{dr} : direct radiation of the measured object   [W m^{-2}]

Q_{pr} : characteristic radiation of the air path   [W m^{-2}]

Q_t : total radiation measured by the camera   [W m^{-2}]

The environmental temperature T_e accounts for the temperature of objects in the ambience of the measured object emitting heat radiation that might be reflected at the surface of the measured object. This radiation will affect the object temperature measured by the thermal camera only if the set emissivity is < 1 (Varioscan Manual, 2000).

The direct radiation of measured object Q_{dr} is given by (Varioscan Manual, 2000):

$$Q_{dr} = \varepsilon_o \cdot \tau_p \cdot \sigma \cdot T_o^4 \tag{4.6}$$

where,

Q_{dr} : direct radiation of the measured object   [W m^{-2}]

ε_o : object emissivity   [-]

τ_p : transmission of the air path   [-]

σ : Stefan-Boltzmann constant = $5.67 \cdot 10^{-8}$ [W m^{-2} K^{-4}]

T_o : object temperature   [K]

The object temperature T_o and the object emissivity ε_o were considered separately for the glass and the glazing bar. The ε_o values of 0.92 and 0.96 for glass and steel glazing bar, respectively (Fluke, 2009) were used. With a known measuring distance of the camera d_c, the parameter τ_p is obtained from the following expression (Varioscan Manual, 2000):

$$\tau_p = \exp\left(\frac{-d_c}{x_l}\right) \tag{4.7}$$

where,

τ_p : transmission of the air path   [-]

d_c : measuring distance of the camera   [m]

x_l : coefficient = 1000 (Varioscan Manual, 2000) [m]

Under the prevailing air temperature T_a, the ambient radiation Q_{ar} reflected by the measured object is expressed by (Varioscan Manual, 2000):

$$Q_{ar} = (1 - \varepsilon_o) \cdot \tau_p \cdot \sigma \cdot T_a^4 \tag{4.8}$$

where,

Q_{ar} : ambient radiation reflected by the object   [W m^{-2}]

ε_o : object emissivity   [-]

τ_p	: transmission of the air path	[-]
σ	: Stefan-Boltzmann constant = $5.67 \cdot 10^{-8}$	[W m^{-2} K^{-4}]
T_a	: air temperature	[K]

Limitations of the influence of atmospheric radiation can be achieved by entering the ambient temperature into the camera but the challenge is to determine this temperature in a reliable way. It is difficult since the neighbourhood of an observed object can encompass many components of various emissivity values located close to it or farther away (Minkina and Dudzik, 2009).

The characteristic radiation of air path Q_{pr} is computed as (Varioscan Manual, 2000):

$$Q_{pr} = (1 - \tau_p) \cdot \sigma \cdot T_p^4 \tag{4.9}$$

where,

Q_{pr}	: characteristic radiation of the air path	[W m^{-2}]
τ_p	: transmission of the air path	[-]
σ	: Stefan-Boltzmann constant = $5.67 \cdot 10^{-8}$	[W m^{-2} K^{-4}]
T_p	: air path temperature	[K]

All these fractions are considered for the total radiation measured by the thermal camera Q_t and is therefore expressed by:

$$Q_t = \sigma \cdot \left\{ \tau_p \cdot \left(\varepsilon_o \cdot T_o^4 + (1 - \varepsilon_o) \cdot T_a^4 \right) + (1 - \tau_p) \cdot T_p^4 \right\} \tag{4.10}$$

where,

Q_t	: total radiation measured by the camera	[W m^{-2}]
σ	: Stefan-Boltzmann constant = $5.67 \cdot 10^{-8}$	[W m^{-2} K^{-4}]
τ_p	: transmission of the air path	[-]
ε_o	: object emissivity	[-]
T_o	: object temperature	[K]
T_a	: air temperature	[K]
T_p	: air path temperature	[K]

4.3 Small Thermal Box Experiments

4.3.1 Miniaturized thermal boxes

Four other identical thermal boxes were developed by scaling down the dimensions of the big south-facing thermal box (sub-section 4.2.1). The four boxes were necessary in order to achieve the east, west, north and south orientations, while changing the inclination angles characterizing the standard Venlo greenhouse surfaces. Each of the developed thermal boxes was 1.2 m long, 0.95 m wide and 0.6 m high (Fig. 4.14). The base and side walls of the boxes were made of Styrodur (BASF, Germany) with a thickness of 10 cm and a lightweight construction. The Styrodur also has excellent insulation properties, high compressive strength, low water absorption and resistance to aging and decay. The initial determination of the air exchange rate due to leaks with a tracer gas (Tantau, 2013) proved that the boxes were identical. The errors due to workmanship and closing of the boxes were therefore minimized as much as possible. The exterior surfaces were inclined such that they characterize the roof slope and the walls. Based on the revised German standard for Venlo greenhouses, the roof had an inclination angle of 24° (von Elsner et al., 2000; DIN 11535-2, 1994). As expected, both the side and end walls of the Venlo-type greenhouse design had an angle of 90°.

(a)   (b)
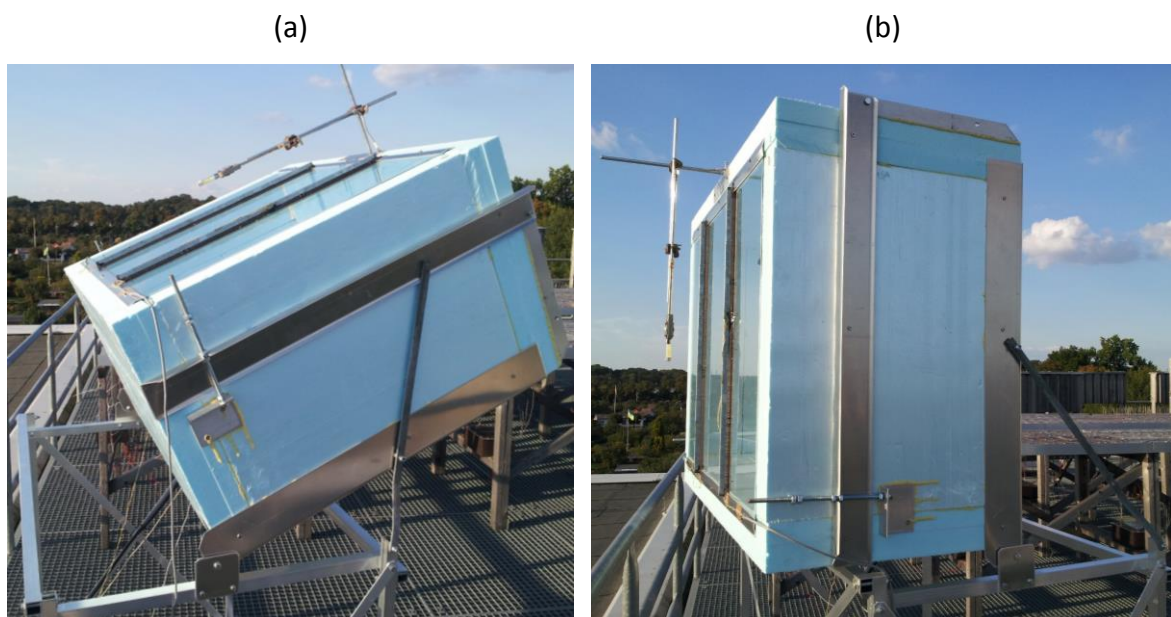
Fig. 4.14. Inclination of the miniaturized thermal box systems: (a) inclined at 24° (roof), and (b) inclined at 90° (wall).

A window heating pad (ProfiPower, axhess GmbH & Co. KG, Hausen, Germany) was attached to the bottom section inside the thermal boxes (Fig. 4.15). It was provided with 12 V DC power and in return supplied about 120 W (10 A, 12 V). The heating pad measured 40 cm by 100 cm and weighed about 0.6 kg. The maximum temperature attained by the heating pad was 55 ± 5 °C and it had an integrated thermostat for temperature control. A switch-mode DC power supply unit (model 6459, Graupner GmbH & Co. KG, Kirchheim/Teck, Germany) was used. The input voltage was 230 V while the output voltage varied between 5 V and 15 V. The output current was adjustable in the range of 0 A to 20 A. Adjustment of the voltage and ampere knobs gave the needed voltage and current values, respectively. In order to reduce the voltage drop, each DC power supply unit was connected to the heating pad using a twin wire cable of 6 mm^2 cross-sectional area and approximately 46 m length. To ensure uniform heat distribution within the box, an aluminium sheet was attached firmly to the upper side of the heating pad. The aluminium sheet was 0.98 m long, 0.65 m wide and 0.003 m thick.
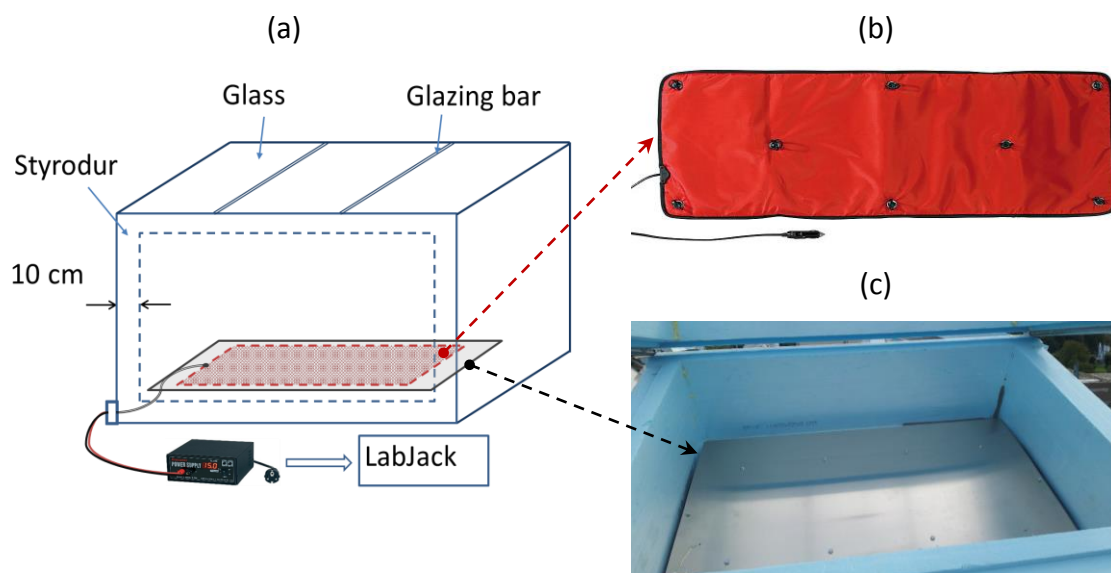
Fig. 4.15. The heating system components: (a) schematic illustration, (b) heating pad, and (c) aluminium sheet attached to the pad and fixed inside the box.

In order to avoid obstructions from buildings and trees, an appropriate rooftop was selected (Fig. 4.16). This was on top of one of the buildings at the Faculty of Architecture and Landscape Sciences, Leibniz Universität Hannover. The site's proximity to the previous study location made it easier to coordinate the experiments with the instruments

involved. Measurements were carried out exclusively at night since heating of the boxes was necessary. This also ensured that the boxes were not subjected to solar radiation effects which would predominantly favour the thermal box inclined to the south.

Fig. 4.16. An arrangement of the miniaturized thermal boxes oriented horizontally.

4.3.2 Temperature regulation in the boxes

During the measurement period (October 2014 to March 2015), temperature regulation was necessary to ensure that the inside temperatures in all the four thermal boxes were similar at any given time. This regulation was done with the ProfiLab Expert 4.0 program by setting the inside temperature T_i to 8 K above the ambient air temperature T_a. The program ensured that the heating pad in the boxes remained heated whenever the interior air temperature dropped below the set-point.

With an output current of approximately 8 A from the DC power supply, four modular monostable DIN relays (22 Series DPST-NO, FINDER GmbH, Trebur-Astheim, Germany) were connected in between the ME-UBRE relay box (Meilhaus Electronic GmbH, Alling, Germany) and the power supply units. The DIN relays used are equipped with 20 A, 250 V AC contacts rated at 5000 VA AC1 and are ideal for use in commercial applications including heating, air conditioning and lighting. They were also suitable for this regulation since their operating temperature range is -40 °C to 40 °C.

4.3.3 Variation of surface inclination and orientation

This approach enabled a proper evaluation of the variations in key parameters at the external surfaces due to varied inclination and orientation. The measured parameters

included net radiation, air temperature, inside and surface temperatures of the boxes, and wind speeds at different directions (similar methods as explained in sub-section 4.2.2). The output net radiation signals were relayed through the ME-UBRE and the LabJack amplifier to the LabJack U12. The other output signals for temperature and wind speed were relayed directly to the LabJack U12 (Fig. 4.17).
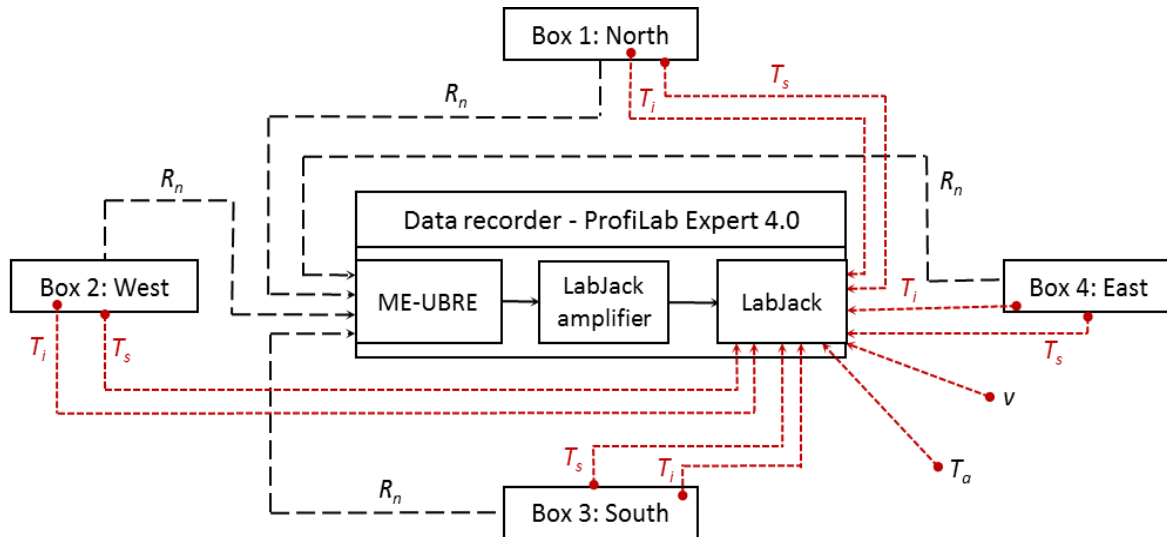
Fig. 4.17. Schematic of data relay and recording from the miniaturized thermal boxes.

where,

R_n	: net radiation	[W m^{-2}]
T_a	: air temperature	[K]
T_i	: inside temperature	[K]
T_s	: surface temperature	[K]
v	: wind speed	[m s^{-1}]

The temperature difference between the surface and the surrounding air $\Delta T_{s\text{-}a}$ was simply computed as:

$$\Delta T_{s-a} = T_{s,eff} - T_a \qquad (4.11)$$

where,

$\Delta T_{s\text{-}a}$	: surface-to-air temperature difference	[K]
$T_{s,eff}$	: effective surface temperature	[K]
T_a	: air temperature	[K]

The wind speed data made it possible to know the frequency of wind direction and to further categorize the wind speeds into four classes (0 m s^{-1} - <1.5 m s^{-1}, 1.5 m s^{-1} - <3 m s^{-1}, 3 m s^{-1} - <4.5 m s^{-1} and 4.5 m s^{-1} - <6 m s^{-1}). At both 24° and 90° surface inclination angles, the thermal boxes were randomly oriented in order to obtain several combinations necessary for detailed analysis and comparison. The boxes were rotated after every three days such that at the end of the measurement period each box had faced all the four directions (Fig. 4.18). In this case, the rotation was only meant for the box orientations while maintaining the two inclinations (roof and wall).
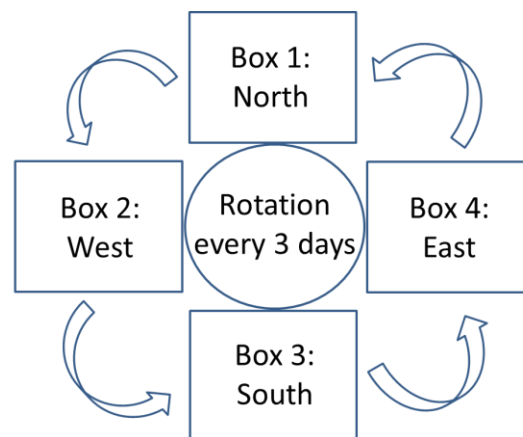
Fig. 4.18. Setup for rotation of the miniaturized thermal boxes.

4.4 Modelling of Thermal Radiation Exchange

4.4.1 Radiation modelling under night situation

The critical parameters required for modelling of the longwave radiation components (downwelling and upwelling) at night include:

   a) Surface properties: emissivity, temperature, inclination angle, surface area

   b) Meteorological variables: air temperature, dew point temperature, relative humidity, water vapour pressure of the air, cloudiness

   c) Sky and related atmospheric parameters: sky temperature, sky emissivity, clear-sky atmospheric emissivity, effective atmospheric emissivity

   d) Properties of the surroundings: ground temperature, emissivity of ground objects

   e) View factor of the glass-covered surface to: the sky, the air and the ground

The effective atmospheric emissivity is required in computation of the downwelling longwave radiation under all-sky (overcast and clear-sky) conditions. It is often computed

based on ground-based meteorological observations and is particularly a function of the cloudiness factor C and a basic clear-sky atmospheric emissivity ε_{cs} (Duarte et al., 2006). Since it is difficult to determine the bulk emissivity and the effective temperature of a vertical column of the atmosphere (Crawford and Duchon, 1999), parameterizations based on the screen level air temperature T_a and the vapour pressure e_a are commonly used. Thus, the following 10 commonly used parameterizations were selected for the calculation of the ε_{cs} (Table 4.3). The best ε_{cs} parameterization was chosen based on statistical criteria (BIAS, RMSE, MAE, PMRE and R^2).

Table 4.3. Parameterizations for clear-sky atmospheric emissivity suggested by different authors.

Author	Equation	No.
Swinbank (1963)	$\varepsilon_{cs} = y_{d,1} \cdot T_a^2$	(4.12)
Idso and Jackson (1969)	$\varepsilon_{cs} = 1 - 0.261 \cdot \exp\left(- y_{d,2} \cdot (y_{t,1} - T_a)^2\right)$	(4.13)
Brutsaert (1975)	$\varepsilon_{cs} = y_{p,2} \cdot \left(\dfrac{e_a}{T_a}\right)^{1/7}$	(4.14)
Idso (1981)	$\varepsilon_{cs} = 0.70 + y_{p,3} \cdot e_a \cdot \exp\left(\dfrac{y_{t,2}}{T_a}\right)$	(4.15)
Sugita and Brutsaert (1993)	$\varepsilon_{cs} = y_{p,4} \cdot \left(\dfrac{e_a}{T_a}\right)^{0.0687}$	(4.16)
Prata (1996)	$\varepsilon_{cs} = 1 - \left(1 + y_{p,5} \cdot \dfrac{e_a}{T_a}\right) \cdot \exp\left(-\left(1.2 + y_{p,6} \cdot \dfrac{e_a}{T_a}\right)^{0.5}\right)$	(4.17)
Iziomon et al. (2003)	$\varepsilon_{cs} = 1 - X_s \cdot \exp\left(\dfrac{-Y_s \cdot e_a}{T_a}\right)$	(4.18)
Duarte et al. (2006)	$\varepsilon_{cs} = y_{p,7} \cdot \left(\dfrac{e_a}{T_a}\right)^{0.131}$	(4.19)
Kruk et al. (2010)	$\varepsilon_{cs} = y_{p,8} \cdot \left(\dfrac{e_a}{T_a}\right)^{0.202}$	(4.20)
Dos Santos et al. (2011)	$\varepsilon_{cs} = y_{p,9} \cdot \left(\dfrac{e_a}{T_a}\right)^{0.0881}$	(4.21)

where,

ε_{cs}	: clear-sky atmospheric emissivity	[-]
e_a	: water vapour pressure of air	[Pa]
T_a	: air temperature	[K]
$y_{d,1}$	: coefficient = $9.365 \cdot 10^{-6}$ (Swinbank, 1963)	[K^{-2}]
$y_{d,2}$	: coefficient = $7.77 \cdot 10^{-4}$ (Idso and Jackson, 1969)	[K^{-2}]
$y_{t,1}$	: coefficient = 273 (Idso and Jackson, 1969)	[K]
$y_{p,2}$	: coefficient = 0.643 (Brutsaert, 1975)	[K$^{1/7}$ Pa$^{-1/7}$]
$y_{p,3}$	: coefficient = $5.95 \cdot 10^{-7}$ (Idso, 1981)	[Pa^{-1}]
$y_{t,2}$	: coefficient = 1500 (Idso, 1981)	[K]
$y_{p,4}$	: coefficient = 0.714 (Sugita and Brutsaert, 1993)	[K$^{0.0687}$ Pa$^{-0.0687}$]
$y_{p,5}$	: coefficient = 0.465 (Prata, 1996)	[K Pa^{-1}]
$y_{p,6}$	: coefficient = 1.395 (Prata, 1996)	[K Pa^{-1}]
$y_{p,7}$	: coefficient = 0.625 (Duarte et al., 2006)	[K$^{0.131}$ Pa$^{-0.131}$]
$y_{p,8}$	: coefficient = 0.576 (Kruk et al., 2010)	[K$^{0.202}$ Pa$^{-0.202}$]
$y_{p,9}$	: coefficient = 0.6905 (Dos Santos et al., 2011)	[K$^{0.0881}$ Pa$^{-0.0881}$]
X_s	: site-dependent coefficient (Iziomon et al., 2003)	[-]
Y_s	: site-dependent coefficient (Iziomon et al., 2003)	[K hPa^{-1}]

The values of the site-dependent coefficients X_s and Y_s in the algorithm of Iziomon et al. (2003) were extrapolated for the study location from the given values at lowland (212 m elevation) and mountain (1489 m elevation) sites. Considering the new parameterization for a clear-sky atmospheric emissivity ε_{cs} (Iziomon et al., 2003), the X_s and Y_s values for the lowland site are 0.35 K hPa^{-1} and 10 K hPa^{-1}, respectively, while the corresponding values for the mountain site are 0.43 K hPa^{-1} and 11.5 K hPa^{-1}, respectively. The parameterization by Iziomon et al. (2003) is unique since it includes the cloud cover and the elevation of the study sites. From the point of view of climatic characteristics, the variables utilized in the ε_{cs} parameterizations showed a strong dependence on the site elevation.

For all-sky conditions, the effective atmospheric emissivity ε_a is very necessary in modelling the longwave radiation from the sky. It is often applicable at the lower boundary of the atmosphere (Staley and Jurica, 1972). The ε_a is a function of the

cloudiness factor C and a basic clear-sky atmospheric emissivity ε_{cs}. The best ε_{cs} parameterization (out of the 10 parameterizations presented in Table 4.3) was used in the calculation of ε_a. The statistical criteria (BIAS, RMSE, MAE and PMRE) gave a hint of the particular parameterization with the best goodness of fit.

The ε_a formulation has the basic structure expressed by (Duarte et al., 2006):

$$\varepsilon_a = \varepsilon_{cs} \cdot \left(1 + b \cdot C^d\right) \tag{4.22}$$

where,

ε_a	: effective atmospheric emissivity	[-]
ε_{cs}	: clear-sky atmospheric emissivity	[-]
b, d	: constants determined experimentally	[-]
C	: cloudiness factor	[-]

The locally calibrated values of b and d for the study site were found to be 0.24 and 0.58, respectively.

Sky conditions were modelled on the basis of the cloudiness factor C, which is a very important parameter in the longwave radiation exchange. From the initial findings on some nighttime measurements (Fig. C7, Appendix C), the longwave radiation received at the surface depends on the fractional cloud cover (in octas). The nights were representative of the different air temperature and cloudiness conditions. Cloudiness greatly affects the magnitude of downwelling longwave radiation received at the surface of the earth. Therefore, cloudiness should be considered while modelling the downwelling longwave radiation. The positive relationship of the radiation with the air temperature and cloudiness (Guest, 1998) indicates that empirical models can be used in the simulation under all-sky conditions.

Another important parameter is the emissivity of surrounding ground objects ε_{gnd}. An emissivity ε_{gnd} of 0.97 was suggested by Howard and Stull (2013) particularly for tree temperatures ranging from -10 °C to 10 °C. This value was used throughout this study, since a perfect blackbody is rare in nature (Petty, 2006).

The sky emissivity ε_{sky} is necessary in a quantitative understanding of the sky radiation. It can be approximated as a function of the dew point temperature (Chen et al., 1995; Kimball et al., 1982), which is defined by the temperature and the relative humidity of air.

$$\varepsilon_{sky} = 0.732 + x_3 \cdot \left(\theta_o - \left(\frac{y_0 - RH}{z_0} \right) \right) \tag{4.23}$$

where,

ε_{sky}	: sky emissivity	[-]
θ_o	: outside air temperature	[°C]
x_3	: coefficient = 0.0063 (Chen et al., 1995)	[°C^{-1}]
y_0	: coefficient = 100 (Kimball et al., 1982)	[%]
z_0	: coefficient = 5 (Kimball et al., 1982)	[% °C^{-1}]
RH	: relative humidity	[%]

Also important is the emissivity of the cover surface ε_s, which includes glass and glazing bar. Emissivity values of 0.92 and 0.96 for glass and steel glazing bar, respectively were obtained from Fluke Corporation (Fluke, 2009).

Considering the surface inclination angle β, the view factors to the sky F_{sky}, the air F_a and the ground F_{gnd} can be calculated as (Romila, 2012; EnergyPlus 8.0, 2013; Walton, 1983):

$$F_{sky} = a \cdot \cos^2 \left(\frac{\beta}{2} \right) \tag{4.24}$$

$$F_{air} = (1 - a) \cdot \cos^2 \left(\frac{\beta}{2} \right) \tag{4.25}$$

$$F_{gnd} = \sin^2 \left(\frac{\beta}{2} \right) \tag{4.26}$$

where,

F_{sky}	: view factor to the sky	[-]
F_{air}	: view factor to the air	[-]
F_{gnd}	: view factor to the ground	[-]
a	: factor splitting sky and ambient radiation	[-]
β	: inclination angle of surface from horizontal	[°]

According to the recent literature (EnergyPlus 8.0, 2013), the factor a splits the sky and ambient radiation and is dependent as well on the inclination angle β (Walton, 1983). The simplified form of this splitting factor is given by:

$$a = \cos\left(\frac{\beta}{2}\right)$$
(4.27)

where,

a : factor splitting sky and ambient radiation [-]

β : inclination angle of surface from horizontal [°]

Apart from the measured surface temperature T_s, the ground temperature T_{gnd} was estimated from the air temperature (EnergyPlus 8.0, 2013; Kehrer and Schmidt, 2008). Modelling of longwave radiation exchange between the outside surfaces and the sky requires the knowledge of the sky temperature (Ronoh and Rath, 2015a). The equivalent sky temperature T_{sky} has been estimated differently by various researchers. The common equations applied in the T_{sky} computation (sub-section 2.4.1) are empirical in nature and are related to the air temperature. Thus, they perform best for areas with radiative climate similar to the one for which they were originally obtained. Hence, the available model by von Elsner (1982) was selected since it was developed within the same study location. Other than the air temperature, this model utilizes a cloudiness factor as an important factor in the T_{sky} estimation. Thus, for all-sky conditions, T_{sky} was expressed as (von Elsner, 1982):

$$T_{sky} = \left(y_{c,1} \cdot \theta_o + x_{a,1} + C \cdot (x_{a,2} + y_{c,2} \cdot \theta_o)\right) + c_k$$
(4.28)

where,

T_{sky} : sky temperature [K]

θ_o : outside air temperature [°C]

C : cloudiness factor [-]

$y_{c,1}$: coefficient = 1.2 (von Elsner, 1982) [-]

$y_{c,2}$: coefficient = -0.26 (von Elsner, 1982) [-]

$x_{a,1}$: coefficient = -21.4 (von Elsner, 1982) [°C]

$x_{a,2}$: coefficient = 20.6 (von Elsner, 1982) [°C]

c_k : coefficient = 273.15 (Celsius to Kelvin) [K]

Considering an exterior surface and the relevant parameters, the thermal radiation exchange at the surface Q_s is the sum of the components due to the exchange with the sky, the air and the ground.

$$Q_s = \varepsilon_s \cdot \sigma \cdot \left\{ \varepsilon_{sky} \cdot F_{sky} \cdot \left(T_s^4 - T_{sky}^4\right) + \varepsilon_a \cdot F_{air} \cdot \left(T_s^4 - T_a^4\right) + \varepsilon_a \cdot F_{gnd} \cdot \left(T_s^4 - T_{gnd}^4\right) \right\} \quad (4.29)$$

where,

Q_s	: thermal radiation exchange	[W m^{-2}]
σ	: Stefan-Boltzmann constant = $5.67 \cdot 10^{-8}$	[W m^{-2} K^{-4}]
ε_s	: surface emissivity	[-]
ε_{sky}	: sky emissivity	[-]
ε_a	: effective atmospheric emissivity	[-]
F_{sky}	: view factor to the sky	[-]
F_{air}	: view factor to the air	[-]
F_{gnd}	: view factor to the ground	[-]
T_s	: surface temperature	[K]
T_{sky}	: sky temperature	[K]
T_a	: air temperature	[K]
T_{gnd}	: ground temperature	[K]

Since the cover surface is composed of 86 % glass and 14 % glazing bars with the respective emissivity and surface temperature, the effective thermal radiation exchange $Q_{s,eff}$ was then calculated as:

$$Q_{s,eff} = y_{c,6} \cdot Q_{s,g} + y_{c,7} \cdot Q_{s,gb} \quad (4.30)$$

where,

$Q_{s,eff}$	: effective thermal radiation exchange	[W m^{-2}]
$Q_{s,g}$	: thermal radiation exchange of glass	[W m^{-2}]
$Q_{s,gb}$	: thermal radiation exchange of glazing bars	[W m^{-2}]
$y_{c,6}$	: coefficient = 0.86 (fraction of glass)	[-]
$y_{c,7}$	: coefficient = 0.14 (fraction of glazing bars)	[-]

For all-sky conditions, the downwelling longwave radiation LWR_d has the general form given by (Choi et al., 2008; Dos Santos et al., 2011):

$$LWR_d = \varepsilon_a \cdot \sigma \cdot T_a^4 \qquad\qquad (4.31)$$

where,

LWR_d : downwelling longwave radiation   [W m^{-2}]

ε_a : effective atmospheric emissivity   [-]

σ : Stefan-Boltzmann constant = 5.67 · 10^{-8} [W m^{-2} K^{-4}]

T_a : air temperature   [K]

According to Howard and Stull (2013), longwave radiation from the surrounding objects such as trees can enhance the total downwelling longwave radiation $LWR_{d,t}$ and should not be neglected. This is specifically added for comparison with the measurement from the net radiometer. $LWR_{d,t}$ is therefore expressed as:

$$LWR_{d,t} = LWR_d + \varepsilon_{gnd} \cdot F_{gnd} \cdot \sigma \cdot T_a^4 \qquad\qquad (4.32)$$

where,

$LWR_{d,t}$: total downwelling longwave radiation   [W m^{-2}]

LWR_d : downwelling longwave radiation   [W m^{-2}]

ε_{gnd} : ground emissivity   [-]

F_{gnd} : view factor to the ground   [-]

σ : Stefan-Boltzmann constant = 5.67 · 10^{-8} [W m^{-2} K^{-4}]

T_a : air temperature   [K]

An additional term accounting for the reflected downwelling radiation is incorporated in computation of the upwelling longwave radiation (Tang and Li, 2008). From the equations above, the sum of the emitted longwave radiation by the surface LWR_u and the reflected downwelling longwave radiation gives the total upwelling longwave radiation $LWR_{u,t}$ (Liang, 2004). The difference in all upwelling radiation and all downwelling radiation must result in $Q_{s,eff}$. Thus the $LWR_{u,t}$ is expressed in the form given by:

$$LWR_{u,t} = LWR_u + \left(1 - \varepsilon_s\right) \cdot LWR_d = Q_{s,eff} + LWR_d \qquad\qquad (4.33)$$

where,

$LWR_{u,t}$: total upwelling longwave radiation   [W m^{-2}]

LWR_u : upwelling longwave radiation   [W m^{-2}]

ε_s : surface emissivity   [-]

LWR_d : downwelling longwave radiation   [W m^{-2}]

$Q_{s,eff}$: effective thermal radiation exchange   [W m^{-2}]

4.4.2 Radiation modelling under day situation

In addition to the parameters for modelling of the downwelling and the upwelling longwave radiation (sub-section 4.4.1), the solar radiation requirements include:

a) Meteorological data: global radiation, diffuse radiation and direct (beam) radiation

b) Location and time-related parameters: day of the year, solar declination, latitude, longitude, hour angle, zenith angle, solar altitude, angle of incidence

c) Derived parameters: clearness index, diffuse fraction

d) Other properties: ground reflectivity, albedo of the earth surface

e) Conversion factors (horizontal to tilted surfaces) for: diffuse, direct and ground reflected radiation components

Due to a limited availability of diffuse radiation data, decomposition models have been developed to predict the diffuse radiation using the measured global data (Wong and Chow, 2001). These models are based on some key parameters which include the clearness index and the diffuse fraction. There is need to recalibrate these parameters for the study location in order to account for local climatic differences (Jacovides et al., 2006). The relationship between the diffuse fraction F_d and the clearness index I_c was established by using daily diffuse and global radiation data for the 5-year period (2009 to 2013). The data was obtained from the Institute of Meteorology and Climatology, Leibniz Universität Hannover. According to Jawarneh et al. (2012) and Jacovides et al. (2006), a polynomial correlation explains the relationship between F_d and I_c. The following 4th order polynomial correlation was fitted to the data.

$$F_d = a_0 + a_1 \cdot I_c + a_2 \cdot I_c^2 + a_3 \cdot I_c^3 + a_4 \cdot I_c^4 \qquad (4.34)$$

where,

F_d : diffuse fraction   [-]

I_c : clearness index   [-]

$a_0, ..., a_4$: empirical constants   [-]

The coefficients a_1, a_1, a_2, a_3 and a_4 can be experimentally obtained for the study location.

From individual daily global and diffuse solar radiation measurements, the diffuse fraction F_d as a function of the clearness index I_c was computed and the trend is as presented in Fig. 4.19. As expected, both F_d and I_c ranged between 0 and 1. The figure shows the scatter plot of the data and the fitted line (dashed line) resulting from the 4th order polynomial correlation. The polynomial correlation fits well for the I_c in the range of 0 and 0.75. This correlation is necessary in the calculation of the diffuse radiation.

$$F_d = 0.985 + 0.467 \cdot I_c - 3.156 \cdot I_c^2 + 0.248 \cdot I_c^3 + 1.525 \cdot I_c^4$$
$$R^2 = 0.913$$
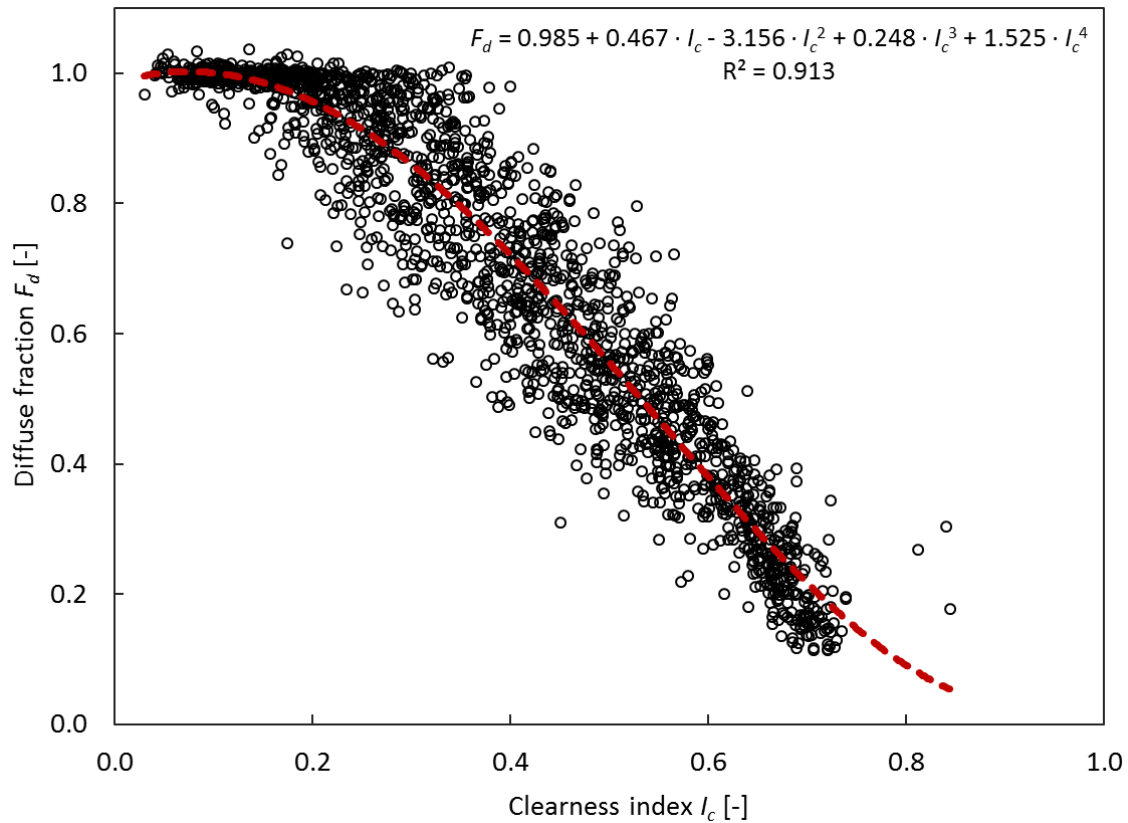
Fig. 4.19. Relationship between the diffuse fraction and the clearness index (n = 1935).

According to El-Sebaii et al. (2010), estimation of total solar radiation incident on tilted surfaces can be expressed as:

$$I_{t,t} = I_{b,h} \cdot \psi_b + I_{d,h} \cdot \psi_d + I_{g,h} \cdot \rho_g \cdot \psi_r \qquad (4.35)$$

where,

$I_{t,t}$	: total solar radiation on the tilted surface	[W m^{-2}]
$I_{b,h}$	: beam radiation	[W m^{-2}]
$I_{d,h}$	: diffuse radiation	[W m^{-2}]
$I_{g,h}$	: global radiation on a horizontal surface	[W m^{-2}]
ρ_g	: ground reflectivity	[-]

Ψ_b : beam radiation conversion factor   [-]

Ψ_d : diffuse radiation conversion factor   [-]

Ψ_r : ground reflected radiation conversion factor [-]

The radiation conversion factors (Ψ_b, Ψ_d and Ψ_r) are useful in transforming the horizontal solar radiation components to compute the total solar irradiance on the tilted surfaces. In Eq. (4.35), the diffuse radiation $I_{d,h}$ was computed using the horizontal global radiation and the diffuse fraction F_d obtained from the polynomial correlation (see Fig. 4.19). Since F_d expresses the ratio of diffuse-to-global solar radiation (Jacovides et al., 2006), the diffuse radiation was thus calculated as:

$$I_{d,h} = I_{g,h} \cdot F_d$$ (4.36)

where,

$I_{d,h}$: diffuse radiation   [W m^{-2}]

$I_{g,h}$: global radiation on a horizontal surface   [W m^{-2}]

F_d : diffuse fraction   [-]

For a surface with a given orientation, the daily value of Ψ_b is related to the time variation of incident beam radiation, the intensity of which on the ground level is a function of the atmospheric transmittance (Yang et al., 2012). With an angle of incidence θ, a zenith angle θ_z and an inclination angle β, the radiation conversion factors are given by (El-Sebaii et al., 2010):

$$\psi_b = \frac{\cos \theta}{\cos \theta_z}$$ (4.37)

$$\psi_d = \frac{1 - \cos \beta}{2}$$ (4.38)

$$\psi_r = \frac{1 + \cos \beta}{2}$$ (4.39)

where,

Ψ_b : beam radiation conversion factor   [-]

Ψ_d : diffuse radiation conversion factor   [-]

Ψ_r : ground reflected radiation conversion factor [-]

θ : angle of incidence   [°]

θ_z : zenith angle   [°]

β : angle of inclination from horizontal   [°]

An average albedo value α_s of 0.2 was used in this study for sites which are not cultivated and have a low vegetation cover and (Campbell and Norman, 1998; Scharmer and Greif, 2000). This value is therefore applicable for fields where grass is present. The upwelling shortwave radiation is the reflected global radiation and is simply given by the relation:

$$I_{ref,t} = \alpha_s \cdot I_{t,t} \tag{4.40}$$

where,

$I_{ref,t}$: reflected radiation from a tilted surface   [W m^{-2}]

α_s : albedo of the earth surface   [-]

$I_{t,t}$: total solar radiation on the tilted surface   [W m^{-2}]

4.4.3 Model sensitivity analysis

One-at-a-time (OAT) sensitivity analysis was conducted for a number of selected atmospheric parameters influencing longwave radiation models. As the name suggests, the OAT approach allows only one parameter to vary each time, ignoring the effects of parameter interactions and multi-response interdependences (Saltelli et al., 2010). This simple, preliminary analysis facilitated the identification a subset of potentially important parameters for the longwave radiation modelling. The atmospheric parameters considered for the OAT analysis included air temperature T_a, cloudiness factor C and relative humidity RH. Appropriate lower and upper boundaries (the feasible ranges) for the selected parameters were carefully derived based on the data acquired during the measurement period. The chosen ranges of T_a, C and RH were 253.15 K to 293.15 K, 0 to 1 and 20 % to 100 %, respectively. To represent a heating situation, the surface-to-air temperature difference ΔT_{s-a} was subjectively set in the range of 273.15 K to 289.15 K. The OAT analysis was done such that the longwave radiation model was run repeatedly for a number of times while varying a single parameter from the lower bound to the upper bound. A middle base value was selected within the feasible range each time while all the other parameters were fixed.

A sensitivity index (SI) is an effective way to judge the model sensitivity (DeVisser, 2010; Saltelli et al., 2004; Hamby, 1994). SI is a dimensionless index which was calculated as the ratio between the relative change of model output and the relative change of a parameter (Lenhart et al., 2002). Elasticity of a variable with respect to a parameter is a simple example of a SI. The higher the elasticity, the higher the sensitivity of results to changes in that parameter. According to Millington et al. (2009), the SI can be computed as:

$$SI = \frac{\Delta Y_{b,i} / Y_b}{\Delta X_{b,i} / X_b}$$
(4.41)

where,

SI	: sensitivity index	[-]
$\Delta Y_{b,i}$	: change in dependent output state variable	[-]
Y_b	: base value of dependent variable	[-]
$\Delta X_{b,i}$	: change in parameter from the base value	[-]
X_b	: base value of parameter	[-]

In this case, $\Delta Y_{b,i} = Y_b - Y_i$ and $\Delta X_{b,i} = X_b - X_i$, with Y_i and X_i being the instantaneous values of the model output variable and parameter, respectively. Index b signifies the set base (in this case the median) while index i is the instantaneous model run being analysed. The major advantage of the median as the centre of a distribution (base value) is its relative insensitivity to extreme values (Foussier, 2006).

According to Lenhart et al (2002), the calculated sensitivity indices can be assessed by ranking them into four classes (Table 4.4).

Table 4.4. Sensitivity classes for assessing sensitivity indices.

Class	Sensitivity index, SI [-]	Sensitivity
I	$0.00 \leq |SI| < 0.05$	Small to negligible
II	$0.05 \leq |SI| < 0.20$	Medium
III	$0.20 \leq |SI| < 1.00$	High
IV	$|SI| \geq 1.00$	Very high

4.4.4 Statistical analysis

All measurements were conducted with hourly replications for each measured parameter considered in this study. Differences among treatments were evaluated using an analysis of variance (ANOVA) procedure. The Student's *t*-test was used in conjunction with the ANOVA to determine the differences between means. Another key aspect used in interpreting the test statistics was the *p*-value. Regression procedures (linear, multiple linear or polynomial) were useful for the modelling and analysis of numerical data (dependent and independent variables). The statistical analyses were performed with SigmaPlot version 11.0 (Systat Software, Inc., San Jose, CA, USA).

The relative performance of the individual radiation models was also achieved by a combination of both statistical and graphical analyses (Evseev and Kudish, 2009). A number of statistical criteria utilized in evaluation of the radiation models and the related parameters are presented in Table 4.5. For each parameterization, the estimated value is denoted by e_i, the measured value is denoted by m_i while n is the number of observations. In addition to the test criteria, a coefficient of determination (R^2) was very useful in comparing the simulated downwelling and upwelling longwave radiation components with the respective measured values. The lower the values of BIAS, RMSE, MAE and PMRE, and the higher the values of R^2, the better the goodness of fit (Dos Santos et al., 2011).

Table 4.5. Statistical criteria for evaluation of the radiation models.

Description	Symbol	Calculation formula	No.
Bias	BIAS	$\dfrac{1}{n} \cdot \sum\limits_{i=1}^{n} \left(e_i - m_i \right)$	(4.42)
Root mean square error	RMSE	$\sqrt{\dfrac{1}{n} \cdot \sum\limits_{i=1}^{n} \left(e_i - m_i \right)^2}$	(4.43)
Mean absolute error	MAE	$\dfrac{1}{n} \cdot \sum\limits_{i=1}^{n} \left| e_i - m_i \right|$	(4.44)
Percentage mean relative error	PMRE	$\dfrac{y_0}{n} \cdot \sum\limits_{i=1}^{n} \left| \dfrac{e_i - m_i}{m_i} \right|$	(4.45)

(Source: modified after Dos Santos et al., 2011)

where,

n : number of observations   [-]

e_i : estimated value (radiation)   [W m^{-2}]

m_i : measured value (radiation)   [W m^{-2}]

y_0 : coefficient = 100 (Dos Santos et al., 2011)   [%]

4.5 Exterior Surface Energy Balance

The energy balance at the exterior surface of the developed thermal box was necessary in order to establish the net radiation gain (daytime solar gain) or the net radiation loss (due to heating at night). The net radiation R_n is important for surface energy analysis and is generally defined as the difference between incoming and outgoing radiation of both short and long wavelengths (Choi, 2013). This net (all-wave) radiation R_n at the surface can be determined as the algebraic sum of the net shortwave radiation $R_{n,sw}$ and the net longwave radiation $R_{n,lw}$ (Ayoola et al., 2014).

$$R_n = R_{n,sw} + R_{n,lw} \tag{4.46}$$

where,

R_n : net (all-wave) radiation   [W m^{-2}]

$R_{n,sw}$: net shortwave radiation   [W m^{-2}]

$R_{n,lw}$: net longwave radiation   [W m^{-2}]

This net radiation balance R_n considers the total solar irradiance and the reflected component for $R_{n,sw}$, while the downwelling and the upwelling longwave radiation components are used in the calculation of $R_{n,lw}$. Hence, the R_n is further expressed as:

$$R_n = I_{t,t} \cdot \left(1 - \alpha_s\right) + LWR_{d,t} - LWR_{u,t} \tag{4.47}$$

where,

R_n : net radiation   [W m^{-2}]

$I_{t,t}$: total solar radiation on a tilted surface   [W m^{-2}]

α_s : albedo of the earth surface   [-]

$LWR_{d,t}$: total downwelling longwave radiation   [W m^{-2}]

$LWR_{u,t}$: total upwelling longwave radiation   [W m^{-2}]

4.5.1 Heat balance

Considering an exterior surface of the thermal box, the heat balance is expressed as:

$$U \cdot A_s \cdot \Delta T + Q_l = Q_{lir} + Q_{cv} \tag{4.48}$$

where,

U	: heat transfer coefficient of cover material	[W m^{-2} K^{-1}]
A_s	: total surface area	[m^2]
ΔT	: air temperature difference	[K]
Q_l	: heat flux by air exchange through leakage	[W]
Q_{lir}	: heat loss by longwave infrared radiation	[W]
Q_{cv}	: heat loss by convection	[W]

The Q_l in a dry greenhouse can be calculated using the following relation (Tantau, 2013):

$$Q_l = \frac{z}{x_{t,4}} \cdot V_{gi} \cdot \rho_a \cdot C_{pa} \cdot \Delta T \tag{4.49}$$

where,

Q_l	: heat flux by air exchange through leakage	[W]
z	: air exchange rate due to leaks	[h^{-1}]
$x_{t,4}$	: coefficient = 3600 (Tantau, 2013)	[s h^{-1}]
V_{gi}	: inner volume of greenhouse model	[m^3]
ρ_a	: density of air	[kg m^{-3}]
C_{pa}	: specific heat capacity of air	[J kg^{-1} K^{-1}]
ΔT	: air temperature difference	[K]

From the tracer gas measurements, a z value of 1 h^{-1} for the big south-facing thermal box was obtained and together with the thermal properties of air and other parameters, the Q_l can be computed. Due to heating, the exterior surface is radiating energy to its cooler surroundings and the net radiation heat loss rate can be determined.

4.5.2 Significance of radiative heat transfer coefficient in U_{cs}-value

A resistance model (Fig. 4.20) was used as a methodological approach to understand the heat transfer at the cover surface and thus compute the heat transfer coefficients. The resistances are reciprocals of the heat transfer coefficients. The connection of these heat resistors played a key role in accurate determination of the final overall heat transfer coefficient (U_{cs}-value). The U_{cs}-value comprises of the heat transfer coefficient through the cover material U and the heat transfer coefficient due to leakage U_l (Tantau, 2013). The approach was specifically useful in quantifying the heat transfer coefficient due to the longwave radiation and the convection at night based on the total heat consumed while heating the big thermal box system. In particular, this ensured that the contribution of the radiative heat transfer coefficient U_{lir} to U_{cs}-value was distinguished from that due to the convective heat transfer coefficient U_{cv}.
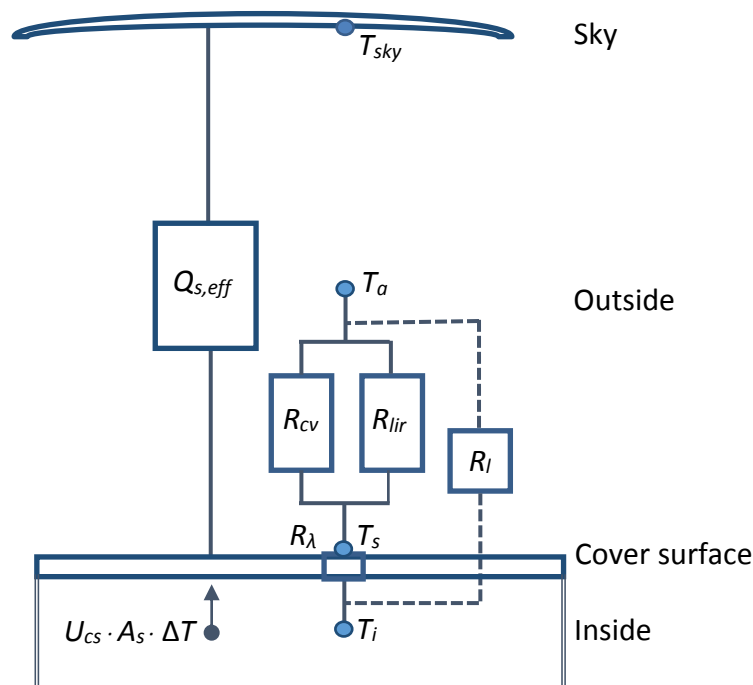
Fig. 4.20. Model of heat resistors and other parameters from inside to the outside air.

where,

U_{cs}	: overall heat transfer coefficient (U_{cs}-value)	[W m^{-2} K^{-1}]
A_s	: total surface area	[m^2]
ΔT	: air temperature difference	[K]
$Q_{s,eff}$	: effective thermal radiation exchange	[W m^{-2}]
R_{cv}	: heat resistance due to convection	[m^2 K W^{-1}]

R_l : heat resistance due to leakage   [m² K W⁻¹]

R_{lir} : heat resistance due to longwave radiation   [m² K W⁻¹]

R_λ : heat resistance due to conduction   [m² K W⁻¹]

T_a : air temperature   [K]

T_i : inside temperature   [K]

T_s : surface temperature   [K]

T_{sky} : sky temperature   [K]

The percentage composition of cover surface (86 % glass and 14 % glazing bars) was used to calculate the effective surface temperature $T_{s,eff}$. Thus, $T_{s,eff}$ is a function of the temperature of the glass surface T_g and the temperature of the glazing bar surface T_{gb}.

$$T_{s,eff} = y_{c,6} \cdot T_g + y_{c,7} \cdot T_{gb} \tag{4.50}$$

where,

$T_{s,eff}$: effective surface temperature   [K]

T_g : temperature of glass surface   [K]

T_{gb} : temperature of glazing bar surface   [K]

$y_{c,6}$: coefficient = 0.86 (fraction of glass)   [-]

$y_{c,7}$: coefficient = 0.14 (fraction of glazing bars)   [-]

Based on the heat balance, the heat transfer coefficient by convection and radiation were computed as (Mammeri et al., 2015; Liu and Harris, 2013):

$$U_{cv} = \frac{Q_{cv}}{A_s \cdot \Delta T_{s-a}} \tag{4.51}$$

$$U_{lir} = \frac{Q_{lir}}{A_s \cdot \Delta T_{s-a}} \tag{4.52}$$

where,

U_{cv} : convective heat transfer coefficient   [W m⁻² K⁻¹]

U_{lir} : radiative heat transfer coefficient   [W m⁻² K⁻¹]

A_s : total surface area   [m²]

Q_{cv} : heat loss by convection   [W]

Q_{lir} : heat loss by longwave infrared radiation   [W]

ΔT_{s-a} : surface-to-air temperature difference   [K]

Due to the linearized radiation exchanges of the surface with the sky, the air and the ground, the U_{lir} can be computed as (EnergyPlus 8.0, 2013; Oliveti et al., 2012):

$$U_{lir} = \varepsilon_s \cdot \sigma \cdot \left(\frac{\varepsilon_{sky} \cdot F_{sky} \cdot \left(T_s^4 - T_{sky}^4\right)}{T_s - T_{sky}} + \frac{\varepsilon_s \cdot F_{air} \cdot \left(T_s^4 - T_a^4\right)}{T_s - T_a} + \frac{\varepsilon_{gnd} \cdot F_{gnd} \cdot \left(T_s^4 - T_{gnd}^4\right)}{T_s - T_{gnd}} \right)$$

(4.53)

where,

U_{lir}	: radiative heat transfer coefficient	[W m^{-2} K^{-1}]
ε_s	: surface emissivity	[-]
ε_{sky}	: sky emissivity	[-]
ε_a	: effective atmospheric emissivity	[-]
ε_{gnd}	: emissivity of surrounding ground objects	[-]
σ	: Stefan-Boltzmann constant = $5.67 \cdot 10^{-8}$	[W m^{-2} K^{-4}]
F_{air}	: view factor to the air	[-]
F_{gnd}	: view factor to the ground	[-]
F_{sky}	: view factor to the sky	[-]
T_a	: air temperature	[K]
T_{gnd}	: ground temperature	[K]
T_s	: surface temperature	[K]
T_{sky}	: sky temperature	[K]

From the literature, the preferred U_{cv} equation covering wind speed in all directions and more specifically for the Venlo greenhouses is given by (Bot, 1983):

$$U_{cv} = x_{u,2} + x_{w,2} \cdot v$$

(4.54)

where,

U_{cv}	: convective heat transfer coefficient	[W m^{-2} K^{-1}]
$x_{u,2}$	: coefficient = 2.8 (Bot, 1983)	[W m^{-2} K^{-1}]
$x_{w,2}$	: coefficient = 1.2 (Bot, 1983)	[W s m^{-3} K^{-1}]
v	: wind speed	[m s^{-1}]

5 RESULTS

5.1 Surface Inclination and Orientation Effects on Thermal Radiation Exchange

5.1.1 Surface inclination

The variation of surface-to-air temperature difference ΔT_{s-a} for both the roof and the wall in the four selected wind speed classes are compared in Fig. 5.1. The box plots in each of the four directions (south, west, north and east) display the variability of ΔT_{s-a} as the wind speed increases. For all the box orientations, ΔT_{s-a} declined with an increase in wind speed. This trend further shows that the wall ΔT_{s-a} was always higher than the roof ΔT_{s-a} and this was apparently not influenced by the directions of the thermal boxes. Further tests through an analysis of variance (ANOVA) confirmed an insignificant effect of the orientation on the ΔT_{s-a} trend ($p > 0.05$).
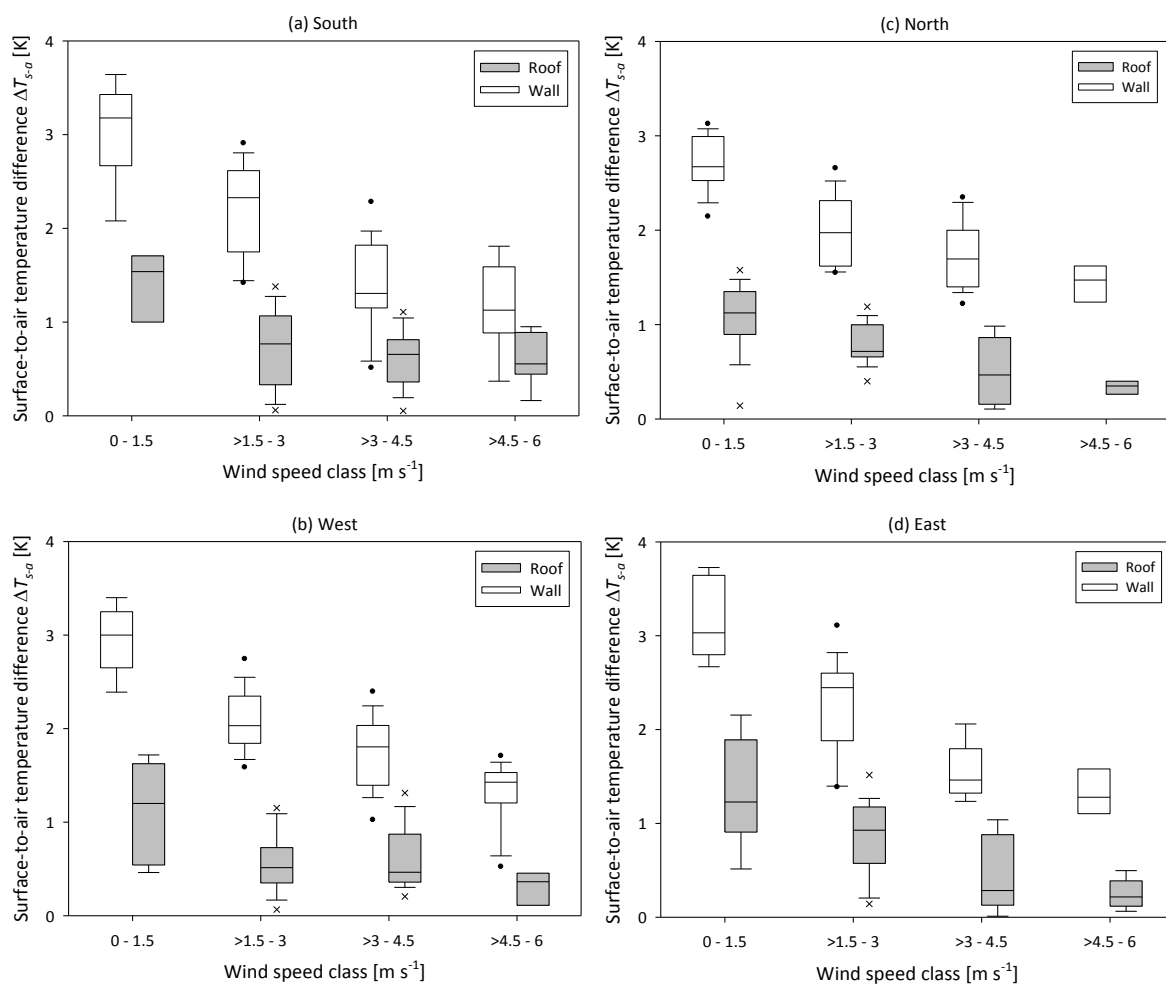

Fig. 5.1. Variation of roof and wall surface-to-air temperature differences with wind speed (n = 41 nights for both 24° (roof) and 90° (wall) surface inclination angles).

With a temperature difference (inside temperature minus outside air temperature) of 8 K, the range of net radiation was less strongly negative, especially under overcast conditions (Fig. 5.2). For both surfaces (roof and wall), the figure compares the mean net radiation R_n with the corresponding wind speeds for both overcast and clear-sky conditions. The overall trends of R_n under overcast conditions (6 to 8 octas) show insignificant differences from each other ($p > 0.05$). However, it can be noticed in both sky conditions that at the wind speed of less than 1.5 m s^{-1}, the mean R_n was more negative compared to the values at higher wind speeds. It can also be seen from the figure that the net radiation loss (negative R_n) values were always lower under the clear-sky condition (0 to 2 octas) than those under the overcast condition. On clear-sky nights, the roof had lower R_n (more negative) values than those of the wall due to the difference in the inclination angle.
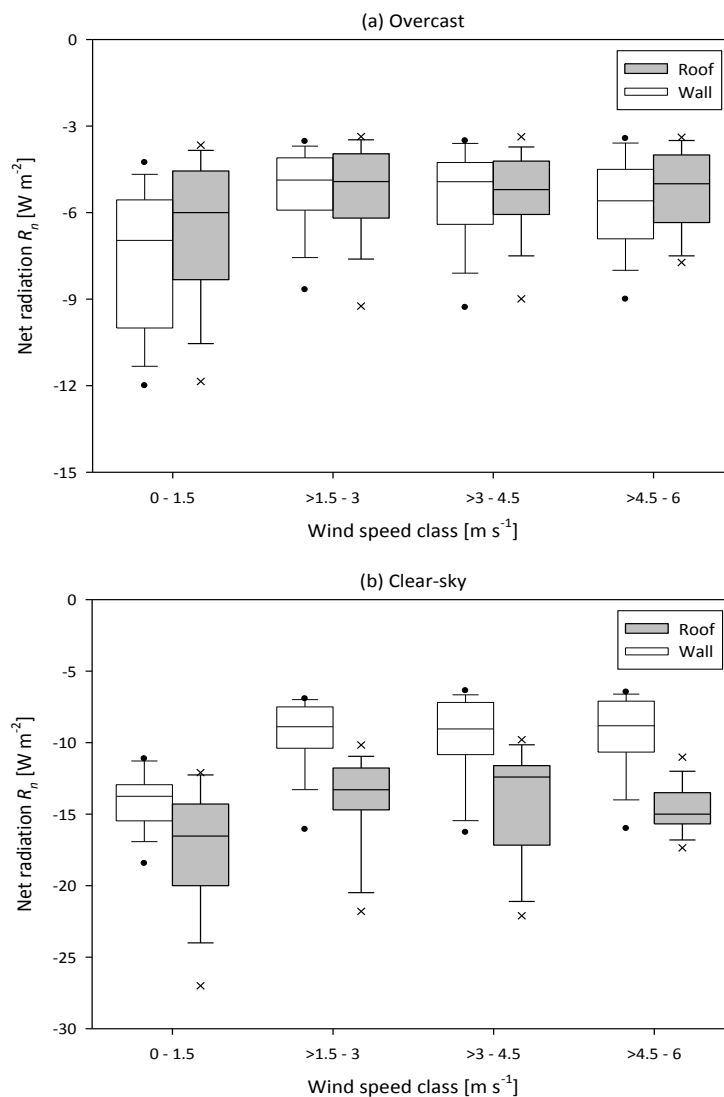
Fig. 5.2. Variation of mean net radiation at the roofs and the walls with wind speed under all-sky conditions: (a) overcast (n = 35 nights), and (b) clear-sky (n = 6 nights).

5.1.2 Surface orientation

During the measurement period, wind was categorized based on the direction from which it originated and its wind speed class. The frequencies of the wind direction and the wind speed are presented in Fig. 5.3. Wind originated mostly from south and west directions (Fig. 5.3(a)), with the former registering a higher dominance (37 %) than the latter (31 %). On the other hand, wind from north and east contributed to only 13 % and 19 %, respectively. In Fig. 5.3(b), the recorded wind speed was mostly (about 55 %) in the range of 1.5 m s^{-1} to < 3 m s^{-1}. This was followed by the range of 3 m s^{-1} to < 4.5 m s^{-1} (about 24 %). Wind speed > 4.5 m s^{-1} was rarely observed during the measurement period (8 %), while that less than 1.5 m s^{-1} accounted for only 13 %.
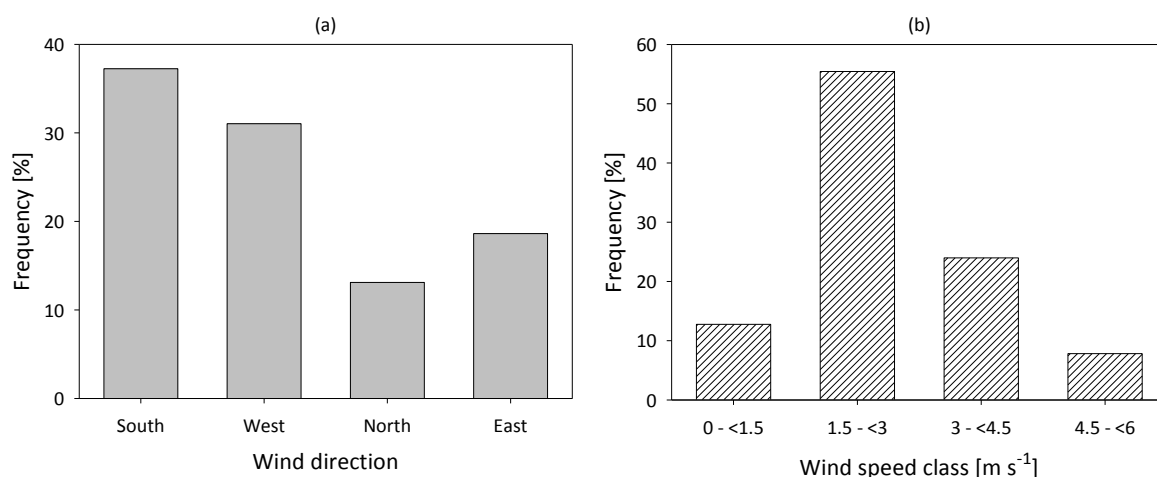

Fig. 5.3. Occurrence of wind direction (a) and wind speed class (b) during the investigation period ((a) n = 54 (south), n = 45 (west), n = 19 (north), n = 27 (east); (b) n = 75 (< 1.5 m s^{-1}), n = 326 (1.5 m s^{-1} to < 3 m s^{-1}), n = 141 (3 m s^{-1} to < 4.5 m s^{-1}), n = 46 (4.5 m s^{-1} to < 6 m s^{-1})).

For the chosen wind speed classes and surface orientations, the deviation between the surface-to-air temperature difference ΔT_{s-a} of the wall and that of the roof was represented by ΔT_{W-R}. The values of ΔT_{W-R} (in K) are given in Table 5.1. The mean ΔT_{W-R} was highest at low wind speed (< 1.5 m s^{-1}) and lowest at high wind speed (> 4.5 m s^{-1}). Interestingly, the standard deviation (Stdev) increased with an increase in wind speed, with the range of 0.12 K to 0.26 K. Despite the random orientation of the thermal boxes, the variation in ΔT_{W-R} within the same wind speed class did not show a significant difference ($p > 0.05$). For wind speeds ≥ 3 m s^{-1}, the south-facing surface registered the lowest values in terms of deviation in ΔT_{s-a} unlike the other three surface orientations.

Table 5.1. ΔT_{W-R} for different orientations and wind speeds.

Surface	Selected wind speed classes [m s^{-1}]			
orientation	0 - 1.5	> 1.5 - 3	> 3 – 4.5	> 4.5 - 6
South	1.60 [a]	1.49 [b]	0.75 [c]	0.58 [e]
West	1.82 [a]	1.53 [b]	1.14 [d]	1.01 [f]
North	1.63 [a]	1.30 [b]	1.22 [d]	1.13 [f]
East	1.83 [a]	1.41 [b]	1.15 [d]	1.09 [f]
Mean ± Stdev	1.72 ± 0.12	1.41 ± 0.15	1.07 ± 0.22	0.95 ± 0.26

(Within column, same letter indicates insignificant differences at 5 % level)

5.2 Modelling of Thermal Radiation Exchange

5.2.1 Night situation

5.2.1.1 Development of longwave radiation models

The parameters involved in the development process of the longwave radiation models (downwelling and upwelling) are summarized in Fig. 5.4. The key parameters included emissivity, view factor, cloudiness and temperature. These parameters are related to the radiative exchange of the surface with the sky, the air and the ground. The resulting models are the total downwelling longwave radiation $LWR_{d,t}$, the effective thermal radiation exchange $Q_{s,eff}$ and the upwelling longwave radiation $LWR_{u,t}$.
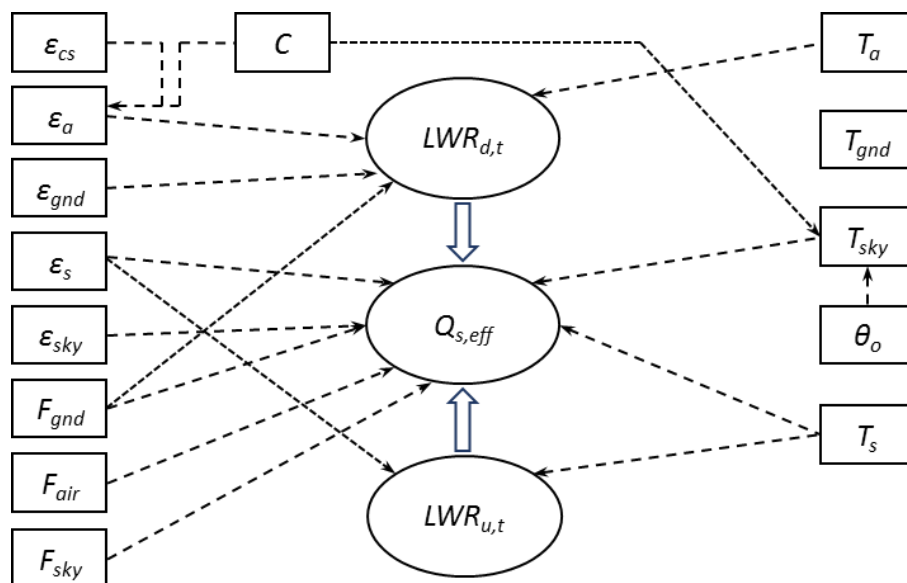

Fig. 5.4. Model development process of the longwave radiation exchange.

where,

ε_{cs}	: clear-sky atmospheric emissivity	[-]
ε_{a}	: effective atmospheric emissivity	[-]
ε_{gnd}	: emissivity of surrounding ground objects	[-]
ε_{s}	: surface emissivity	[-]
ε_{sky}	: sky emissivity	[-]
C	: cloudiness factor	[-]
F_{gnd}	: view factor to the ground	[-]
F_{air}	: view factor to the air	[-]
F_{sky}	: view factor to the sky	[-]
$LWR_{d,t}$	: total downwelling longwave radiation	[W m^{-2}]
$LWR_{u,t}$	: total upwelling longwave radiation	[W m^{-2}]
$Q_{s,eff}$	: effective thermal radiation exchange	[W m^{-2}]
T_{a}	: air temperature	[K]
T_{gnd}	: ground temperature	[K]
T_{sky}	: sky temperature	[K]
θ_{o}	: outside air temperature	[°C]
T_{s}	: surface temperature	[K]

Comparisons of cloudiness predicted using the two approaches (analysed weather maps and octas from the weather watcher) are presented in form of box plots (Fig. 5.5). The comparison was categorized in form of eighths (octas) and thus an opportunity to check the trend of the map-based cloudiness factors. From the figure, under the nighttime situation (Fig. 5.5(a)), the distribution of cloudiness prediction is generally skewed, although a fairly good comparison is noticed between 2 and 4 octas. A quick overview of the plot shows that there was a small range of data for the zero-octa category. In all the categories, outliers were common in the box plots especially between the 4th and 8th categories. This adds to the fact that a statistical significant difference ($p < 0.001$) existed between the two cloudiness prediction approaches. The case is somehow different for the daytime situation (Fig. 5.5(b)). Although the distribution is not shown in as much detail, a skewed distribution during the day was more than at night. The trend shows that the deviation from the reference line (data from the weather watcher) was more than at

night. A small range of data was also pronounced specifically for the first two cloudiness categories (0 and 1 octas). Just like in the nighttime situation, the data were skewed with the outliers being common in almost all the categories. Similarly, further comparison indicates that a statistical significant difference ($p < 0.001$) existed between the two cloudiness prediction approaches (octa- and map-based cloudiness factors) during the day.
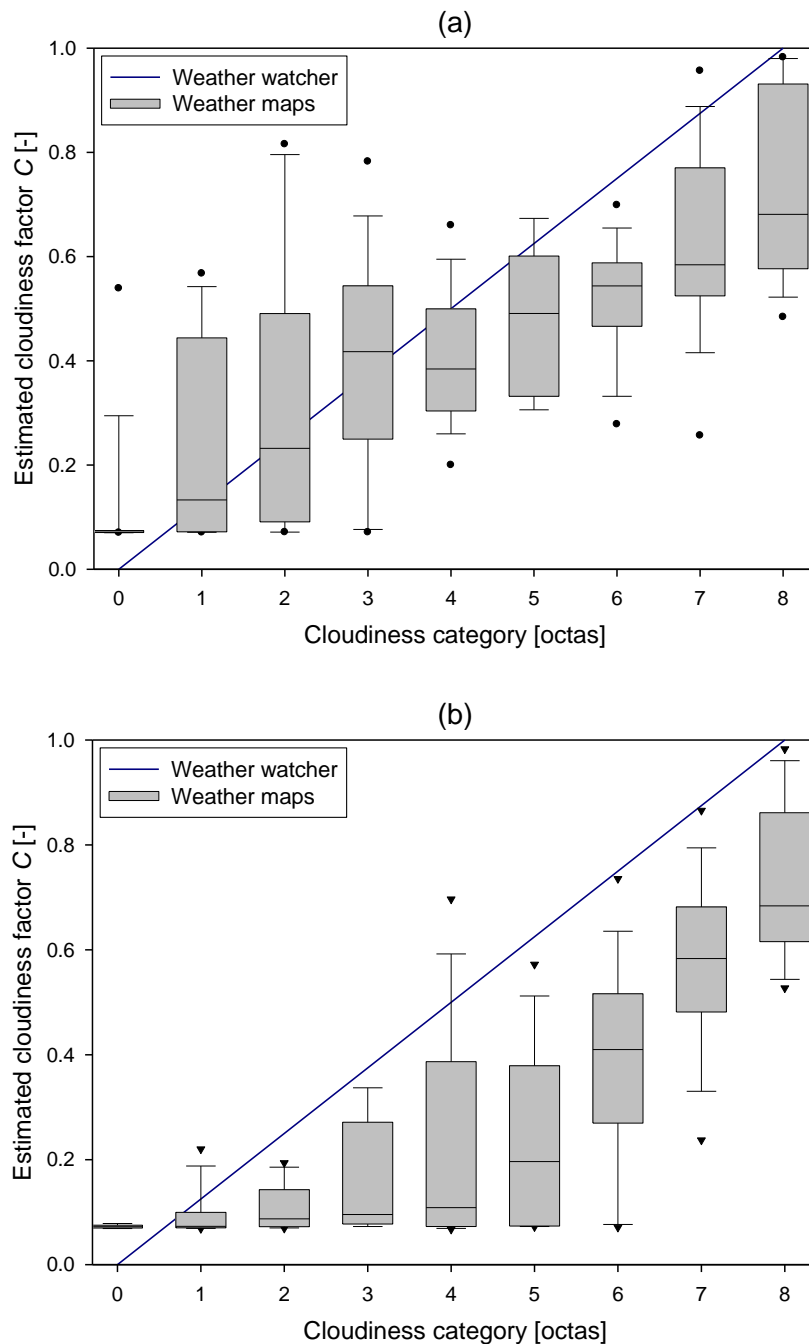

Fig. 5.5. Comparison of cloudiness factors predicted using two approaches: (a) at night (n = 44), and (b) during the day (n = 40).

5.2.1.2 Simulation of longwave radiation

Table 5.2 shows the comparative statistics for the performance of 10 clear-sky atmospheric emissivity calculation models at night compared to the corresponding values computed directly from the measured data. Typical nights with mean cloudiness of less than 1 octa (clear-sky) were used and an hourly average computed for the entire observation period. The performance of the models was ranked in ascending order based on the PMRE values with the best model at the top. The best results, which resulted in the smallest BIAS, RMSE, MAE and PMRE, were obtained by the Sugita and Brutsaert (1993) model. It was followed by the Ido and Jackson (1969) model. The Kruk et al. (2010) model resulted in the highest errors under the nighttime situation.

Table 5.2. Comparative statistics for the performance of clear-sky atmospheric emissivity calculation models during nighttime.

Models	BIAS [-]	RMSE [-]	MAE [-]	PMRE [%]
Sugita and Brutsaert (1993)	0.000	0.011	0.009	1.174
Idso and Jackson (1969)	-0.010	0.014	0.011	1.484
Prata (1996)	-0.010	0.015	0.012	1.648
Dos Santos et al. (2011)	-0.014	0.018	0.016	2.085
Iziomon et al. (2003)	-0.028	0.030	0.028	3.657
Idso (1981)	0.032	0.034	0.032	4.265
Brutsaert (1975)	-0.037	0.039	0.037	4.897
Swinbank (1963)	-0.053	0.054	0.053	7.033
Duarte et al. (2006)	-0.063	0.064	0.063	8.351
Kruk et al. (2010)	-0.083	0.084	0.083	11.067

Comparisons between the simulated downwelling longwave radiation ($LWR_{d,t}$) and upwelling longwave radiation ($LWR_{u,t}$) and their corresponding measured longwave radiation fluxes at night are presented in Fig. 5.6. The $LWR_{d,t}$ and $LWR_{u,t}$ values varied in the range of about 255 W m^{-2} to 400 W m^{-2} and 300 W m^{-2} to 430 W m^{-2}, respectively. Heating of the measurement system at night increased the surface temperatures, thereby increasing the total upwelling longwave radiation $LWR_{u,t}$. Due to the two approaches

utilized for cloudiness prediction (the octas assigned by the weather watcher and the analysed weather maps), simulation was always in two datasets. For both $LWR_{d,t}$ and $LWR_{u,t}$, it is noted that better model prediction was obtained for the nighttime observation period. The map-based simulated data seem to be closer to the 1:1 line than those simulated with octas.
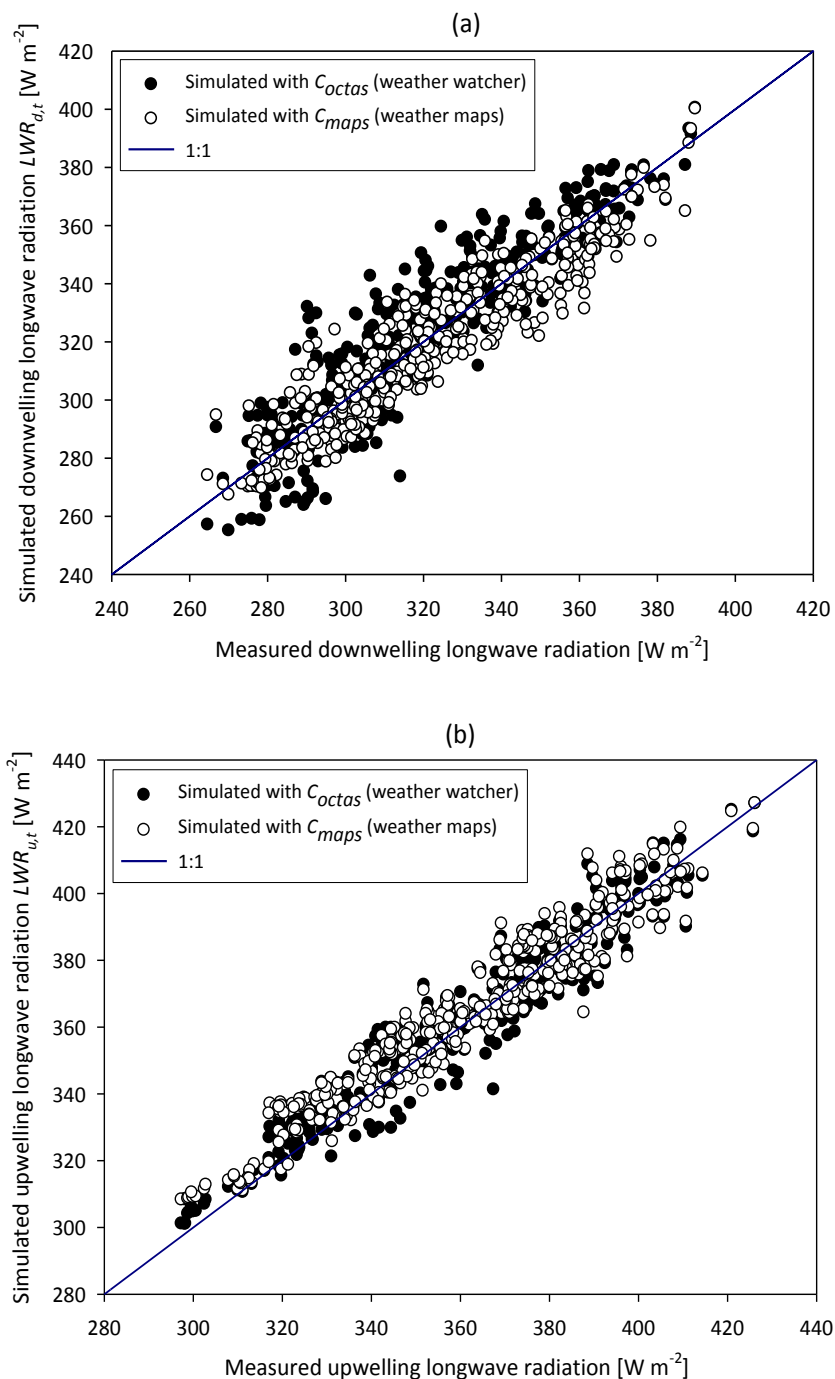

Fig. 5.6. Comparison of simulated and measured nighttime longwave radiation: (a) downwelling (n = 455), and (b) upwelling (n = 455).

5.2.2 Day situation

5.2.2.1 Modification of thermal radiation models

The daytime simulation requires both the shortwave (solar) and the longwave radiation models. A similar approach (as in section 5.2.1) was thus useful to compute the daytime downwelling and the upwelling longwave radiation components. The steps involved in the model modification of the total solar irradiance on the tilted surface are shown in Fig. 5.7. Once the beam and the diffuse components of total solar radiation incident on a horizontal surface are determined (see equations in sub-sections 2.4.3 and 4.4.2), they can be transposed over any given tilted surface (El-Sebaii et al., 2010). The data generated from the measurement system were beneficial in validation of the simulation models.
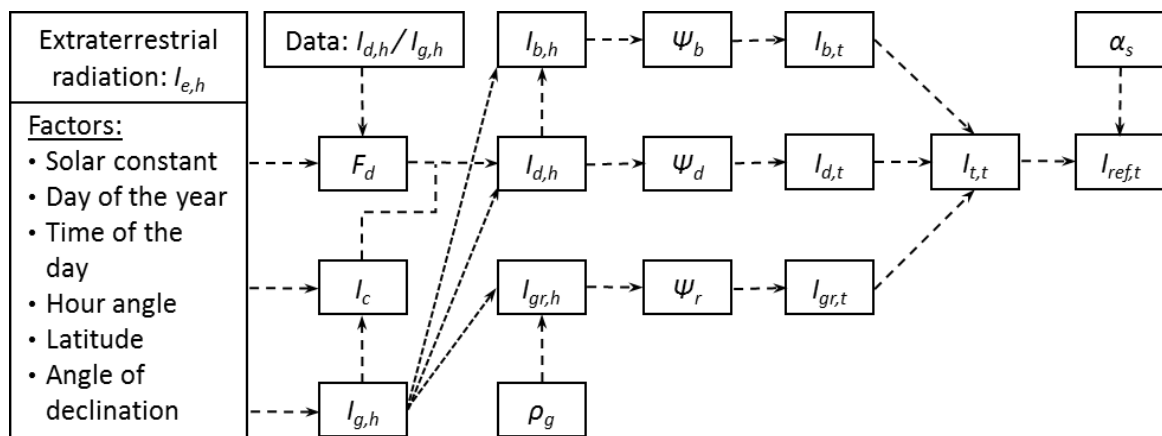
Fig. 5.7. Stepwise modelling of solar radiation components at the tilted surface.

where,

$I_{e,h}$: extraterrestrial radiation on a horizontal surface   [W m^{-2}]

F_d : diffuse fraction   [-]

I_c : clearness index   [-]

$I_{g,h}$: global radiation on a horizontal surface   [W m^{-2}]

$I_{b,h}$: beam radiation on a horizontal surface   [W m^{-2}]

$I_{d,h}$: diffuse radiation on a horizontal surface   [W m^{-2}]

$I_{gr,h}$: ground reflected radiation on a horizontal surface   [W m^{-2}]

ρ_g : ground reflectivity   [-]

Ψ_b : beam radiation conversion factor   [-]

Ψ_d : diffuse radiation conversion factor   [-]

Ψ_r : ground reflected radiation conversion factor   [-]

$I_{b,t}$	: beam radiation on a tilted surface	[W m^{-2}]
$I_{d,t}$	: diffuse radiation on a tilted surface	[W m^{-2}]
$I_{gr,t}$	: ground reflected radiation to a tilted surface	[W m^{-2}]
$I_{t,t}$	: total solar radiation on a tilted surface	[W m^{-2}]
α_s	: albedo of the earth surface	[-]
$I_{ref,t}$	: reflected radiation from a tilted surface	[W m^{-2}]

A comparison of measured solar radiation incident on the tilted glass-covered surface, horizontal global radiation on the horizontal plane and the diffuse solar flux from the sky is presented in Fig. 5.8. The intensity of measured solar radiation appears to increase with the change of season (from winter to early spring). As seen in the figure, the total irradiance on the south-facing tilted surface $I_{t,t}$ was always higher than the horizontal global radiation $I_{g,h}$. The magnitude of $I_{t,t}$ was appreciably increased whenever the difference between the global and diffuse radiations (presence of beam radiation) was large. The diffuse horizontal solar radiation $I_{d,h}$ was notably close to the $I_{g,h}$ values, especially after the 150th hour number.
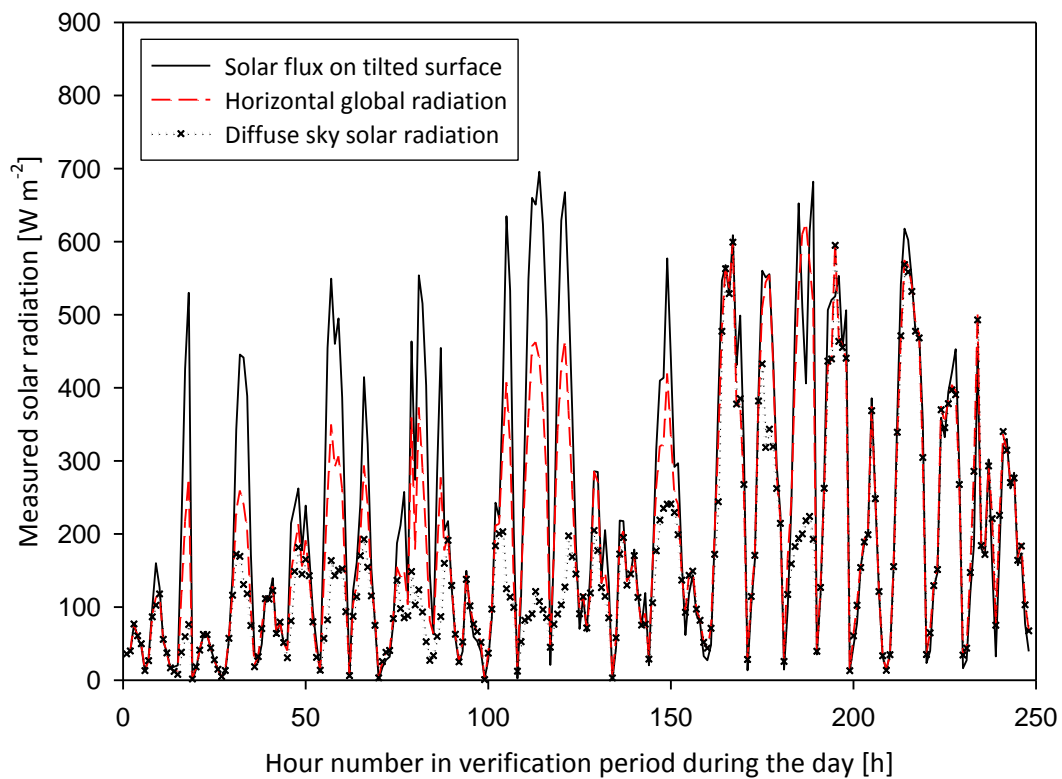

Fig. 5.8. Variation of measured solar radiation incident on horizontal and tilted surfaces

(n = 248).

5.2.2.2 Simulation of thermal radiation

A comparison between the solar radiation measured by the pyranometers of the CNR 4 net radiometer and the simulated values is presented in Fig. 5.9. The total solar irradiance on the south-facing surface inclined at 26.5° included both the direct and the diffuse solar radiation components. The simulation models with the appropriate radiation conversion factors gave promising results, especially within the solar radiation range of 0 W m^{-2} to 500 W m^{-2}. The solar radiation of high magnitude occurred towards the end of the measurement period, i.e. at the early spring period. As seen from the figure, the reflected solar radiation during the entire period was less than 155 W m^{-2}.
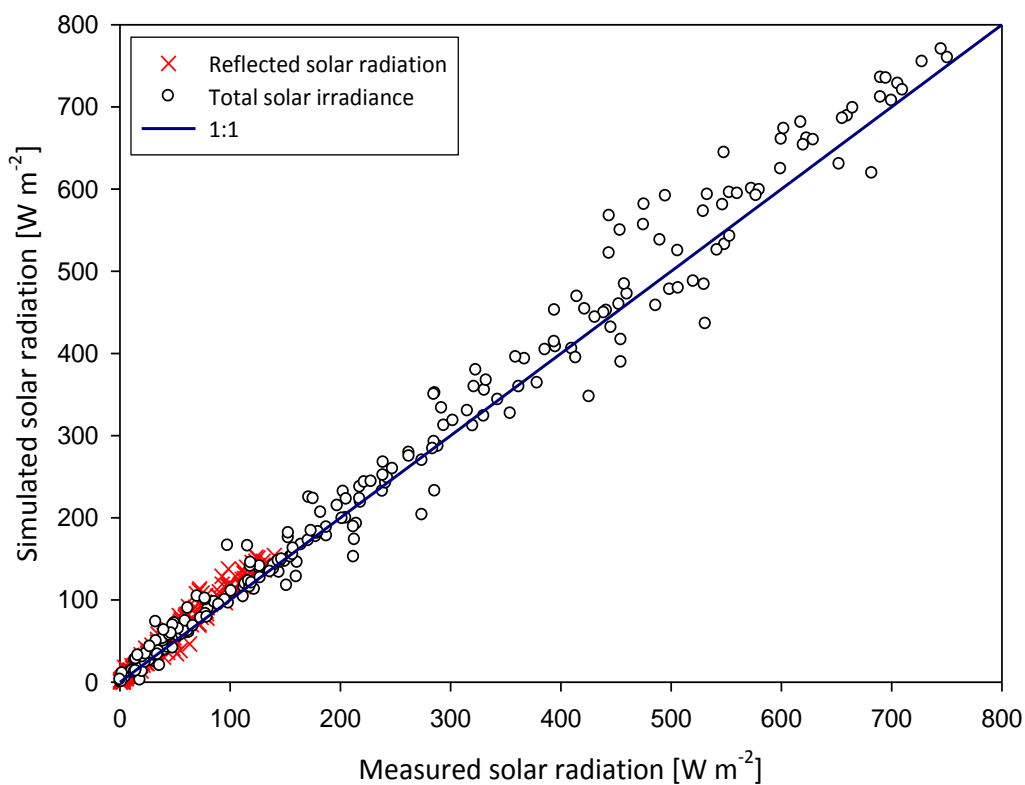
Fig. 5.9. Comparison of the simulated and the measured solar radiation components
(n = 227).

Just like in the nighttime situation, the clear-sky atmospheric emissivity ε_{cs} was useful for modelling of the daytime longwave radiation. The comparative statistics for the performance of the 10 ε_{cs} models during the day are presented in Table 5.3. The estimated values were compared with the corresponding values at less than 1 octa from the dataset. The performance of the models was ranked in ascending order based on the

PMRE values with the best model at the top. As was the case at night, the results with the smallest BIAS, RMSE, MAE and PMRE were similarly presented by the Sugita and Brutsaert (1993) model. The Kruk et al. (2010) was the least performing model (highest errors) also during the day.

Table 5.3. Comparative statistics for the performance of clear-sky atmospheric emissivity calculation models during daytime.

Models	BIAS [-]	RMSE [-]	MAE [-]	PMRE [%]
Sugita and Brutsaert (1993)	-0.001	0.033	0.028	3.597
Dos Santos et al. (2011)	-0.013	0.036	0.028	3.662
Prata (1996)	-0.01	0.035	0.028	3.697
Swinbank (1963)	-0.005	0.034	0.03	3.872
Idso and Jackson (1969)	0.003	0.033	0.03	3.946
Iziomon et al. (2003)	-0.028	0.043	0.034	4.301
Brutsaert (1975)	-0.031	0.046	0.037	4.679
Idso (1981)	0.021	0.04	0.036	4.787
Duarte et al. (2006)	-0.059	0.068	0.059	7.599
Kruk et al. (2010)	-0.073	0.081	0.073	9.503

The simulated downwelling longwave radiation $LWR_{d,t}$ and upwelling longwave radiation $LWR_{u,t}$ and the corresponding measured values during the day are compared in Fig. 5.10. Generally, $LWR_{d,t}$ ranged between 260 W m^{-2} and 430 W m^{-2} while $LWR_{u,t}$ values were in the range of 280 W m^{-2} to 490 W m^{-2}. Despite no heating of the thermal box during daytime, the $LWR_{u,t}$ values were equally high due to solar radiation presence. It is also evident from the figure that simulation with the cloudiness factor derived from octas (assigned by the weather watcher) led to overestimation of $LWR_{d,t}$ during the day. The octa-based $LWR_{d,t}$ values deviated more from the 1:1 line than the map-based ones. However, simulation of $LWR_{u,t}$ with both cloudiness approaches were not significantly different from each other.
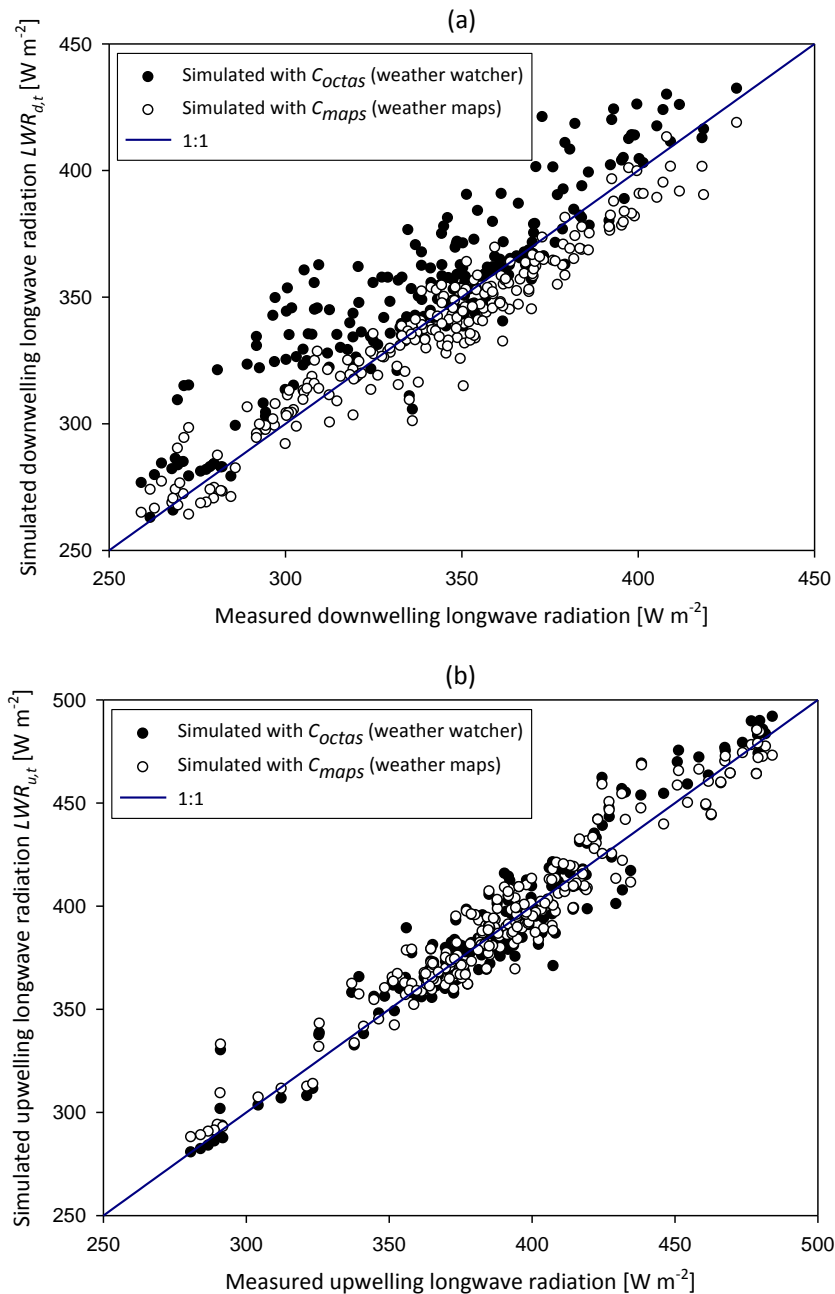
Fig. 5.10. Comparison of simulated and measured daytime longwave radiation:

(a) downwelling (n = 229), and (b) upwelling (n = 229).

5.2.3 Net radiation balance

5.2.3.1 Measurement of net radiation

The variation of average nighttime net radiation R_n at the exterior glass-covered surface is presented in Fig. 5.11. For the study period, the R_n values ranged between -64.8 W m^{-2} and 25.9 W m^{-2}. During mid-winter season, the negative R_n values are typical of the radiation loss from the cover surfaces and at a later stage of the measurement period, R_n

tends towards zero and even positive values. The figure also presents the wind speed values during the investigation period. The wind speed ranged from 0.1 m s^{-1} to 6.1 m s^{-1}, with mean value being 1.2 m s^{-1}. In comparison of both trends, the results show that the low wind speed seems to favour more negative R_n values (increased net radiation loss) while high wind speeds resulted in less negative R_n values (reduced net radiation loss). However, it is apparent from the trends that wind speed does not solely affect R_n at the cover surface.
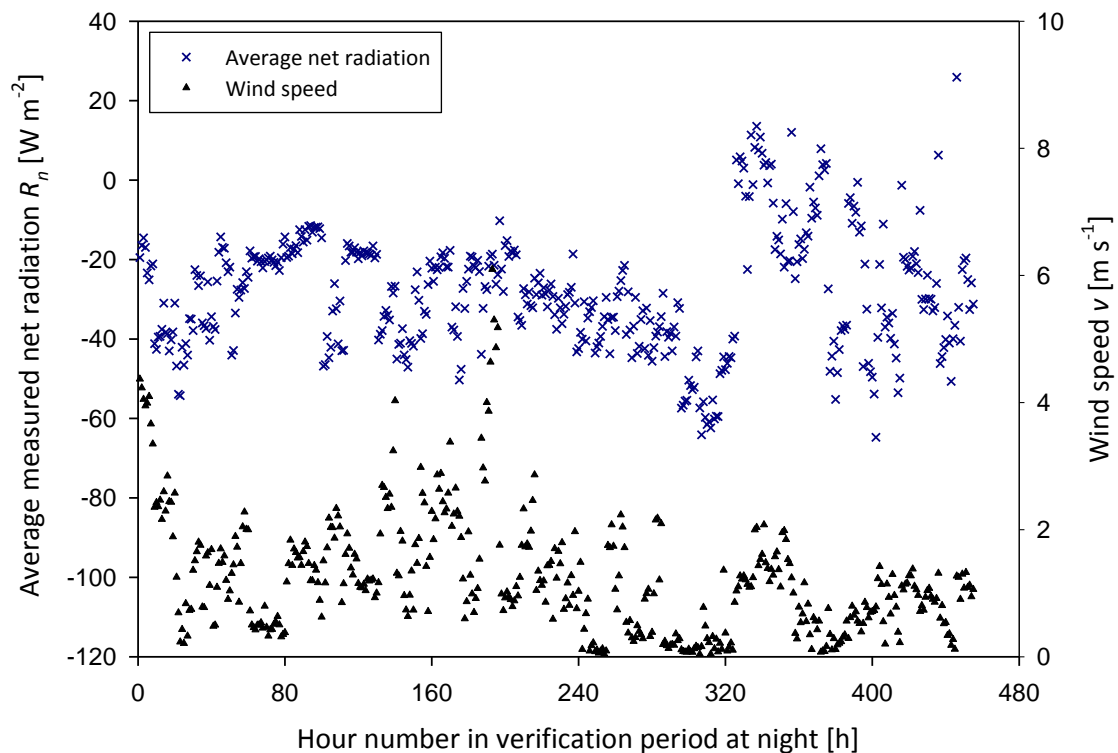
Fig. 5.11. Variation of average net radiation and wind speed at night ($n = 455$).

The nighttime air and surface temperatures during the measurement period are plotted in Fig. 5.12. Due to heating, the exterior effective surface temperature (for both glass and glazing bars) $T_{s,eff}$ was always higher than the air temperature T_a. This was also the case since the temperature inside the box T_i was regulated such that it was 15 K higher than the air temperature T_a. This dependency of temperatures was generally evident throughout the winter and early spring periods within the investigation period. Also presented in the figure is the rainfall amount, which was actually less prevailing during this verification period. It is, however, noticed that whenever it rained, both the $T_{s,eff}$ and the T_a values were close to each other.
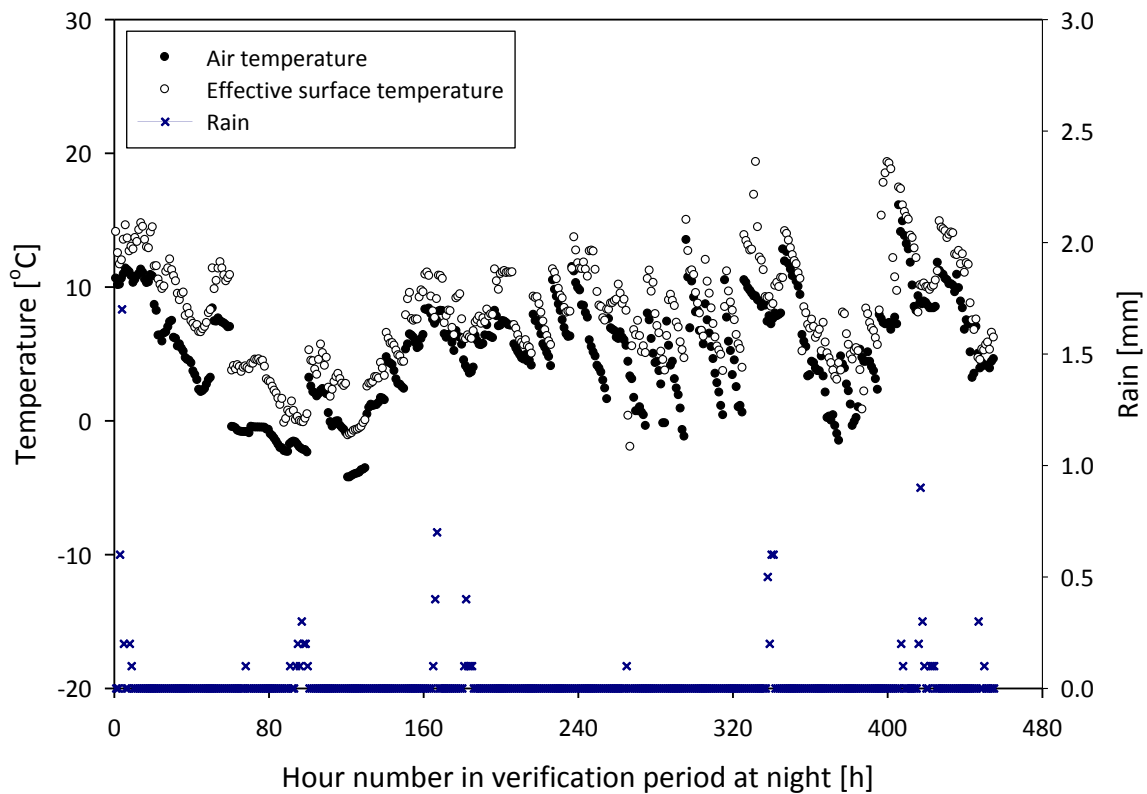
Fig. 5.12. Comparison of air temperature, effective surface temperature and rain with time at night (n = 455).

The average values of daytime net radiation R_n at the exterior cover surface measured with five net radiometers are presented in Fig. 5.13. The R_n values generally ranged between -26.2 W m^{-2} and 589 W m^{-2}. Unlike nighttime situation, solar radiation during the day increased the R_n and this was dependent on the intensity of solar radiation. Also presented in the figure is the trend of the hourly mean wind speed during the same investigation period. The wind speed ranged from about 0.1 m s^{-1} to 6.7 m s^{-1}. The mean value of wind speed during the measurement period was less than 2 m s^{-1}, its value being 1.8 m s^{-1}. On some instances, a decrease in the wind speed appears to favour high R_n (positive values due to solar energy gain) and vice versa. From the figure, however, it is not clear how the wind speed is related to the R_n and this could be an indication that other atmospheric parameters are affected.
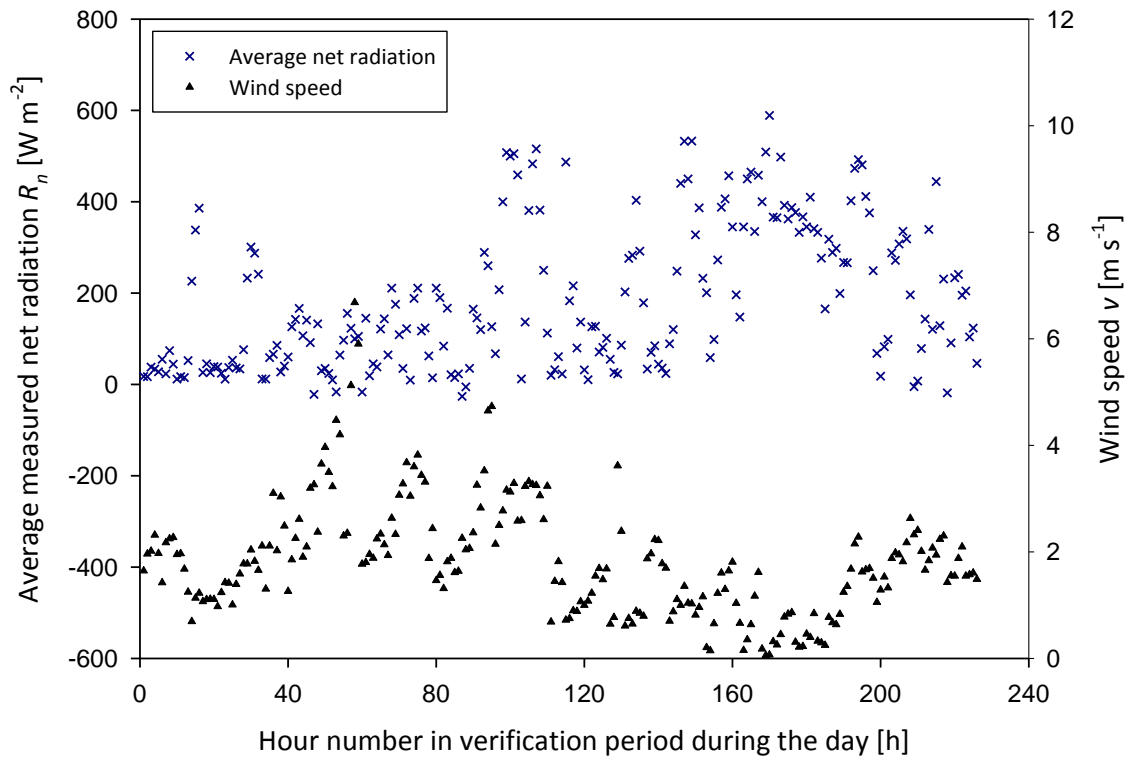
Fig. 5.13. Variation of average net radiation and wind speed with time during the day

(n = 226).

Both the air and effective surface temperatures during the selected daytime investigation period are given in Fig. 5.14. Unlike the nighttime situation, the measurement system was not heated during the day. The difference in the temperatures relied solely on the solar radiation effect on the surface. As expected, the effective surface temperature $T_{s,eff}$ was generally higher than the air temperature T_a. Additionally, the figure includes a plot of rain recorded during the same period. Although the mean rainfall amount was approximately 0 mm, it is noticed from the figure that $T_{s,eff}$ and T_a were close to each other whenever it rained. However, in most cases, the differences between $T_{s,eff}$ and T_a remained considerably large especially at high T_a values.
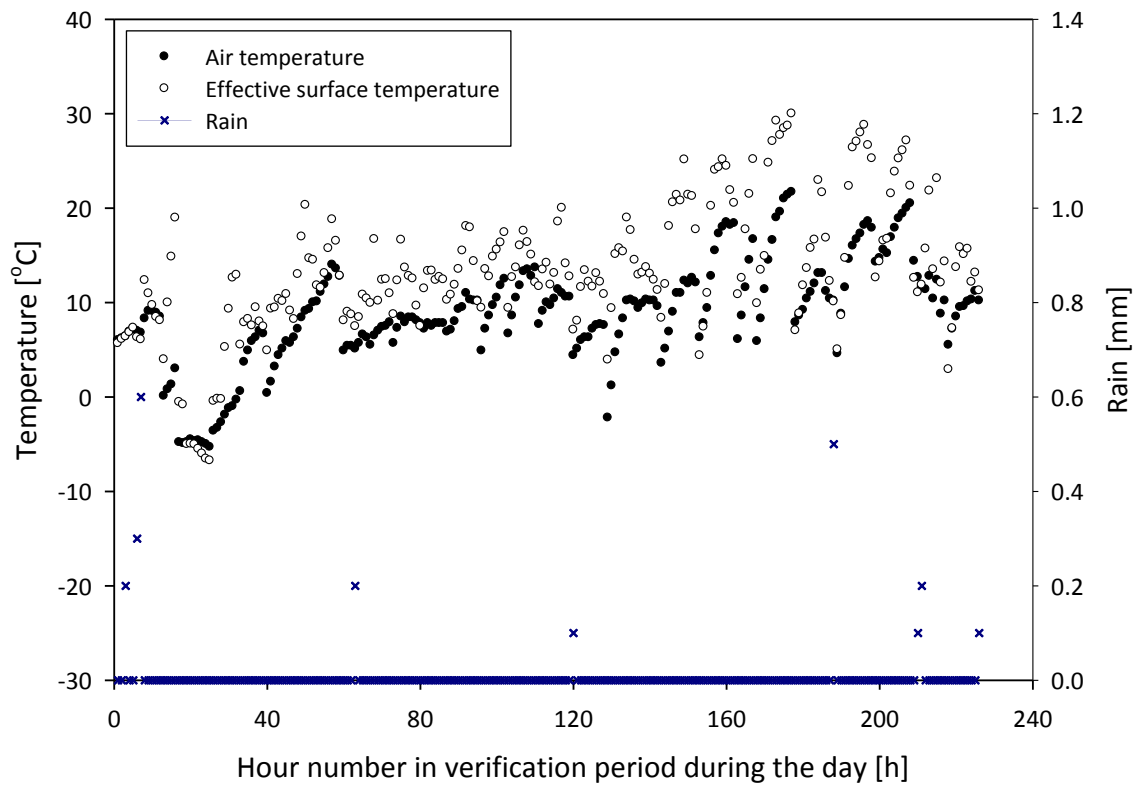
Fig. 5.14. Comparison of air temperature, effective surface temperature and rain with time during the day (n = 226).

5.2.3.2 Simulation of net radiation

The comparisons of the simulated net radiation and the average net radiation are presented in Fig. 5.15. At night (Fig. 5.15(a)), the uneven distribution of supplied heat inside the measurement system led to the scattered variation between the simulated and the measured net radiation loss (negative net radiation). As a result, slight differences in surface temperatures were noticed both for the glass and the glazing bars. However, a fairly good agreement between the simulated and the measured net radiation was attained during the day where solar radiation is prevalent (Fig. 5.15(b)). Under the daytime situation, since the net radiation R_n has mostly positive values (solar gain), the simulated and measured values of R_n were used. The net radiation loss ($LWR_{u,t}$ - $LWR_{d,t}$) values at night were less than 80 W m^{-2} while the daytime R_n ranged between -55 W m^{-2} and 569 W m^{-2}.
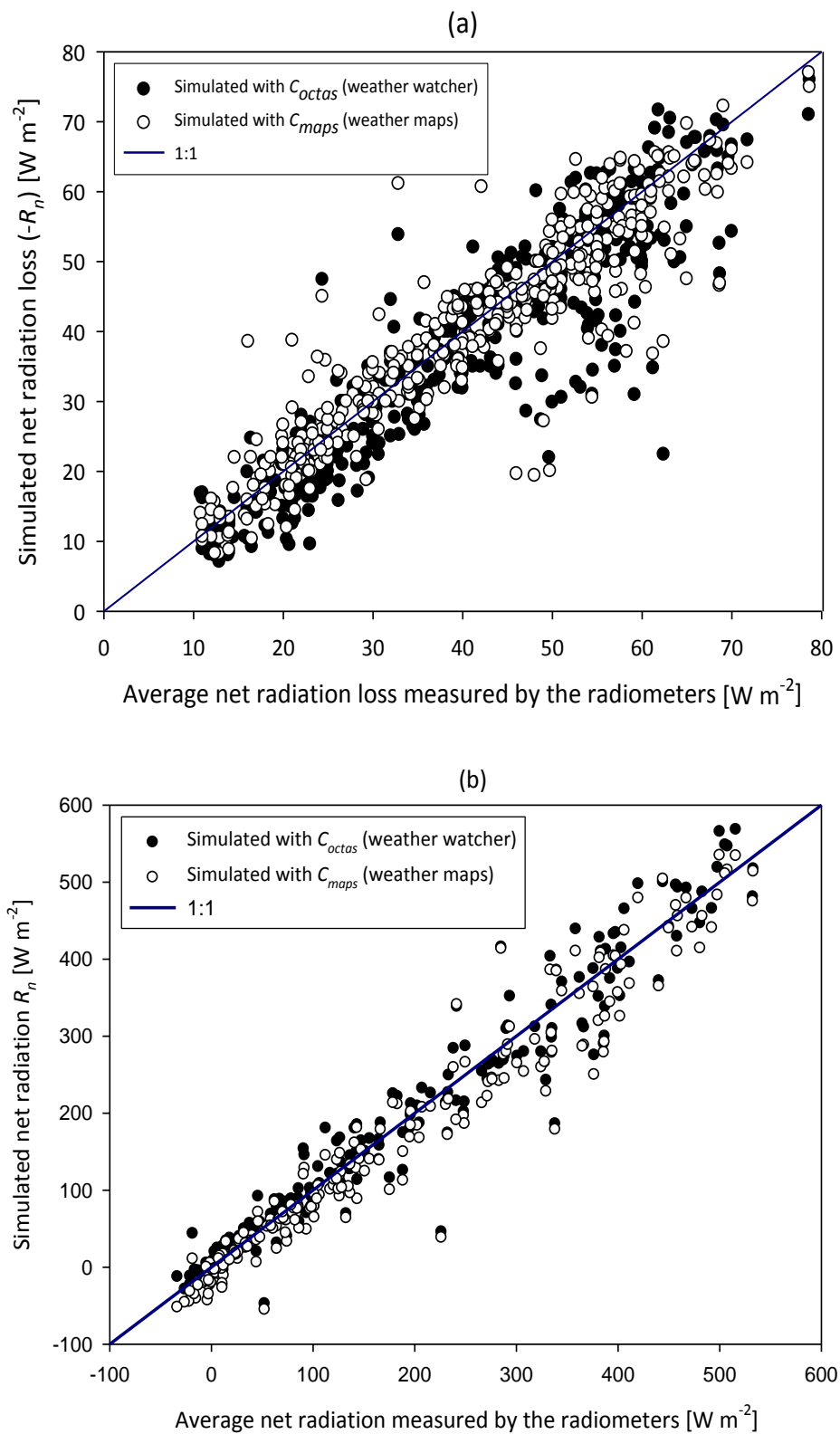
Fig. 5.15. Comparison of simulated and average measured net radiation: (a) at night (n = 455), and (b) during the day (n = 229).

5.2.4 Evaluation and sensitivity analysis of longwave radiation models

5.2.4.1 Evaluation of the models

The evaluation of the longwave radiation models was essential using the previously described statistical criteria (BIAS, RMSE, MAE and PMRE) and the coefficient of determination (R^2). Under both daytime and nighttime situations, the evaluation applied for both the total downwelling longwave radiation $LWR_{d,t}$ and the total upwelling longwave radiation $LWR_{u,t}$. Table 5.4 shows the comparison of nighttime and daytime comparative statistics for the performance of the longwave radiation models. For both the $LWR_{d,t}$ and the $LWR_{u,t}$ models, the simulation was done with the two cloudiness prediction approaches (octa-based and map-based). The simulation results were compared with the measurements for the same period. Although the simulations using both cloudiness prediction techniques were not significantly different ($p > 0.05$), the map-based prediction approach gave the best results with the highest R^2 and the lowest errors (BIAS, RMSE, MAE and PMRE). Both at night and during the day, the test criteria led to somehow better results for the $LWR_{u,t}$ model than for the $LWR_{d,t}$ model.

Table 5.4. Comparative statistics for the performance of longwave radiation models under both night and day situations.

Model*	Nighttime measurements					Daytime measurements				
	BIAS [W m^{-2}]	RMSE [W m^{-2}]	MAE [W m^{-2}]	PMRE [%]	R^2 [-]	BIAS [W m^{-2}]	RMSE [W m^{-2}]	MAE [W m^{-2}]	PMRE [%]	R^2 [-]
[1] $LWR_{d,t}$	2.362	11.011	8.296	2.632	0.870	11.801	19.765	14.766	4.536	0.818
[2] $LWR_{d,t}$	-3.810	9.188	7.353	2.284	0.910	-4.477	11.322	9.022	2.643	0.929
[1] $LWR_{u,t}$	0.266	8.017	6.246	1.730	0.912	1.761	11.449	8.713	2.231	0.924
[2] $LWR_{u,t}$	2.153	7.843	6.411	1.796	0.924	1.523	10.199	7.751	2.004	0.935

*Simulated with cloudiness factors: [1] C_{octas} (weather watcher), [2] C_{maps} (weather maps).

5.2.4.2 Sensitivity analysis of the models

Based on the variation of the key parameters from the base value (median), temperature clearly stands out to be the critical parameter influencing the longwave radiation models (Fig. 5.16). Considering air temperature T_a change of 45 K, the increment in $LWR_{d,t}$ was as high as 115.35 % (Fig. 5.16(a)). The $LWR_{d,t}$ fluxes increased by about 22.61 % under cloudy

conditions (cloudiness factor $C = 1$) while for 60 % change in relative humidity RH, the increment in $LWR_{d,t}$ was only 10.97 %. Clouds seemed to be somewhat more sensitive in the $Q_{s,eff}$ model (Fig. 5.16(b)) than in the $LWR_{d,t}$ model. Generally the surface-to-air temperature difference and the air temperature were the most sensitive parameters.
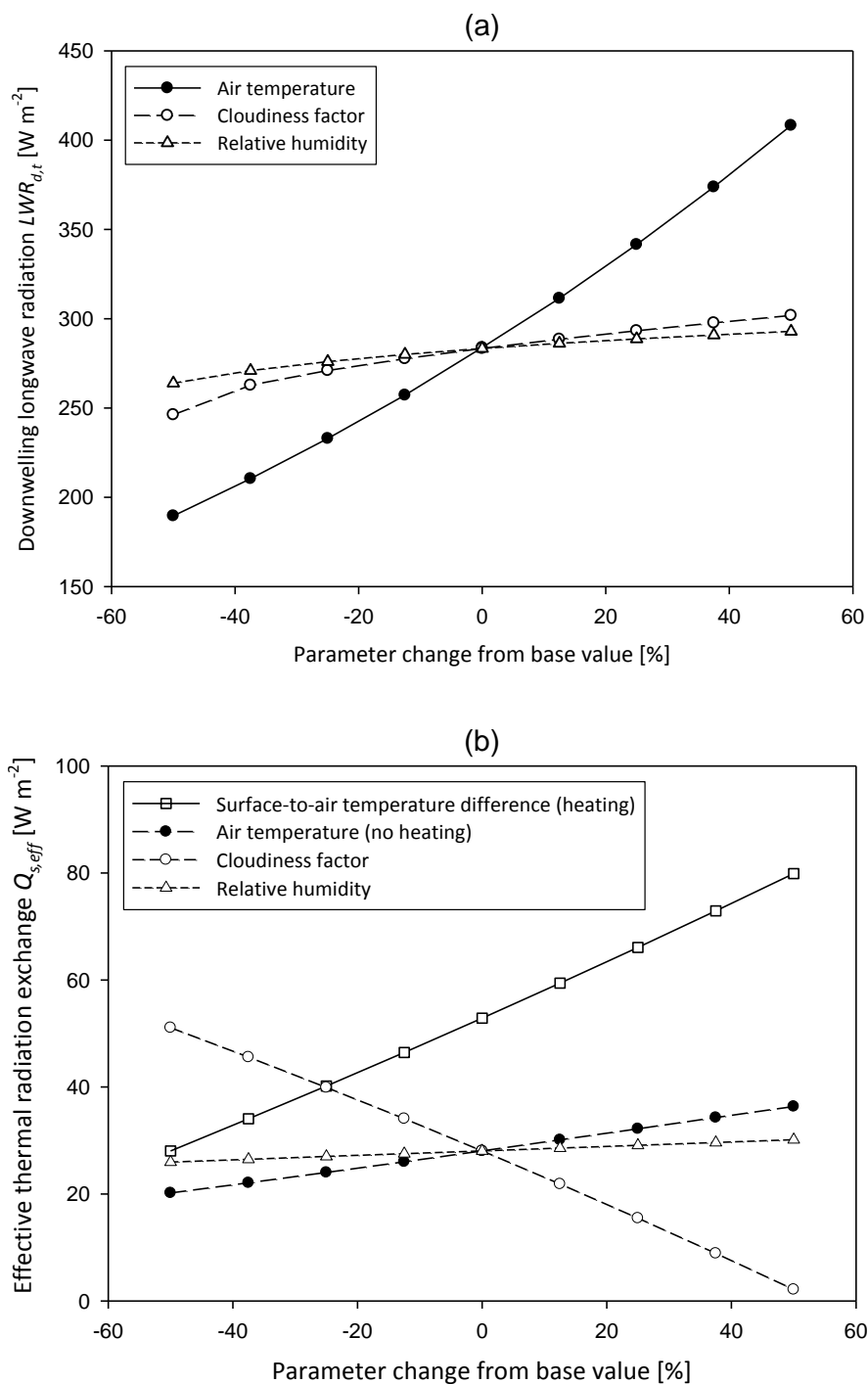

Fig. 5.16. Sensitivity of longwave radiation models to changes in the key parameters: (a) downwelling longwave radiation, and (b) effective thermal radiation exchange (n = 9).

5.2.4.3 Sensitivity index

The sensitivity indices obtained from sensitivity analysis of longwave radiation models are presented in Table 5.5. For the $LWR_{d,t}$ model, the highest sensitivity index SI was due to changes in air temperature. Changes in both cloudiness and relative humidity resulted in low SI values, with the latter registering the lowest. Similar results were noted for the case of effective thermal radiation exchange $Q_{s,eff}$ model. The highly sensitive parameter still stands out to be the temperature. However, the higher SI was as a result of increment in temperature difference between the surface and the air. The sensitivity indices due to changes in cloudiness and relative humidity in the $Q_{s,eff}$ model were high and medium, respectively.

Table 5.5. Sensitivity indices of longwave radiation models due to the parameter changes.

	Key parameters influencing the radiation models			
	Air temperature	Cloudiness factor	Relative humidity	Temperature difference
Model output variable	T_a [K]	C [-]	RH [%]	$\Delta T_{s\text{-}a}$ [K]
Downwelling longwave radiation $LWR_{d,t}$ [W m^{-2}]	5.24	0.08	0.07	-
Effective thermal radiation exchange $Q_{s,eff}$ [W m^{-2}]	10.20 [a]	0.87	0.11	17.22 [b]

([a] with no heating; [b] with heating)

5.3 External Surface Radiation Distribution and Heat Balance

5.3.1 Thermographic assessment of the surface

The thermal status in terms of surface temperature and heat distribution at the glass-covered surface was assessed using infrared thermography. The measured upwelling longwave radiation is compared with the surface radiation flux evaluated by the thermography method as shown in Fig. 5.17. It is clearly seen that the measured values were always greater than those obtained through thermography. At around the 30th hour number, the measured and computed (thermography) were fairly the same and it was on this day (3rd March 2013) that the mean cloudiness factor was zero octa (eighth). In the

same figure, a clear and marked relationship between the radiation emitted from the exterior surface and the temperature is also observed. During the verification period, the air and exterior surface temperature profiles vary in a similar way as the surface radiation. Due to nighttime heating of the developed measurement system, the effective surface temperature $T_{s,eff}$ was always higher than the air temperature T_a. Accurate knowledge of surface emissivity ε_s (0.92 for glass and 0.96 for steel glazing bars) leads to minimal errors related to apparent temperature recorded by the thermal camera.
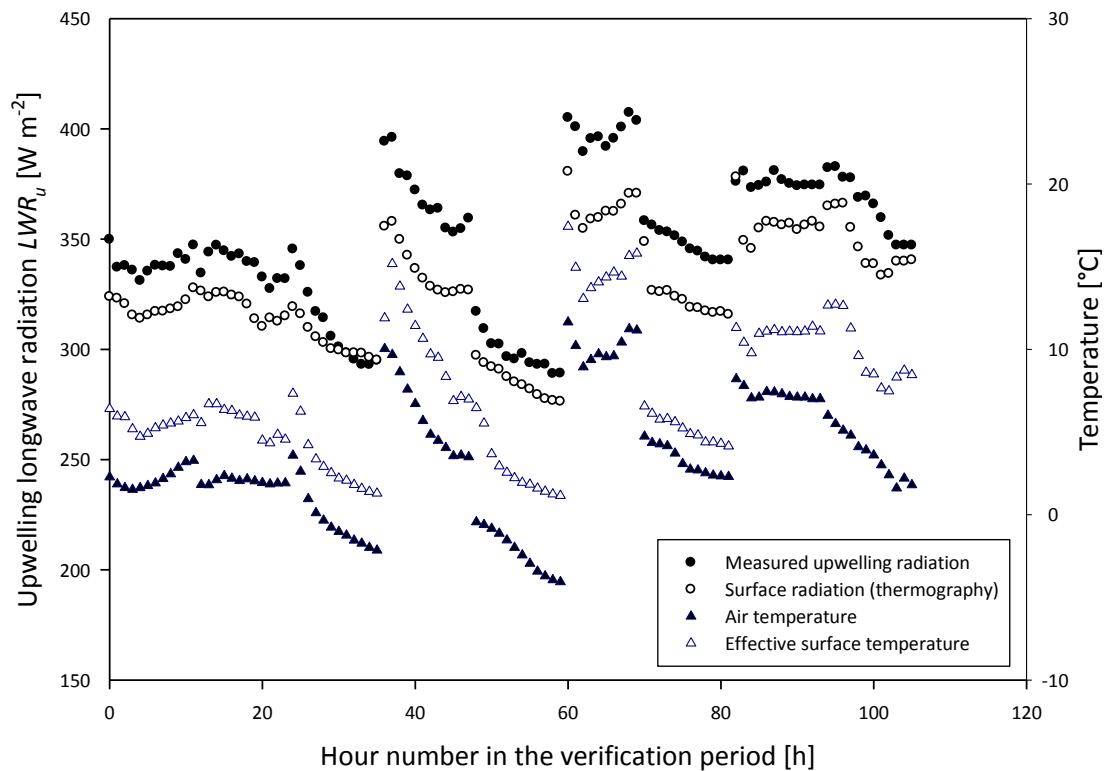
Fig. 5.17. Variation of exterior surface heat flux with the air and surface temperatures ($n = 105$).

Two thermograms obtained from the analysed weather images on two typical nighttime measurements are given in Fig. 5.18. The fairly large range in temperatures is due to the fact the thermal images also captured the temperatures of the radiometers and the supporting frames (blue and green colours) above the cover surface. One of the nights had presence of little showers (about 0.2 mm) while the other had no rain at all. The heating rods placed on the lower edges inside the boxes are captured by the infrared thermal camera and this is shown by vertical pink lines on the thermograms.
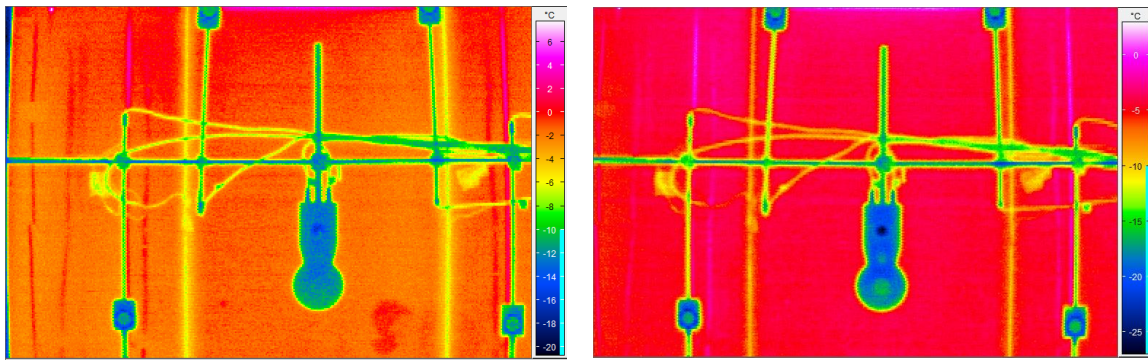
Fig. 5.18. Thermograms of the surface with little showers (left) and with no rain (right).

Since the big south-facing thermal box was inclined at 26.5° from the horizontal, the upper section of the glass-covered surface was always slightly warmer than the lower section (Fig. 5.19). Although this was the case, the variation in the apparent surface temperature $\theta_{s,app}$ was not significant ($p > 0.05$). However, the scenario in Fig. 5.19(c) was characterized by a clear-sky condition and the $\theta_{s,app}$ values at the upper section were somehow significantly different from those on the lower section ($p < 0.05$).
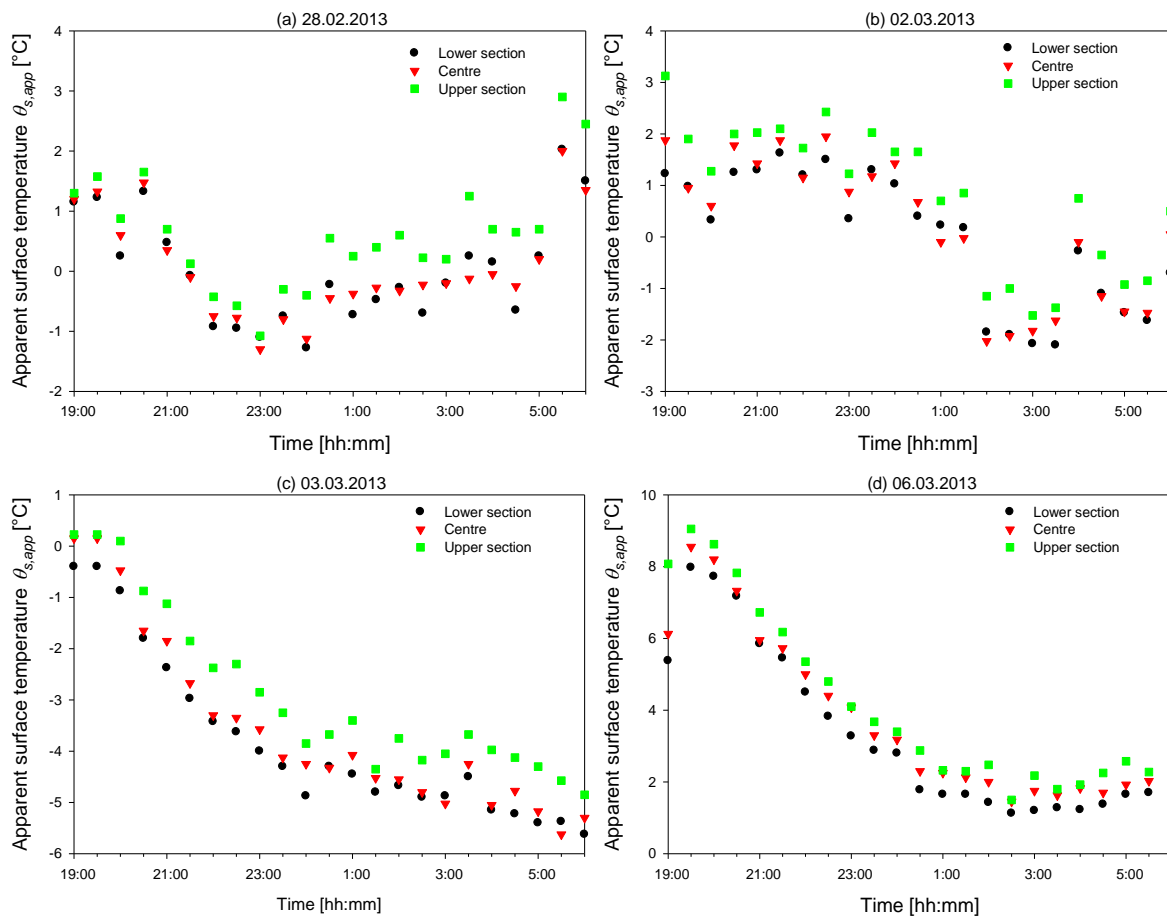
Fig. 5.19. Apparent surface temperatures on the thermograms for some nights (a – d)

(n = 23).

5.3.2 Significance of thermal radiation in U_{cs}-value

The variation of heat transfer coefficients due to convection and radiation during the nighttime measurement period are given in Fig. 5.20. The computed hourly convective heat transfer coefficient U_{cv} ranged between 2.8 W m^{-2} K^{-1} and 10.1 W m^{-2} K^{-1}. The corresponding wind speeds for the minimum and maximum U_{cv} values were 0.1 m s^{-1} and 6.1 m s^{-1}, respectively. As the wind speed increases, convection becomes the dominant mode of heat loss. In fact, U_{cv} at the exterior surface is never zero even when the wind speed is approximately 0 m s^{-1}. On the other hand, the radiative heat transfer coefficient U_{lir} ranged between 3.9 W m^{-2} K^{-1} and 5 W m^{-2} K^{-1}.
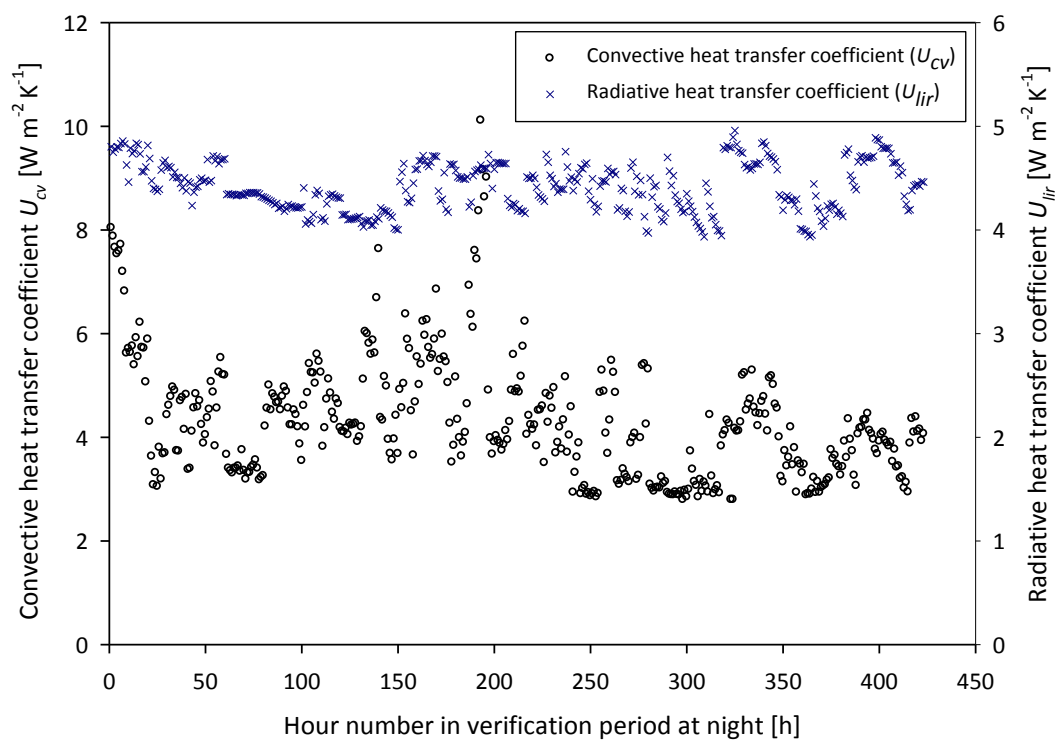
Fig. 5.20. Comparison of convective and radiative heat transfer coefficients with time (n = 423).

Based on the measurements from the big south-facing thermal box, the minimum and maximum U_{cs}-values were 4.12 W m^{-2} K^{-1} and 9.97 W m^{-2} K^{-1}, respectively (Fig. 5.21). The values are seemingly close to those of the standard (dashed line) as highlighted by the HORTEX system (Rath, 1992), where the U_{cs}-value at the wind speed of 4 m s^{-1} is about 7.56 W m^{-2} K^{-1}. It is also apparent from the figure that the U_{cs}-value is directly proportional to the wind speed.
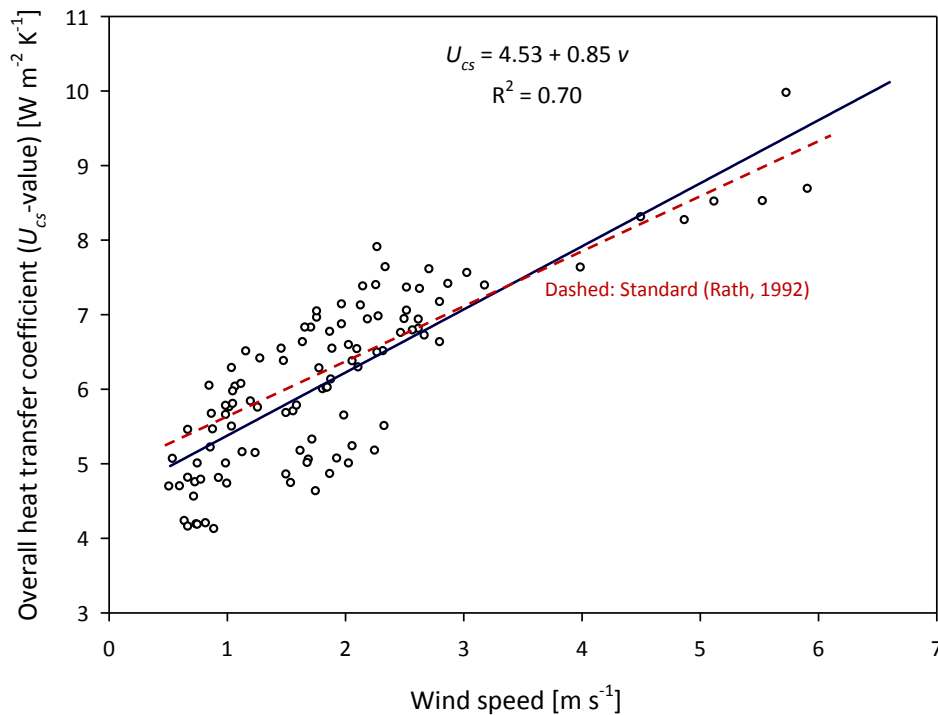
Fig. 5.21. Variation of U_{cs}-value as a function of wind speed (n = 106).

The proportions of both the radiative and the convective heat transfer coefficients to the overall heat transfer coefficient U_{cs}-value are presented in Fig. 5.22. As seen in Fig. 5.22(a), the ratio of U_{lir} to U_{cs}-value decreased with an increase in the wind speed. This declining trend of U_{lir} to U_{cs}-value ratio was predominant at low wind speeds. On the other hand, the ratio of U_{cv} to U_{cs}-value increased as the wind speed increased (Fig. 5.22(b)). Even though the wind speeds were mostly less than 3 m s^{-1}, it can be seen that wind speed had a stronger effect on both the U_{cv} and the U_{lir}. Considering the wind speed range (0.04 m s^{-1} to 6.1 m s^{-1}) during the measurement period, the ratio of U_{lir} to U_{cs}-value ranged between 0.37 and 0.78, while the ratio of U_{cv} to U_{cs}-value ranged from 0.35 to 0.87. From the models fitted to the data, the U_{lir} to U_{cs}-value ratio reduced by 41 % when the wind speed is increased from 0 m s^{-1} to 4 m s^{-1}. However, within the same wind speed range (0 m s^{-1} to 4 m s^{-1}), the ratio of U_{cv} to U_{cs}-value increased by 59 %. A fairly steep slope in the case of U_{cv} to U_{cs}-value ratio also confirms this effect by wind.

(a)

$U_{lir}/U_{cs} = 0.659 - 0.095\,v + 0.008\,v^2$

$R^2 = 0.538$

(b)

$U_{cv}/U_{cs} = 0.449 + 0.066\,v$

$R^2 = 0.607$
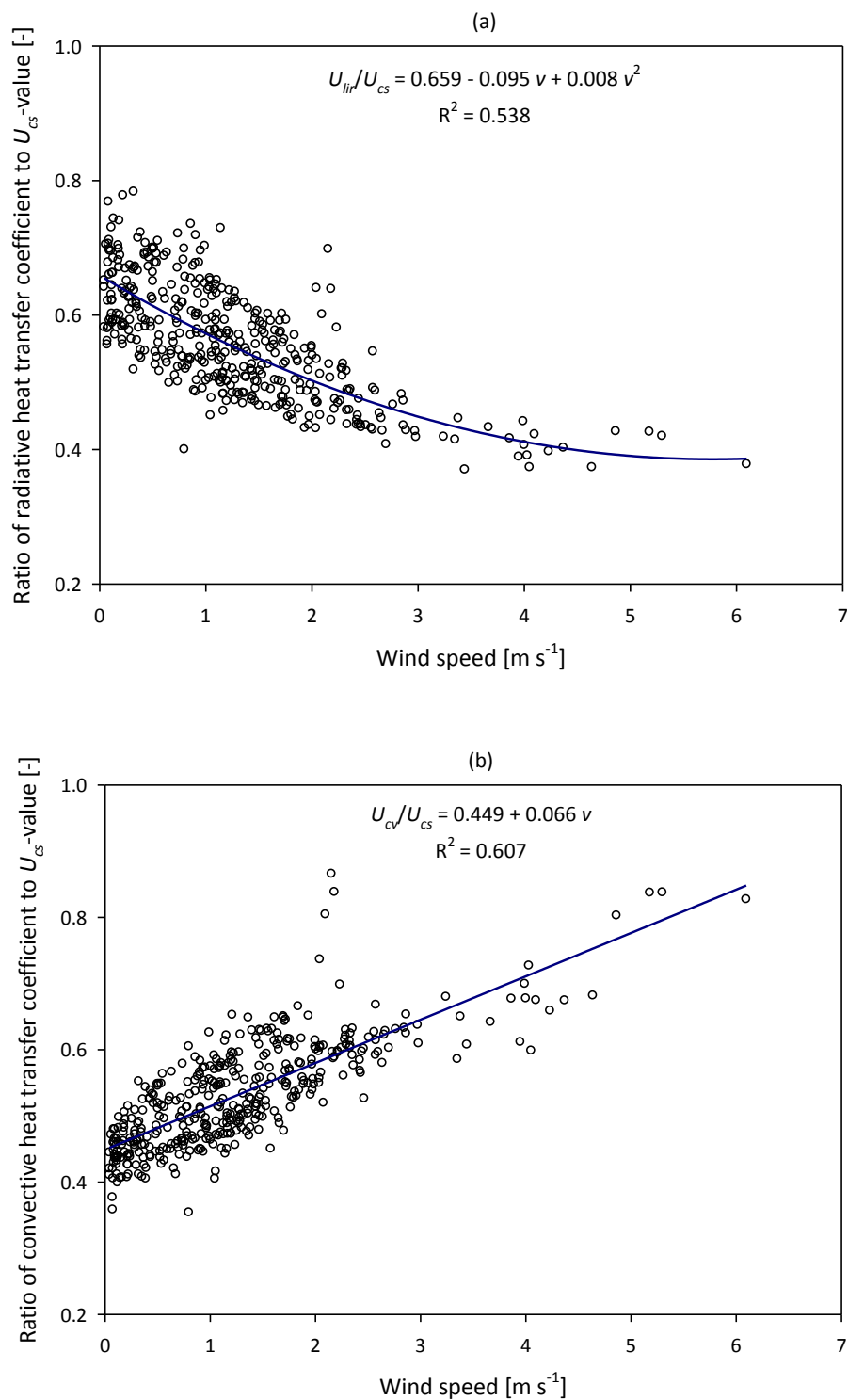
Fig. 5.22. Relationship between ratios of radiative (a) and convective (b) heat transfer coefficients to U_{cs}-value as a function of wind speed ($n = 423$).

5.4 Corrected *U*$_{cs}$-values as a Function of Cloudiness, Wind Speed and Surface Inclination

The *U*$_{cs}$-value of an entire greenhouse can be transformed into separate *U*$_{cs}$-values of roofs and walls by taking into consideration the corrections due to wind speed and cloudiness. The available wind-corrected *U*$_{cs}$-values in HORTEX (Rath, 1992) have been used to describe greenhouse heat losses. For a single float glass, the standard greenhouse *U*$_{cs}$-value of 7.56 W m^{-2} K^{-1} is based on an average wind speed of 4 m s^{-1}. The wind-corrected *U*$_{cs}$-value is expressed as (Rath, 1992):

$$U_{cs,v} = U_{cs,st} + \left(\frac{U_{cs,st}}{y_{c,8}} \cdot \left(x_{v,1} \cdot v + y_{c,9} \right) \right) \tag{5.1}$$

where,

$U_{cs,v}$	: wind-corrected U_{cs}-value	[W m^{-2} K^{-1}]
$U_{cs,st}$	: standard greenhouse U_{cs}-value at 4 m s^{-1}	[W m^{-2} K^{-1}]
$y_{c,8}$	: coefficient = 7.56 (Rath, 1992)	[-]
$x_{v,1}$	: coefficient = 0.35 (Rath, 1992)	[s m^{-1}]
v	: wind speed	[m s^{-1}]
$y_{c,9}$	: coefficient = -1.4 (Rath, 1992)	[-]

The estimated *U*$_{cs}$-values for both surface inclinations (roof and wall) as a function of the cloudiness and the wind speed are presented in Fig. 5.23. The data was derived from the measurements with the miniaturized thermal boxes. In the 3D-plot, the chosen wind speed ranging from 0 m s^{-1} to 4 m s^{-1} were obtained from the measured data. The wind speed of 4 m s^{-1} has been used previously as an average wind speed for the study location (Tantau, 1983; von Zabeltitz, 1982). The cloudiness factors were grouped into four categories (0.25, 0.5, 0.75 and 1) which lie in the range of 0 to 1. The 3D-plot shows that the *U*$_{cs}$-value is proportional to the wind speed and inversely proportional to the cloudiness. The influence of cloudiness on the *U*$_{cs}$-value is less marked than in the case of the wind speed. The transparency effect in the 3D-plot distinguished the two colours (cyan for the roof and grey for the wall). It is apparent that the *U*$_{cs}$-values differ from each other by approximately 0.45 W m^{-2} K^{-1}. Generally, the roof had higher *U*$_{cs}$-values than the walls under all wind and sky conditions.
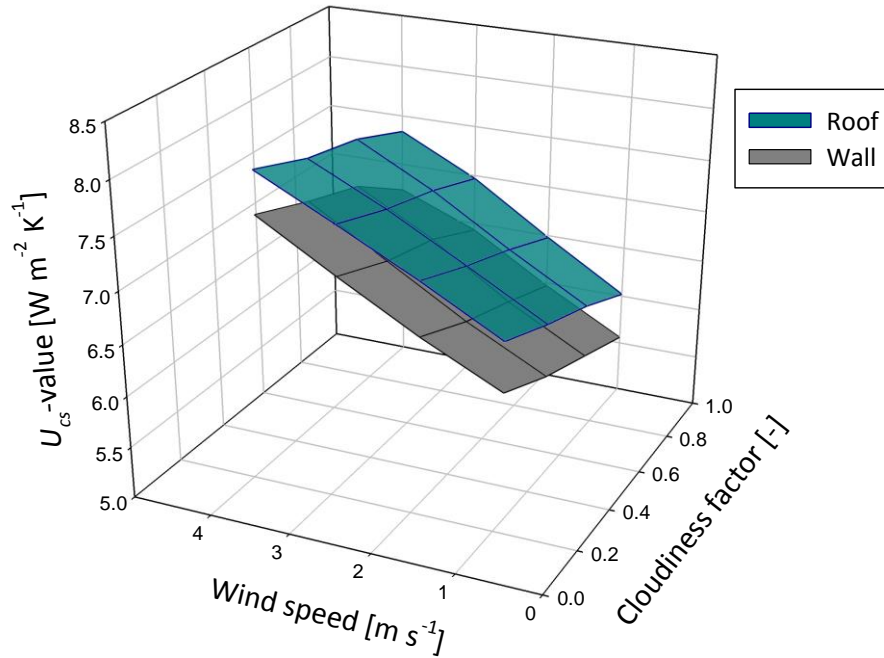
Fig. 5.23. U_{cs}-value as a function of cloudiness and wind speed for roofs and walls ($n = 4$).

A multilinear approach was used to check the influence of the cloudiness factor C and the wind speed v on the roof and wall U_{cs}-values. A coupled effect of both variables (C and v) was initially included. However, from statistical tests, the coupled effect of both variables presented a high p-value ($p > 0.05$). This points out that the combined effect ($C \cdot v$) is less sensitive to the U_{cs} model compared to the individual C and v variables. Since this coupled effect appeared to be an insignificant independent variable, it was therefore eliminated from the multilinear model. For a single glass greenhouse, the relationships between the U_{cs}-value, the cloudiness factor and the wind speed are expressed as:

Roof: $\quad\quad\quad U_{cs,sfg} = x_{u,8} + x_{u,9} \cdot C + x_{w,6} \cdot v$ $\quad\quad\quad\quad\quad\quad\quad$ (5.2)

Wall: $\quad\quad\quad U_{cs,sfg} = x_{u,10} + x_{u,11} \cdot C + x_{w,7} \cdot v$ $\quad\quad\quad\quad\quad\quad$ (5.3)

where,

$U_{cs,sfg}$: greenhouse U_{cs}-value for a single float glass $[W\ m^{-2}\ K^{-1}]$

v $\quad\quad$: wind speed $\quad\quad\quad\quad\quad\quad\quad\quad\quad\quad\quad$ $[m\ s^{-1}]$

C $\quad\quad$: cloudiness factor $\quad\quad\quad\quad\quad\quad\quad\quad\quad$ $[-]$

$x_{u,8}$ $\quad$: coefficient = 6.48 (empirical) $\quad\quad\quad\quad$ $[W\ m^{-2}\ K^{-1}]$

$x_{u,9}$ $\quad$: coefficient = -0.81 (empirical) $\quad\quad\quad$ $[W\ m^{-2}\ K^{-1}]$

$x_{w,6}$ $\quad$: coefficient = 0.415 (empirical) $\quad\quad\quad$ $[W\ s\ m^{-3}\ K^{-1}]$

$x_{u,10}$ $\quad$: coefficient = 6.01 (empirical) $\quad\quad\quad$ $[W\ m^{-2}\ K^{-1}]$

$x_{u,11}$: coefficient = -0.88 (empirical)   [W m^{-2} K^{-1}]

$x_{w,7}$: coefficient = 0.421 (empirical)   [W s m^{-3} K^{-1}]

A summary of the U_{cs}-values for the selected extreme wind and sky conditions is presented in Table 5.6. These values represent the four edge points of the 3D-plot for both roof and wall surfaces (see Fig. 5.23). The U_{cs}-values are generally low under calm (not windy) and cloudy conditions, and high under windy and clear-sky conditions. For a ground area of 10000 m^2, the roofs and the walls (side and end walls) constitute about 73 % and 27 % of the total Venlo greenhouse surface area, respectively. In this case, and assuming a wind speed of 4 m s^{-1} and an average cloudiness of 4 octas, the calculated area-weighted U_{cs}-value for an entire greenhouse is 7.57 W m^{-2} K^{-1}. This standardized value (Rath, 1992; von Zabeltitz, 1982) represents a greenhouse covered with a single float glass under average wind and sky conditions.

Table 5.6. U_{cs}-values of roofs and walls under different wind and sky conditions.

Surface	Calm, Clear-sky	Calm, Cloudy	Average wind speed, Clear-sky	Average wind speed, Cloudy
Roof	6.73	6.02	7.89	7.34
Wall	6.25	5.56	7.48	6.73

Note: U_{cs}-values in W m^{-2} K^{-1}; Calm: ≈ 1 m s^{-1}; Average wind speed: 4 m s^{-1}; Clear-sky: < 2 octas; Cloudy: ≈ 8 octas

A correction factor *CF* is necessary for adjusting the U_{cs}-values especially for well-insulated greenhouses. This correction should consider the prevailing outdoor conditions, such as wind and cloudiness. For this reason, the data was obtained from measurements with the thermal boxes. The U_{cs}-values from HORTEX (Rath, 1992) are only wind-corrected. The strong interaction between radiative and convective exchanges at the exterior surface (sub-section 5.3.2) points out that it is necessary to consider both cloudiness and wind speed parameters, hence the need to correct the existing U_{cs}-values. If a model is known for a single glass ($U_{cs,st}$ = 7.56 W m^{-2} K^{-1}) greenhouse, one can transform it to other $U_{cs,st}$ values with a *CF* as follows (assuming a multiplicative effect similar to Rath (1992)):

$$CF = U_{cs,st} \cdot \frac{1}{x_{u,12}}$$ (5.4)

where,

    CF : correction factor   [-]

    $U_{cs,st}$: standard greenhouse U_{cs}-value at 4 m s^{-1} [W m^{-2} K^{-1}]

    $x_{u,12}$: coefficient = 7.56 (Rath, 1992)   [W m^{-2} K^{-1}]

The roof and wall U_{cs}-values were computed using Eqs. (5.2) and (5.3), respectively, with the wind speed of 4 m s^{-1} and the selected cloudiness factors C (0, 0.385 and 1). The average U_{cs}-values for roofs and walls are compared with the existing wind-corrected data as shown in Fig. 5.24. The U_{cs}-values deviate from each other at the C values of 0 and 1. The U_{cs}-values are in best agreement at a C value of 0.385. This indicates that the former measurements were done at an average C of 0.385 (approximately 3 octas).
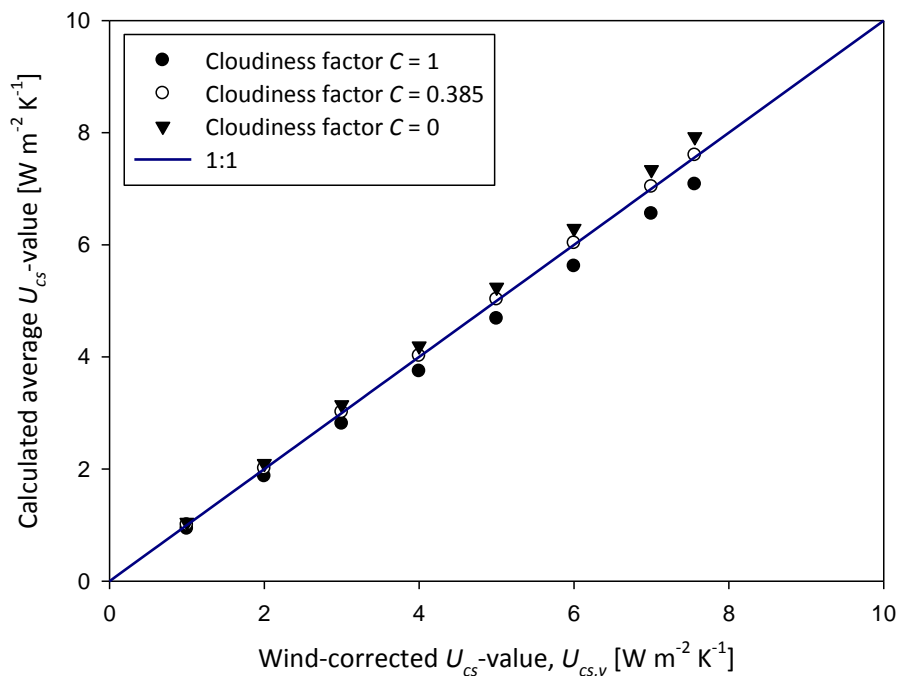
Fig. 5.24. Comparison of average U_{cs}-values and the equivalent wind-corrected data (n = 8).

At a wind speed of 4 m s^{-1} and a cloudiness factor C of 0.385 (value from Fig. 5.24), the average U_{cs}-value is 7.56 W m^{-2} K^{-1}. With this standard U_{cs}-value, the correction factor CF is 1. An appropriate CF is necessary to ensure that there is no change in all other average U_{cs}-values at the wind speed of 4 m s^{-1} and the C of 0.385. For other U_{cs}-values less than 7.56 W m^{-2} K^{-1}, the CF is expected to be less than 1. With the U_{cs}-value of 4.5 W m^{-2} K^{-1}, for

example, the *CF* is 0.6 (i.e. 4.5 divided by 7.56). At an even lower U_{cs}-value of 1.5 W m^{-2} K^{-1}, the corresponding *CF* is 0.2. The *CF* is therefore generally useful for calculating the new corrected U_{cs}-values ($U_{cs,n}$). The existing wind-corrected U_{cs}-values ($U_{cs,v}$) have $U_{cs,st}$ and *v* as the model inputs (Rath, 1992). Hence, for a single float glass and the *CF* created with the measured values from this study, the $U_{cs,n}$ is expressed as follows:

$$U_{cs,n} = \left(U_{cs,sfg} \cdot \frac{1}{x_{u,12}} \right) \cdot \left(U_{cs,st} + \left(\frac{U_{cs,st}}{y_{c,8}} \cdot \left(x_{v,1} \cdot v + y_{c,9} \right) \right) \right) \tag{5.5}$$

where,

$U_{cs,n}$	: new corrected U_{cs}-value	[W m^{-2} K^{-1}]
$U_{cs,sfg}$	: greenhouse U_{cs}-value for a single float glass	[W m^{-2} K^{-1}]
$x_{u,12}$	: coefficient = 7.56 (Rath, 1992)	[W m^{-2} K^{-1}]
$U_{cs,st}$	: standard greenhouse U_{cs}-value at 4 m s^{-1}	[W m^{-2} K^{-1}]
$y_{c,8}$	: coefficient = 7.56 (Rath, 1992)	[-]
$x_{v,1}$	: coefficient = 0.35 (Rath, 1992)	[s m^{-1}]
v	: wind speed	[m s^{-1}]
$y_{c,9}$	: coefficient = -1.4 (Rath, 1992)	[-]

The multilinear versions of $U_{cs,n}$ for roof and wall surfaces as a function of $U_{cs,st}$, *C* and *v* are thus obtained by incorporating Eqs. (5.2) and (5.3) into Eq. (5.5). The influences of the two variables (cloudiness factor and wind speed) are included in the individual models. The overall expressions of $U_{cs,n}$ for the roof and wall surfaces are given by:

$$\text{Roof:} \quad U_{cs,n} = \left(\left(x_{u,8} + x_{u,9} \cdot C + x_{w,6} \cdot v \right) \cdot \frac{1}{x_{u,12}} \right) \cdot \left(U_{cs,st} + \left(\frac{U_{cs,st}}{y_{c,8}} \cdot \left(x_{v,1} \cdot v + y_{c,9} \right) \right) \right) \tag{5.6}$$

$$\text{Wall:} \quad U_{cs,n} = \left(\left(x_{u,10} + x_{u,11} \cdot C + x_{w,7} \cdot v \right) \cdot \frac{1}{x_{u,12}} \right) \cdot \left(U_{cs,st} + \left(\frac{U_{cs,st}}{y_{c,8}} \cdot \left(x_{v,1} \cdot v + y_{c,9} \right) \right) \right) \tag{5.7}$$

where,

$U_{cs,n}$	: new corrected U_{cs}-value	[W m^{-2} K^{-1}]
C	: cloudiness factor	[-]
v	: wind speed	[m s^{-1}]
$x_{u,8}$	: coefficient = 6.48 (empirical)	[W m^{-2} K^{-1}]
$x_{u,9}$	: coefficient = -0.81 (empirical)	[W m^{-2} K^{-1}]

$x_{w,6}$: coefficient = 0.415 (empirical)   [W s m^{-3} K^{-1}]

$x_{u,12}$: coefficient = 7.56 (Rath, 1992)   [W m^{-2} K^{-1}]

$U_{cs,st}$: standard greenhouse U_{cs}-value at 4 m s^{-1} [W m^{-2} K^{-1}]

$y_{c,8}$: coefficient = 7.56 (Rath, 1992)   [-]

$x_{v,1}$: coefficient = 0.35 (Rath, 1992)   [s m^{-1}]

$y_{c,9}$: coefficient = -1.4 (Rath, 1992)   [-]

$x_{u,10}$: coefficient = 6.01 (empirical)   [W m^{-2} K^{-1}]

$x_{u,11}$: coefficient = -0.88 (empirical)   [W m^{-2} K^{-1}]

$x_{w,7}$: coefficient = 0.421 (empirical)   [W s m^{-3} K^{-1}]

Transforming the measured U_{cs}-values into those of roofs and walls is then possible with the obtained CF. The new corrected multi-effect U_{cs} model ($U_{cs,n}$) can be expressed with the standard greenhouse U_{cs}-value at 4 m s^{-1} ($U_{cs,st}$), the cloudiness factor C and the wind speed v as the model inputs. The simplified $U_{cs,n}$ models are therefore expressed as:

$$\text{Roof:} \quad U_{cs,n} = U_{cs,st} \cdot \left(y_{c,10} + y_{c,11} \cdot C + x_{v,2} \cdot v + x_{w,8} \cdot C \cdot v + y_{u,7} \cdot v^2 \right) \qquad (5.8)$$

$$\text{Wall:} \quad U_{cs,n} = U_{cs,st} \cdot \left(y_{c,12} + y_{c,13} \cdot C + x_{v,3} \cdot v + x_{w,9} \cdot C \cdot v + y_{u,8} \cdot v^2 \right) \qquad (5.9)$$

where,

$U_{cs,n}$: new corrected U_{cs}-value   [W m^{-2} K^{-1}]

$U_{cs,st}$: standard greenhouse U_{cs}-value at 4 m s^{-1} [W m^{-2} K^{-1}]

C : cloudiness factor   [-]

v : wind speed   [m s^{-1}]

$y_{c,10}$: coefficient = 0.697 (empirical)   [-]

$y_{c,11}$: coefficient = -0.087 (empirical)   [-]

$x_{v,2}$: coefficient = 0.084 (empirical)   [s m^{-1}]

$x_{w,8}$: coefficient = -4.9 · 10^{-3} (empirical)   [W s m^{-3} K^{-1}]

$y_{u,7}$: coefficient = 2.5 · 10^{-3} (empirical)   [W s^2 m^{-4} K^{-1}]

$y_{c,12}$: coefficient = 0.646 (empirical)   [-]

$y_{c,13}$: coefficient = -0.095 (empirical)   [-]

$x_{v,3}$: coefficient = 0.081 (empirical)   [s m^{-1}]

$x_{w,9}$: coefficient = -5.3 · 10^{-3} (empirical)   [W s m^{-3} K^{-1}]

$y_{u,8}$: coefficient = 2.6 · 10^{-3} (empirical)   [W s^2 m^{-4} K^{-1}]

To check the performance of the developed models, another step involved comparing the new corrected U_{cs}-value ($U_{cs,n}$) with the former wind-corrected U_{cs}-value ($U_{cs,v}$). A comparison of the roof and wall $U_{cs,n}$-values (including their averages) and the $U_{cs,v}$-values is shown in Fig. 5.25. The values were similarly selected at intervals of 1.5 W m^{-2} K^{-1} between the two set fixpoints (0 W m^{-2} K^{-1} and 7.56 W m^{-2} K^{-1}). Based on the model improvements, the $U_{cs,n}$-values of the roof are slightly higher than those of the wall. This was more pronounced for high U_{cs}-values close to 7.56 W m^{-2} K^{-1}. However, it is seen from the figure that the average $U_{cs,n}$-values are very close to the 1:1 line. This was generally the case for all average $U_{cs,n}$-values ranging between 0 W m^{-2} K^{-1} and 7.56 W m^{-2} K^{-1}.
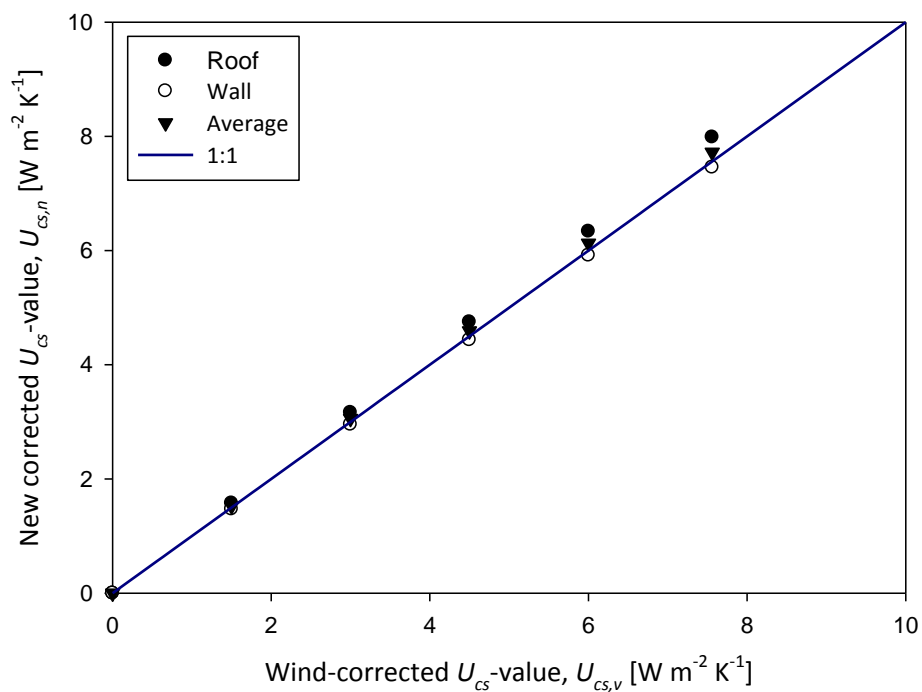
Fig. 5.25. Comparison of new corrected U_{cs}-values and the existing wind-corrected data with C = 0.385 and v = 4 m s^{-1} (n = 6).

In order to check the effect of the model inputs in Eqs. (5.8) and (5.9) on the $U_{cs,n}$, some assumptions were subjectively set to define a given range in each of the variables. For instance, in HORTEX, the standard greenhouse U_{cs}-values ($U_{cs,st}$) at a wind speed of 4 m s^{-1} are about 7 W m^{-2} K^{-1} and 3 W m^{-2} K^{-1} for fairly bad and good glass insulations, respectively (Rath, 1992). From this work, the average cloudiness factors C of 0.1 and 0.9 define the clear-sky and overcast conditions, respectively. It is also assumed that the $U_{cs,n}$ models work well within the wind speed v range of 0 m s^{-1} to 7 m s^{-1}, and are thus less

suitable for $v > 7$ m s^{-1}. With the selected ranges of $U_{cs,st}$, C and v, the following assumptions were therefore taken into consideration:

a) $\Delta U_{cs,st} = 4$ W m^{-2} K^{-1}

b) $\Delta C = 0.8$

c) $\Delta v = 7$ m s^{-1}

where,

$\Delta U_{cs,st}$: difference in standard greenhouse U_{cs}-values   [W m^{-2} K^{-1}]

ΔC : difference in cloudiness factors   [-]

Δv : difference in wind speeds   [m s^{-1}]

Based on the set assumptions, the effects of the individual variables on the corrected $U_{cs,n}$ models are presented in Table 5.7. The model inputs and their coefficients for the roof and the wall were obtained from Eqs. (5.6) and (5.7), respectively. In the linear combination of the model variables, $U_{cs,st}$ and $U_{cs,st} \cdot v$ showed the highest influence for roofs and walls. However, $U_{cs,st} \cdot C \cdot v$ was the least influential input in the models. Despite the variation in rating, the independent variables jointly contribute in calculating the $U_{cs,n}$ for roofs and walls ($p < 0.05$). The quadratic effect in the $U_{cs,n}$ models with the input v resulted from the new correction (with both C and v parameters) applied to the existing wind-corrected U_{cs}-values (Rath, 1992).

Table 5.7. Effects of the model inputs on the new corrected U_{cs}-values for roofs and walls.

Model input (with coefficient)	Absolute factor effect on $U_{cs,n}$ [W m^{-2} K^{-1}]		Input influence on $U_{cs,n}$ [%]	
	Roof	Wall	Roof	Wall
$\Delta U_{cs,st}$	> 2.7	> 2.5	45.57	44.13
$\Delta U_{cs,st} \cdot \Delta C$	> 0.2	> 0.3	4.54	5.19
$\Delta U_{cs,st} \cdot \Delta v$	> 2.3	> 2.2	38.45	38.73
$\Delta U_{cs,st} \cdot \Delta C \cdot \Delta v$	< 0.12	< 0.12	1.83	1.91
$\Delta U_{cs,st} \cdot (\Delta v)^2$	> 0.5	> 0.5	9.61	10.04

6 DISCUSSION

6.1 Radiation Exchange as Influenced by Surface Inclination and Orientation

6.1.1 Surface inclination effects

Unlike in the big south-facing thermal box where the view factor remained unchanged, the case was different in the miniaturized thermal boxes. By changing the inclination angle β, the view factor is similarly altered (Evins et al., 2014). In this respect, when β changes from 24° (roof) to 90° (wall), the view factor of the exterior surface to the sky F_{sky} is reduced while that to the surrounding ground objects F_{gnd} is increased. Based on the equations in the literature which depend on the inclination angle (Romila, 2012; EnergyPlus 8.0, 2013; Walton, 1983), the roof has a sky view factor F_{sky} of 0.94 while the vertical wall has an F_{sky} of 0.35. At an inclination angle of 24°, the roof is the most exposed component of the greenhouse structure. This in turn led to lower surface-to-air temperature differences ΔT_{s-a} of the roofs compared to those of the walls. This implies that the sky-oriented exterior roof surfaces are cooled more than the vertical walls (Ronoh and Rath, 2015b; Algarni and Nutter, 2015; Kehrer and Schmidt, 2008).

However, under an overcast condition, the variation in inclination angles did not show any significant changes ($p > 0.05$) in the net longwave radiation loss. This supports the fact that the radiative heat flux is not well connected to the surface inclination as it merely depends on the temperature difference (Dimitriadou and Shea, 2012). As expected, the exposed roof loses more heat to the sky than the walls under clear-sky conditions. The surface of interest represents that of the Venlo greenhouse design where the roof fraction is low (von Elsner et al., 2000). This outcome agrees well with the observation that the nighttime heat loss by longwave radiation affects any building surface whose roof fraction is high (Porson et al., 2010). This is equivalent to saying that the sensible heat flux is higher when the roof area is more than the wall area. The reduced roof surface area (an area of major heat loss) in Venlo greenhouses is therefore beneficial in the overall reduction of the heating costs.

Despite the differences in the view factors of the surfaces (roof and wall) to the sky, the variability of the radiative exchange is more restricted at night than during the day (Oliveti et al., 2012). The high view factor of the roof surface to the sky increases the greenhouse-

sky radiative heat exchange. However, the heat loss through the walls is compensated by the radiative exchange to the air and the surrounding objects. This explains the insignificant effects ($p > 0.05$) of the surface inclination on the measured net radiation R_n values. The effect was more pronounced during overcast nights (about 6 to 8 octas) with less negative R_n values. Li et al. (2014) also noted that the roof effect does not have a significant impact on the nighttime heat loss due to the energy limitation. The case would be different during the day when solar radiation is present. It was, however, noticed that the R_n values were more negative (increase in radiative loss) under clear-sky conditions (less than 2 octas) than under overcast conditions (about 8 octas). During the clear-sky nights, the configuration of the surface (and thus the view factor effect) contributed to the variation in the net radiation loss. Due to the exposure of the roof to the sky, the mean R_n was higher at the roof than at the wall. The net radiation data served not only as an additional parameter (other than temperature and wind speed) but also as a tremendous insight of heat loss from the exterior surface.

The presence of radiation influences the roof and the wall surface temperatures to various extents depending on the emissivity and the view factor effect. The surface temperature in turn influences the weak natural convection flows. An observation by Sharma et al. (2008) indicates that the effect of surface radiation on turbulent natural convection depends strongly on the inclination of the surface. Thus, the interaction of these heat transfer mechanisms at the cover surface (natural convection and surface radiation) is of practical interest. The smaller surface-to-air temperature differences $\Delta T_{s\text{-}a}$ of the roof compared to those of the wall at various wind speeds can be explained by the fact that the exposed roofs have higher forced convective heat loss, especially at the windward side (Liu et al., 2015). A study by Svensson (2004) reported an insignificant effect of the surface geometry (thus the view factor) and the air temperature, and hence an indication that the view factor is strongly correlated to the surface temperature. This relationship is in agreement with observations by other authors for several areas (Eliasson, 1996; Chapman et al., 2001; Nunez et al., 2000).

6.1.2 Surface orientation effects

Southerly and westerly wind directions were generally dominant during the measurement period. This agrees well with an observation by Voigtländer et al. (2006) about the distribution of wind directions in Germany. It is also worth noting that the dominant wind speed class was that between 1.5 m s^{-1} and 3 m s^{-1}. It was also apparent that wind was very variable both in direction and speed. An increase in wind speed reduces the surface resistance (Jones, 2014); this generally leads to an increased heat loss which is largely brought about by convection.

Based on the trends of the surface-to-air temperature difference ΔT_{s-a}, the deviation between the ΔT_{s-a} values of the roof and the wall (i.e. ΔT_{W-R}) was not significantly affected by the box orientation. In a study by Nie et al. (1992), the difference in average daytime net radiation R_n can be as high as 15 % to 20 %, especially when the north and south orientations are considered. Interestingly, this effect of orientation on nighttime R_n from this study was insignificant (Ronoh and Rath, 2015b). This indicates that the R_n was little affected by varying the orientation of the thermal boxes. Generally, these orientations are applicable, especially during the day, in maximizing winter sunlight and heat gain depending on whether the greenhouse is a single-span or a gutter-connected type (Sanford, 2011).

6.2 Modelling of Thermal Radiation Exchange

6.2.1 Radiation model and its effects for night situation

The radiation exchange is an important factor in the thermal environment of building and ground surfaces (van Thanh, 1973). At night, longwave radiation is the sole source of radiant energy to the surface. During this time, the exterior surface exchanges longwave radiation with the sky, the ground and the surrounding elements (Ronoh and Rath, 2015a). The longwave radiation exchange between surfaces is dependent on the surface temperatures, spatial relationships between the surfaces and the surroundings, and relevant material properties (emissivity and absorptivity) of the surfaces. The sum of the sky downwelling longwave radiation and the longwave radiation from the surrounding gives the total modelled downwelling longwave radiation $LWR_{d,t}$. An additional component accounted for the longwave radiation from the surrounding objects such as

trees adjacent to the measurement site. This is in agreement with an observation by Howard and Stull (2013) while modelling the downwelling longwave radiation under clear skies. Although the work of Howard and Stull (2013) was applied on alpine ski racing (groomed ski run), the longwave radiation phenomena at the reference surface remain comparable. This implies that integrated contributions from the entire upper hemisphere above the surface of interest are of great concern while modelling the radiation exchange. The individual contributions of radiation are sequentially weighted by their view factors (Howard and Stull, 2013). These view factors determine which part of the total radiation is directly intercepted by the surface (Vollebregt and van de Braak, 1995). The simulated $LWR_{d,t}$ values compared well with the measurements by the CNR 4 net radiometer.

In modelling of the downwelling longwave radiation from the sky LWR_d, the clear-sky atmospheric emissivity ε_{cs} parameterizations, which use water vapour pressure and air temperature, had the best scores. This confirms that the near-surface water vapour pressure is an important variable due to its impact as a greenhouse gas and should be applied in conjunction with the air temperature (Sedlar and Hock, 2009). The best parameterization for ε_{cs} estimation under both day and night situations was the Sugita and Brutsaert model (see Tables 5.2 and 5.3). It requires only the air temperature and water vapour pressure measurements. Generally, the Duarte et al. (2006) and the Kruk et al. (2010) models underestimated the ε_{cs} values while the Idso (1981) model registered an overestimation of the ε_{cs}. Accurate estimation of the ε_{cs} directly influences the computation of the effective atmospheric emissivity. According to Ryu et al. (2008), LWR_d estimation becomes challenging because complex atmospheric components might affect atmospheric emissivity and could be the main reason of model uncertainties (Choi, 2013). Rizou and Nnadi (2007) pointed out that heterogeneous land cover types could affect atmospheric emissivity as well as air temperature and water vapour.

The estimated cloudiness factors (C_{octas} from weather watcher and C_{maps} from analysed weather maps) were necessary for the radiation modelling (Table B2, Appendix B). These cloudiness factors were then implemented into the effective atmospheric emissivity ε_a parameterization. The inclusion of the cloudiness factor in the model parameters provides an appreciable improvement on the simulation (Ronoh and Rath, 2014). Clouds are known

to alter longwave radiative profile through emission of longwave radiation from cloud base (Key and Minnett, 2004). Generally, the presence of clouds increases atmospheric irradiance received at the surface. This could be attributed to the fact that radiation from water vapour and carbon dioxide in the lower atmosphere gets supplemented by emission from clouds in the waveband which the gaseous emission lacks (Iziomon et al., 2003). However, clouds should not be expected to increase sky radiation by more than 40 % even under completely overcast conditions (Kimball et al., 1982). Cooler clouds, on the other hand, reduce the amount of heat that radiates into space by absorbing the heat radiating from the surface and re-radiating some of it back down. Despite this scenario, this cooling effect of clouds is partly offset by a blanketing effect (reflection of infrared radiation from the undersides of clouds).

With precise computation of the effective thermal radiation exchange $Q_{s,eff}$ and the reflected component of atmospheric downwelling longwave radiation LWR_d, the upwelling longwave radiation $LWR_{u,t}$ can then be obtained (Ronoh and Rath, 2014). The effective surface temperature $T_{s,eff}$ (for glass and glazing bars) and the surface emissivity strongly influence the output of $LWR_{u,t}$. To a certain degree, vegetation influences the $LWR_{u,t}$ since a thick vegetation cover can act to retard the radiation emitted from the ground via multiple reflections.

6.2.2 Radiation model and its effects for day situation

The thermal radiation exchange influences the entity of the maximum thermal loads which act of any building surface (Oliveti et al., 2012). The thermal radiative heat transfer consists of the shortwave solar radiation against the external surfaces of buildings (such as greenhouses) during the day and the longwave radiation exchange which occurs throughout the day and night (Liu and Harris, 2013). Detailed thermal radiation models that count for the thermal exchange between the exterior surfaces of buildings and the surroundings are necessary to calculate the energy balance on the exterior surfaces (Romila, 2012). Unlike measurement of solar radiation, longwave radiation instrumentation (e.g. pyrgeometer) is nowadays usually deployed at weather stations specifically designed for scientific purposes (Sicart et al., 2006). It is not so common in the most habitual automated weather stations. Hence, all energy balance models estimate

longwave components independently through different physical relations and parameterizations.

The daytime longwave radiation exchange at the greenhouse surfaces, just like at night, was also influenced by the air temperature, the water vapour pressure and the cloudiness factor. The greenhouse surfaces receive energy from the sky and the nearby objects in the form of longwave radiation which is continuously present during the day and at night. In addition to the longwave radiation, these surfaces receive a substantial amount of energy from the sun in the form of solar radiation (van Thanh, 1973). Due to presence of this solar radiation during the day, the measurement system was however not heated. This allowed exclusion of solar radiation data from the longwave radiation data and thus a possibility to test the models. Under daytime situation, therefore, the magnitude of net shortwave radiation was higher than the net longwave radiation. The diffuse-to-global solar radiation correlation, originally developed by Liu and Jordan (1960), has been used extensively as a technique providing accurate results, although it is latitude-dependent. The 4th order polynomial expression helps to establish the relationship between the hourly diffuse fraction F_d and the hourly clearness index I_c using the measured data on a horizontal surface (Jacovides et al., 2006). From the available dataset (2009 to 2013), this polynomial expression showed a good agreement for $0 \leq I_c \leq 0.75$. Another important observation is that for $I_c > 0.75$, the diffuse fraction F_d does not decrease further. Despite a paucity of data for $I_c > 0.75$, F_d is relatively large at high I_c values. For $I_c > 0.75$, an average F_d value of 0.2 was found to be appropriate and this is in agreement with the value given by Miguel et al. (2001).

During the day, solar radiation is the dominant flux under clear, dry skies. Solar and longwave fluxes are both important with cloudy skies. Cloudiness, similarly, alters the solar radiation profile through scattering and absorption of the incident solar radiation. A portion of the energy reaching the surface is reflected skyward where it may again interact with clouds. These radiative interactions constitute the surface cloud radiative forcing over a given area, a factor used to determine the impact of clouds on irradiance (Key and Minnett, 2004). The larger insolation increases the surface temperature (Moene and van Dam, 2014) and thus resulting in the higher total upwelling longwave radiation

LWR$_{u,t}$. Since the developed measurement system (big thermal box) remained closed during the specific daytime investigation period, the effective surface temperature $T_{s,eff}$ was higher than the air temperature T_a. However, the difference between these temperatures (T_a and $T_{s,eff}$) was not great unlike for the night situation where the system was heated. At temperature T_a, air is brought in contact with the surface by the turbulent winds and thereafter it warms up and takes heat out of the surface since $T_a < T_{s,eff}$.

For inclined surfaces such as those used in this study, it is necessary to consider the radiation reflected onto the surface by adjacent surfaces (Hay, 1979). According to Gulin et al. (2013), the classical approach to the modelling of the reflected radiation assumes that the reflected rays are diffuse. This means that the coefficients of reflection of the beam and the diffuse rays are identical. The global and diffuse solar irradiance on horizontal are commonly measured at the meteorological stations. The developed radiation models are then useful in estimating the total solar irradiance (beam, diffuse and reflected) on the tilted surfaces. The tested models can be useful in accurately predicting the annual collectable solar radiation on south-facing surfaces. Quantification of the total irradiance is very important on different exterior building surfaces such as in the energy-efficient control of indoor greenhouse climate.

6.2.3 Net radiation balance

The net radiation R_n is a measure of the fundamental energy available at greenhouse surfaces. The R_n at the surface is typically positive during the day (gain of energy) and is somewhat close to the net global radiation. On the other hand, the nighttime R_n is negative (loss of energy) and this loss can increase for heated systems (Castilla, 2013). At night, with the absence of solar radiation, the incoming longwave radiation from sky and surroundings are usually not enough to compensate for the upwelling longwave radiation from greenhouse surfaces (van Thanh, 1973). A negative sign of net radiation (net radiation loss) during nighttime implies the radiation flux off the reference cover surface to the sky. Hence, it follows that the surface loses energy by longwave radiation. This radiation heat loss is intensive under some weather conditions. In particular, this phenomenon frequently happens during clear-sky nights (Mesmoudi et al., 2010). This

explains the fact that radiation loss to space decreases with increasing cloudiness. Basically, the increased clouds do not encourage emission of heat from the objects below.

The results attests the fact that energy demand of a greenhouse is often based on the heat balances at the exterior surfaces, inner surfaces (linked via conduction) and zone air (linked via convection). The exterior atmospheric conditions are therefore useful in calculation of the energy needed to maintain a given inside air temperature range (Evins et al., 2014; Pedersen et al., 1997). The nature of surface affects its net radiation exchange with the sky. From the thermograms, surface temperatures slightly dropped due to light rain influence. This implies that rain is less strongly affecting the upwelling longwave radiation from the surface LWR_u. An observation by Katsaros and Buettner (1969) supports the fact that rain falling on a warmer or cooler surface can greatly alter its temperature. This can happen especially when the film of water on the surface reaches a certain thickness. However, rain is rarely singly associated with very low temperature (Nijskens et al., 1984). In a nutshell, the surface temperature and the effective surface emissivity are the main parameters which enable quantification of LWR_u from the surface (Ferreira et al., 2012). Since the sensor field of view was identical for all the net radiometers, the heating system (due to placement of heating rods) contributed to variation in the surface temperatures. This effect was clearly evident (see Fig. 5.18) at night when heating of the big south-facing thermal box system was necessary.

6.2.4 Applicability of the models

6.2.4.1 Evaluation of the radiation models

The developed solar radiation models with the respective conversion factors compared well with the measurements. The values of coefficient of determination (R^2) for total solar irradiance on the inclined surface and the reflected radiation component were 0.983 and 0.965, respectively. The results imply that it is practical to calculate the total solar irradiance on any surface (inclined or horizontal) and for any location other than the measurement site considered in this study. Based on the global and the diffuse radiation data for any location, the coefficients of the 4th order polynomial correlation relating the diffuse fraction with the clearness index need, however, to be rechecked.

Other than the cloudiness, the variables in the longwave radiation models (downwelling and upwelling) can be either measured, computed or obtained from the agricultural weather stations. Thus, in essence, these radiation models are transferable and can be used to predict the radiation exchange at the exterior surfaces of greenhouses or any other buildings in virtually all regions with different climatic conditions. Under both day and night situations, the R^2 for the longwave radiation simulation with the cloudiness factor C_{octas} (by weather watcher) were in all cases less than those obtained due to simulation with the cloudiness factor C_{maps} (from analysed weather maps). Additionally, simulation of longwave radiation with C_{maps} led to the lowest errors (BIAS, RMSE, MAE and PMRE) compared to simulation with C_{octas}. This means that for this kind of energy application the map-based simulation data are accurate and precise enough. For both $LWR_{d,t}$ and $LWR_{u,t}$ models, the nighttime simulation was better and more accurate than the daytime simulation. This can be attributed to the solar radiation effects on the cloudiness prediction. Despite these slight variations, the usage of the cloudiness factors showed no significant difference ($p > 0.05$) in terms of radiation simulation.

6.2.4.2 Model sensitivity analysis

The downwelling longwave radiation $LWR_{d,t}$ varies with air temperature T_a, cloudiness C and relative humidity RH. The trend (see Fig. 5.16) attests to the fact that T_a is the major factor in the model. Additionally, the sensitivity index SI of T_a is greater than one while for the parameters C and RH, the $SI < 0.2$. The higher the SI, the higher the sensitivity of results to changes in that parameter. Just like RH, clouds did not show appreciable effect on the $LWR_{d,t}$ (Long, 2005). This also explains the fact that errors related to longwave radiation simulation with the two cloudiness approaches (values from the weather watcher and the analysed weather maps) are not significantly different ($p > 0.05$).

The parameter C appears to be more sensitive in the effective thermal radiation exchange $Q_{s,eff}$ model ($SI > 0.2$) than in the $LWR_{d,t}$ model ($SI < 0.2$). Although clouds reflect some downward radiation back to space, they also reradiate infrared energy back towards the earth's surface. This implies clouds increase the longwave radiation to the surface, thereby enhancing the net cooling effect in the daytime but a net warming at night. These factors (T_a, C and RH) are interrelated and they jointly influence the radiation model

output. Overall, T_a and the temperature difference between the exterior surface and air ΔT_{s-a} are the key parameters in the $LWR_{d,t}$ and $Q_{s,eff}$ models, respectively (see Table 5.5). This is in agreement with the Stefan-Boltzmann law where the rate of longwave energy emission is proportional to the absolute surface temperature raised to the fourth power.

6.3 Significance of Radiative Heat Transfer in the U_{cs}-value Model

6.3.1 Interaction between radiation and convection at the greenhouse surface

The heat exchange by radiation is very important at the greenhouse surfaces (Vollebregt and van de Braak, 1995). However, at the exterior surfaces, there is an interaction between radiation and convection. Convection occurring at the external building surfaces is predominantly wind-driven forced convection. This implies that the exchange with the outside air is directly influenced by wind speed. This is in agreement with a similar explanation reported by Jolliet et al (1991) in terms of radiative and convective losses for a cladding material with or without screens. Based on the different models for calculating the convective heat transfer coefficient U_{cv}, convection dominates the heat loss as wind speed increases. However, as the wind speed decreases, radiation takes over as the dominant mode. At low wind speeds, there was scattering of data describing the ratio of radiative heat transfer coefficient U_{lir} to U_{cs}-value (see Fig. 5.22(a)). With free convection in air (low U_{cv}) and moderate temperatures that produce small radiative fluxes (low U_{lir}), the radiative transfer is comparable to convection. This behaviour of free convection and radiation at the boundary surface was similarly noted by Howell et al. (2011).

For the U_{cs}-value measurement, the temperature difference between the interior part of the developed system (big thermal box) and the outside air was maintained at 15 K. As a result, the variation in the temperature difference between the exterior cover surface and the air was slight. This means that the scattering of the U_{lir} to U_{cs}-value ratio can be attributed to the cloudiness behaviour. At night, the lack of cloud cover means that any energy from the sun absorbed by the ground during the day is radiated back to space and thus bringing cold weather. It therefore implies that the proportion of heat losses through radiation during cold, clear-sky nights will be high. This corroborates the findings by Liu and Harris (2013) on the external surface of a low-rise building.

The U_{cs}-value, U_{lir} and U_{cv} were strongly affected by wind speed (Ronoh et al., 2015). As expected, the ratio of U_{cv} to U_{cs}-value increased with an increase in wind speed (Liu and Harris, 2013; Suhardiyanto and Romdhonah, 2008). Even at wind speed of 0 m s^{-1} (still air), $U_{cv} \neq 0$ W m^{-2} K^{-1} and thus revealing that the convection heat transfer at the exterior cover surface was not forced. Apart from the free convection due to temperature difference, forced convection took a substantial part of the exchange. This agrees well with observations noted by Suhardiyanto and Romdhonah (2008) and Al-Mahdouri et al. (2014) that, in most cases, the mixed convection (free and forced convection) exists at the outside cover. The decrease in U_{lir} to U_{cs}-value ratio at high wind speeds was less marked due to the convection which takes over as the dominant mode of heat loss. A strong interaction between U_{lir} and U_{cv} as a function of the wind speed was generally observed. The results highlight the importance of measurement of local wind speed rather than the bulk velocity at the meteorological site (Liu et al., 2015).

6.3.2 U_{cs}-values of roofs and walls

The results from the four miniaturized thermal boxes indicated that the roof was mostly affected by convection due to its exposure compared to the wall and hence the variation in the surface-to-air temperature difference ΔT_{s-a}. Depending on the surface exposure, and thus the view factors, the air adjacent to the surface drains heat from it by conductive and convective heat transport mechanisms. The two transport phenomena are mostly lumped together in the form of convective heat transfer. Owing to the fact that the roof has a larger sky view factor F_{sky} than the vertical wall, low ΔT_{s-a} for the roof and high ΔT_{s-a} for the wall were expected. Due to the surface orientation, the wind effect favoured the dominance of mixed convection (free and forced convection) at the vertical walls unlike the movement of wind (forced convection) over the roofs. The free convection due to high ΔT_{s-a} (Liu et al., 2015) at the walls can increase the U_{cs}-value compared to the roofs. This can be further explained by the surface-to-wind angle (Emmel et al., 2007) which is higher for vertical walls than for the roofs. Moreover, the surface-to-wind angle dependency becomes even more important when the windward walls are considered (Emmel et al., 2007).

According to Howell et al. (2011), the walls are unequally heated and thus an asymmetric free convection velocity distribution develops. In this way, the radiative exchange tends to equalize the convective heat transfer at the wall surfaces and this leads to an improved U_{cs}-value. This then implies that the U_{cs}-value is increased as a result of the convective heat transfer which increases with a rise in the surface inclination (Antretter et al., 2008). Based on the temperature regulation in the thermal boxes (inside temperature set to only 8 K higher than the air temperature), this convective effect on the roof and the wall surfaces did not solely impact on the energy consumption (Liu et al., 2015). It was, however, noticed that the net radiation loss (negative net radiation) was higher at the roofs than at the walls especially on clear-sky nights. Under these clear-sky conditions, the roofs lost about 5 W m^{-2} to 10 W m^{-2} more than the walls. This implies that high energy was required to maintain the set-point temperature of 8 K for the exposed roofs. Based on these findings, the strong interactions of the radiative and the convective exchanges at the exterior surfaces are evident and the two heat transfer mechanisms jointly influence the U_{cs}-value.

Heat transfer via conduction, convection and radiation contributes to the U_{cs}-value of the cover material when used as a roof or a wall covering (Basak et al., 2015; Dimitriadou and Shea, 2012). In addition to the heat loss due to air leakages, this phenomenon was similarly noticed from this work. The U_{cs}-values from the big south-facing thermal box were in agreement with the standard values (see Fig. 5.21) as reported in the HORTEX system (Rath, 1992). This was notably the case for a single float glass-covered surface, with an average U_{cs}-value of 7.56 W m^{-2} K^{-1} at a wind speed of 4 m s^{-1}. The corrected values took into consideration the air leakages from the thermal box (approximately 1 h^{-1} air exchange rate) and the errors related to temperature measurement. Efforts have been put in place to comprehensively address the challenges related to the surface temperature measurement (Langner and Rath, 2015) in order to enhance a precise computation of the U_{cs}-value.

6.4 Practical Usage of the Corrected Roof and Wall U_{cs}-values

With a wind speed of about 1 m s^{-1} (calm condition), the convection gains are low compared to the radiation losses. In that case, the cloudiness plays an important role in influencing the U_{cs}-value (see Fig. 5.23). The U_{cs}-value is generally higher on clear-sky conditions (0-2 octas) than on cloudy skies (6-8 octas). However, as wind speed increases to 4 m s^{-1}, the same effect of clouds is exhibited but the U_{cs}-values are higher than at low wind speeds. This clearly shows that the radiant mechanism when the sky is clouded over is different from a clear-sky condition. Overall, the surfaces of cloudy skies do not encourage more radiative losses (McMullan, 2012) from the external greenhouse surfaces. At a wind speed of 4 m s^{-1} and a mean cloudiness of 4 octas (i.e. cloudiness factor C = 0.5), the calculated area-weighted U_{cs}-value of an entire Venlo greenhouse was 7.57 W m^{-2} K^{-1} (see Eqs. (5.2) and (5.3)). This value was based on a ground area of 10000 m^2 whereby the roof and the walls constitute about 73 % and 27 % of the total greenhouse surface area, respectively. This further confirms the fact that the exposed roof is a major part of heat loss in greenhouses (Algarni and Nutter, 2015; Castilla, 2013; Sanford, 2011). In fact, unlike the wall, the roof is exposed to several environmental factors such as dust, rain, sunlight, snow and wind, all of which contribute to variations in the roof's thermal properties. Hence, an improvement of the roof thermal performance results in a major reduction in the greenhouse energy consumption (Algarni and Nutter, 2015).

The conventional wind-corrected U_{cs}-values ($U_{cs,v}$) for greenhouses (Rath, 1992) can be transformed into separate values for roofs and walls. This is possible by taking into account the outdoor conditions such as wind speed and cloudiness. Hence, a correction factor CF (see Eq. (5.4)) was incorporated in the new corrected models ($U_{cs,n}$). In principle, the CF should have a full effect on the model (i.e. CF is 1) for a standardized U_{cs}-value of 7.56 W m^{-2} K^{-1} at a wind speed of 4 m s^{-1}. However, at a lower U_{cs}-value of approximately 4 W m^{-2} K^{-1}, the CF is halved. This implies that the model effect is reduced (thus low CF) for low U_{cs}-values and this characterizes a well-insulated greenhouse. This is true since the glass surface temperature is close to the outside air temperature. The multiplicative CF effect (with no offset) was found to be appropriate and this is in agreement with the previous correction to wind speed (Rath, 1992). Due to the cloudiness C and wind speed v corrections, the new corrected $U_{cs,n}$ models for roofs and walls (see Eqs. (5.8) and (5.9))

are therefore applicable in practical situations. These key parameters (C and v) are important since they influence the radiative and convective heat transfer interaction at the greenhouse surfaces. Initially, the coupled effect of wind and cloud variables was integrated in the multiple linear regression models. However, based on the model coefficients and statistics, this coupled effect ($C \cdot v$) seemed to have a relatively less impact on the corrected models compared to the individual variables.

The calculated average U_{cs}-values (with the new corrected models) compared well with the old wind-corrected U_{cs}-values ($R^2 = 0.995$) from the HORTEX system (Rath, 1992), with the best comparison being noted at a mean cloudiness factor C of 0.385. Despite the prevalent variations in cloudiness conditions, the previous measurements in the same study location (Rath, 1992) were done at approximately 3 octas. The new corrected models ($U_{cs,n}$) for both roofs and walls have the standard greenhouse U_{cs}-value ($U_{cs,st}$), the cloudiness factor C and the wind speed v as the independent variables. In the multilinear roof and wall $U_{cs,n}$ models, $U_{cs,st}$ and $U_{cs,st} \cdot v$ had the highest effect of about 45 % and 38 %, respectively. The impact of C in the $U_{cs,n}$ models was relatively minimal. In each of the models, the influence of $U_{cs,st} \cdot C$ and $U_{cs,st} \cdot C \cdot v$ amounted to < 5.2 % and < 2 %, respectively. However, all individual model variables ($U_{cs,st}$, C and v) jointly play an important role in the calculation of the new corrected U_{cs}-values both for roofs and walls.

A quadratic term for the wind speed v in the $U_{cs,n}$ models is in agreement with the physical argumentation. The Newtonian approximation of kinetic energy at low speeds, for instance, has the quadratic effect of v (i.e. $\frac{1}{2} \cdot m \cdot v^2$) with m being the object's mass and v as the wind speed (Katz, 2016). Hence, the quadratic term ($U_{cs,st} \cdot v^2$) in the new multilinear $U_{cs,n}$ models is sufficient for both surface inclinations (roof and wall). For all the terms in the new models, the common factor is the $U_{cs,st}$ which expresses the extent of glass insulation. The standard U_{cs}-value (i.e. $U_{cs,st}$) of 7.56 W m^{-2} K^{-1} is generally applicable for greenhouses covered with a single float glass and at an average wind speed of 4 m s^{-1} (Rath, 1992; von Zabeltitz, 1986). Overall, the new corrected $U_{cs,n}$ models from this study are useful in the accurate calculation of distinct roof and wall U_{cs}-values under all wind and sky conditions.

6.5 General

The vertical positioning of a net radiometer from the surface affects the view angle of the instrument. From the preliminary tests, an appropriate vertical height of the five net radiometers from the big south-facing thermal box was found to be 0.2 m. With this vertical height and the cover surface dimensions, a view angle of about 150° was attained. This is within the field of view of the net radiometer (Kipp & Zonen, 2009). As noted by Anthoni et al. (2000), view angles of at least 86° are expected to contribute to less than 0.5 % of the net radiation. On the other hand, the net radiometer (240-8110 type) in each of the four miniaturized thermal boxes was positioned at a vertical height of 0.07 m above the cover surface. This was necessary to guarantee the radiometer field of view since the surface design was scaled down from that of the big thermal box. In addition, this vertical height enabled closer capturing of the upwelling radiation from the surface. In analysing the exchange of radiant energy between surfaces, their emission, reflection and absorption characteristics are very necessary (Sparrow and Cess, 1967). This implies that for a glass-covered greenhouse surface, the individual properties of the glass and the glazing bars should be known. The condition of the surface is affected by the physical and chemical contamination which can change the surface properties (e.g. emission, reflection and absorption). These effects should be taken into account when modelling the thermal radiation exchange.

Infrared thermography helps in the determination of the thermal status of building surfaces such as in greenhouses (Lehmann et al., 2013). The surface temperature and the heat distribution at the glass-covered greenhouse surface was adequately assessed using the infrared thermography technique. Generally, the application of thermal imaging is gaining popularity in agriculture in recent years. This is due to the major advantages of the thermal imaging such as non-contact, non-invasive, and rapid technique which could be used for online applications. Since thermal imaging cameras look at heat and not light, they can be used in total darkness (Vadivambal and Jayas, 2011). In the recent past, the development of infrared imaging together with the issue of energy consumption of buildings has led to an enhancement in the application of infrared thermography (Lehmann et al., 2013).

7 CONCLUSIONS AND OUTLOOK

7.1 Conclusions

7.1.1 Surface inclination and orientation effects

In radiative exchange processes at the greenhouse surfaces, the usual factors of interest are local temperatures and energy fluxes. The results indicated that the sky-oriented roofs cooled more than the walls. The exposed roofs thus led to more heat loss to the sky than the walls especially under a clear-sky condition. This implies that the configuration of the surface contributed to the variation in the net radiation loss. The clear-sky acts as a better absorber of radiant heat than a cloudy sky. This effect causes the surface temperatures of the roof to fall significantly especially at night. Due to the nighttime clear-sky radiation, the roofs therefore suffer from a great thermal stress compared to the walls. However, under an overcast condition, the variation in inclination angles did not show any significant changes in the net longwave radiation loss. Interestingly, there was an insignificant effect of orientation of the thermal boxes on the nighttime net radiation.

7.1.2 Modelling of thermal radiation exchange

At the greenhouse surfaces, the weighted contributions of thermal emissions from the sky, the surrounding air and the ground objects are explained by the view factors. During a clear night, the greenhouse surface loses more heat as it radiates to the very cold clear sky. On a regional scale, clouds play a critical role in the radiation balance at the surface. The findings from the present study demonstrate that the prediction models provide a more realistic understanding of the thermal radiation exchange between the greenhouse surfaces and the sky if all the required parameters can be accurately determined. The clear-sky atmospheric emissivity parameterizations that include both the near-surface water vapour pressure and the air temperature tend to outperform those consisting of only the air temperature. Under both day and night situations, the study delivers reliable results in terms of the calculation of parameters necessary for the radiation models. The parameters which have an influence on the daytime and nighttime net radiation are surface and atmospheric emissivities, surface and atmospheric temperatures, and albedo.

Generally, the simulation models help to address the challenges related to the high costs of directly measuring longwave radiation. The simulation results further allow the

estimation of the thermal exchange on any building surfaces. It is evident from the results that neglecting to consider thermal radiation (shortwave and longwave) exchange in sufficient detail can lead to serious inaccuracies in the model predictions. For the energy balance under daytime conditions, the solar irradiance on greenhouse surfaces plays a very important role and should, therefore, be accounted for precisely. The solar radiation data is readily available from most weather stations particularly for horizontal surfaces and this, together with other parameters, can be utilized in calculating the total irradiance on tilted surfaces with an acceptable accuracy. Knowledge of the thermal radiation exchange is vitally important for numerous applications in agriculture requiring surface radiation and energy balance.

7.1.3 Influence of the radiation exchange on the U_{cs}-value

The findings showed a strong interaction between the radiative and the convective heat transfers at greenhouse surfaces. The simulation results contribute to a more accurate evaluation of thermal losses. The exterior surfaces transfer heat to the outside environment both by radiation and convection. The radiative heat transfer depends on the temperature difference while the convective heat transfer increases with a rise of inclination. As wind speed increased from 0 m s^{-1} to 4 m s^{-1}, the ratio of the radiative heat transfer coefficient U_{lir} to the U_{cs}-value reduced by 41 % while the ratio of the convective heat transfer coefficient U_{cv} to the U_{cs}-value increased by 59 %. Generally, the correlations related to the interactions between the convective and radiative heat losses at the greenhouse surfaces should be integrated into the energy simulation programs.

7.1.4 Application of the new corrected roof and wall U_{cs}-values

From the results of this study, the U_{cs}-value was generally higher on clear-sky conditions than on cloudy skies. As wind speed increases from 0 m s^{-1} to 4 m s^{-1}, the convective gains lead to high U_{cs}-values. At the exterior greenhouse surfaces, the exposed roofs registered higher U_{cs}-values than the walls under different sky and wind conditions. For a ground area of 10000 m^2, an average wind speed of 4 m s^{-1} and an average cloudiness of 4 octas, the calculated area-weighted U_{cs}-value for an entire standard Venlo greenhouse was obtained as 7.57 W m^{-2} K^{-1}. The developed models for transforming the conventional wind-corrected U_{cs}-values to the distinct values for roofs and walls are generally

applicable under all wind and sky conditions. At an average wind speed of 4 m s^{-1} and a cloudiness factor of 0.385, the corrected models ensure that all average U_{cs}-values (for roof and wall surfaces) remain unchanged. The multilinear models of the new corrected U_{cs}-values ($U_{cs,n}$) depend on the standard greenhouse U_{cs}-value at 4 m s^{-1}, the cloudiness factor and the wind speed. Generally, the $U_{cs,n}$ models for both surface inclinations (roofs and walls) adjusted with the appropriate correction factors are useful in the comprehensive calculation of greenhouse heat demands.

7.2 Outlook

A proper understanding of interrelationships between the critical climatic factors and the behaviour of the thermal radiation exchange is very essential in sustainable commercial agricultural production. There are a lot of interacting phenomena in the atmosphere which have to be taken into account to make precise predictions while modelling the thermal radiation exchange. More emphasis on any other techniques which can improve the cloudiness prediction needs to be explored. The data from other locations can also be useful in validating the developed radiation models. In particular, it is believed that the improved polynomial correlation relating the diffuse fraction and the clearness index can be efficiently used for the computation of the total solar irradiance in other parts of the world. Due to the difference in spatial and temporal resolution, the correlation can be assessed as to whether or not it is site-specific or generally applicable. Additionally, it would be better to incorporate a cloudiness factor instead of the sky clearness index for the solar radiation estimation.

It is important to consider the impact of wind speed specifically for the windward greenhouse surfaces in energy simulations. In this case, the data is distinguished from those of leeward surfaces and the sensitivity to the variation in wind direction can be checked. This becomes more important in uncertainty quantification as a result of variations in the surface orientation. Also important is to consider the fact that other surface inclination angles between 0° and 90° lead to the calculation of more view factors which can be related in detail with the U_{cs}-value. This information is useful in understanding the effects brought about by the inclined greenhouse surfaces on heating energy and thus on heat losses.

REFERENCES

Abdel-Ghany, A.M. and Kozai, T. (2006). On the determination of the overall heat transmission coefficient and soil heat flux for a fog cooled, naturally ventilated greenhouse: Analysis of radiation and convection heat transfer. *Energy Conversion and Management*, 47(15), 2612-2628.

Abdullah, F.S. and Ali, F.A. (2012). Estimation of the effects of each site factors, time factors, and optical factors on absorbed solar radiation value that is incident on a flat-plate solar collector. *Journal of Theoretical and Applied Information Technology*, 41(2), 122-133. ISSN: 1992-8645.

Adelard, L., Pignolet-Tardan, F., Mara, T., Lauret, P., Garde, F. and Boyer, H. (1998). Sky temperature modelisation and applications in building simulation. *Renewable Energy*, 15(1), 418-430.

Ajwang, P. (2005). Prediction of the effects of insect-proof screens on the climate in naturally ventilated greenhouses in the humid tropics. PhD Thesis, *Gartenbautechnische Informationen*, Heft 63, Gottfried Wilhelm Leibniz Universität Hannover, Germany.

Al-Ajlan, S.A., Al-Faris, H. and Khonkar, H. (2003). A simulation modeling for optimization of flat plate collector design in Riyadh, Saudi Arabia. *Renewable Energy*, 28(9), 1325-1339.

Algarni, S. and Nutter, D. (2015). Influence of dust accumulation on building roof thermal performance and radiant heat gain in hot-dry climates. *Energy and Buildings*, 104, 181-190.

Al-Mahdouri, A., Gonome, H., Okajima, J. and Maruyama, S. (2014). Theoretical and experimental study of solar thermal performance of different greenhouse cladding materials. *Solar Energy*, 107, 314-327.

Ambach, W. (1974). The influence of cloudiness on the net radiation balance of a snow surface with high albedo. *Journal of Glaciology*, 13(67), 73-84.

Anthoni, P.M., Law, B.E., Unsworth, M.H. and Vong, R.J. (2000). Variation of net radiation over heterogeneous surfaces: Measurements and simulation in a juniper-sagebrush ecosystem. *Agricultural and Forest Meteorology*, 102(4), 275-286.

Antretter, F., Haupt, W. and Holm, A. (2008). Thermal transfer through membrane cushions analyzed by computational fluid dynamics. *8th Nordic Symposium on Building Physics in the Nordic Countries*. Copenhagen, Lyngby, 1, 347-354.

Araújo, A.L., da Silva, B.B. and Braga, C.C. (2012). Simplified modeling of downwelling long-wave radiation over Brazilian semi-arid under irrigation conditions. *Brazilian Journal of Geophysics*, 30(2), 137-145.

Arora, R.C. (2010). *Refrigeration and air conditioning*. PHI Learning Private Limited, New Delhi, India.

Ayoola, M.A., Sunmonu, L.A., Bashiru, M.I. and Jegede, O.O. (2014). Measurements of net all-wave radiation at a tropical location, Ile-Ife, Nigeria. *Atmósfera*, 27(3), 305-315.

Bahrami, M. (2005). *Radiation heat transfer*. Chapter 12, E&CE 309, Spring 2005. Available at: http://www.mhtl.uwaterloo.ca. Retrieved on 13th March 2013.

Bailey, B.J., Montero, J.I., Perez-Parra, J.J., Robertson, A.P., Baeza, E. and Kamaruddin, R. (2003). Airflow resistance of greenhouse ventilators with and without insect screens. *Biosystems Engineering*, 86(2), 217-229.

Baille, A., Lopez, J.C., Bonachela, S., Gonzalez-Real, M.M. and Montero, J.I. (2006). Night energy balance in a heated low-cost plastic greenhouse. *Agricultural and Forest Meteorology*, 137(1-2), 107-118.

Baille, A., Gonzalez-Real, M.M., Gasquez, J.C. Lopez, J.C., Perez-Parra, J.J. and Rodriquez, E. (2006). Effects of different cooling strategies on the transpiration rate and conductance of greenhouse sweet pepper crops. *Acta Horticulturae*, 719, 463-470.

Basak, C.K., Sarkar, G. and Neogi, S. (2015). Performance evaluation of material and comparison of different temperature control strategies of a guarded hot box *U*-value test facility. *Energy and Buildings*, 105, 258-262.

Bayler G.M., Aune, R.M. and Raymond, W.H. (2000): NWP cloud initialization using GOES sounder data and improved modeling of nonprecipitating clouds. *Monthly Weather Review*, 128(11), 3911-3920.

Berdahl, P. and Martin, M. (1984). Emissivity of clear skies. *Solar Energy*, 32(5), 663-664.

Berroug, F., Lakhal, E.K., El Omari, M., Faraji, M. and El Qarnia, H. (2011). Thermal performance of a greenhouse with a phase change material north wall. *Energy and Buildings*, 43(11), 3027-3035.

Bi, J., Huang, J., Fu, Q., Ge, J., Shi, J., Zhou, T. and Zhang, W. (2013). Field measurement of clear-sky solar irradiance in Badain Jaran Desert of Northwestern China. *Journal of Quantitative Spectroscopy and Radiative Transfer*, 122, 194-207.

Bolsenga, S.J. (1979). *Solar altitude effects on ice albedo*. NOAA Technical Memorandum, ERL GLERL-25. Great Lakes Environmental Research Laboratory, Ann Arbor, Michigan, USA, pp. 1-5.

Bot, G.P.A. and van de Braak, N.J. (1995). Physics of greenhouse climate, In: Bakker, J.C., Bot, G.P.A., Challa, H. and van de Braak, N.J. (eds). *Greenhouse climate control: An integrated approach*. Wageningen Pers, Wageningen, The Netherlands, pp. 125-130.

Bot, G.P.A. (1983). *Greenhouse climate: from physical processes to a dynamic model*. PhD Thesis, Agricultural University of Wageningen, The Netherlands.

Briassoulis, D., Waaijenberg, D., Gratraud, J. and von Elsner, B. (1997a). Mechanical properties of covering materials for greenhouses. Part 1: General overview. *Journal of Agricultural Engineering Research*, 67, 81-96.

Briassoulis, D., Waaijenberg, D., Gratraud, J. and von Elsner, B. (1997b). Mechanical properties of covering materials for greenhouses. Part 2: Quality assessment. *Journal of Agricultural Engineering Research*, 67, 171-217.

Brutsaert, W. (1975). On a derivable formula for long-wave radiation from clear skies. *Water Resources Research*, 11(5), 742-744.

Burari, F.W. and Sambo, A.S (2001). Model for the prediction of global solar radiation for Bauchi using meteorological data. *Nigerian Journal of Renewable Energy*, 9(1&2), 30-33.

Burke, M.W. (1996). *Image acquisition: Handbook of machine vision engineering*. 1st Edition, Chapman & Hall, London, UK, pp. 61-63.

Campbell, G.S. and Norman, J.M. (1998). *An introduction to environmental biophysics*. 2nd Edition. Springer, New York, NY, USA.

Canada Plan Service. *Greenhouse heating requirements*. Leaflet plan M-6701. Available at: http://www.cps.gov.on.ca/english/plans/E6000/6701/M-6701L.pdf. Accessed on 1st July 2012.

Castilla, N. (2013). *Greenhouse technology and management*. 2nd Edition, Wallingford, Oxfordshire, UK, pp. 115-117.

Cengel, Y.A. (2007). *Heat and mass transfer: A practical approach.* 3rd Edition, Mc-Graw Hill, New York.

Chandra, P. (1982). Thermal radiation exchange in a greenhouse with a transmitting cover. *Journal of Agricultural Engineering Research*, 27(3), 261-265.

Chapman, L., Thornes, J.E. and Bradley, A.V. (2001). Modelling of road surface temperature from a geographical parameter database. Part 1: Statistical. *Meteorological Applications*, 8(4), 409-419.

Chen, B., Clark, D., Maloney, J., Mei, W.N. and Kasher, J. (1995). Measurements of night sky emissivity in determining radiant cooling from cool storage roofs and roofs ponds. In: *Proceedings of American Solar Energy Society*. Annual Meeting, Minneapolis, USA.

Cheng, C.H. and Nnadi, F. (2014). Predicting downward longwave radiation for various land use in all-sky condition: Northeast Florida. *Advances in Meteorology*, 1-12.

Choi, M. (2013). Parameterizing daytime downward longwave radiation in two Korean regional flux monitoring network sites. *Journal of Hydrology*, 476(1), 257-264.

Choi, M., Jacobs, J.M. and Kustas, W.P. (2008). Assessment of clear and cloudy sky parameterizations for daily downwelling longwave radiation over different land surfaces in Florida, USA. *Geophysical Research Letters*, 35(L20402), 1-6.

Crawford, T.M. and Duchon, C.E. (1999). An improved parameterization for estimating effective atmospheric emissivity for use in calculating daytime downwelling longwave radiation. *Journal of Applied Meteorology*, 38(4), 474-480.

DeVisser, M.H. (2010). Identifying sensitivity thresholds in environmental models: When does a model become insensitive to change? *ASPRS 2010 Annual Conference*, San Diego, California, USA.

Dimitriadou, E.A. and Shea, A. (2012). Experimental assessment and thermal characterization of ETFE foil. *Athens: ATINER'S Conference Paper Series*, No: CON2012-0145, Athens, Greece.

DIN 11535-2 (1994). *Gewächshäuser; Stahl- und Aluminiumbauart 12,80 m breit mit dem Rastermaß von 3,065 m in Längsrichtung* (Greenhouses; steel and aluminium construction 12.80 m in width with a longitudinal grid dimension of 3.065 m). DIN, Beuth Verlag GmbH, Berlin, Germany.

Dingman, S.L. (2009). *Fluvial hydraulics*. Oxford University Press, New York, USA, pp. 105-107.

Doukas, D. and Payne, C.C. (2007). Effects of UV-blocking films on the dispersal behaviour of *Encarsia Formosa* (Hymenoptera: Aphelinidae). *Journal of Economic Entomology*, 100(1), 110-116.

Dos Santos, C.A.C., Da Silva, B.B., Rao, T.V.R., Satyamurty, P. and Manzi, A.O. (2011). Downward longwave radiation estimates for clear-sky conditions over northeast Brazil. *Revista Brasileira de Meteorologia*, 26(3), 443-450.

Duarte, H.F., Dias, N.L. and Maggiotto, S.R. (2006). Assessing daytime downward longwave radiation estimates for clear and cloudy skies in southern Brazil. *Agricultural and Forest Meteorology*, 139(3-4), 171-181.

Duffie, J.A. and Beckman, W.A. (1991). *Solar engineering of thermal processes*. John Wiley & Sons, Inc., New York, USA.

Edwards, D.K. (1981). *Radiation heat transfer notes.* Hemisphere Publishing Corporation, Washington, DC.

Eliasson, I. (1996). Urban nocturnal temperatures, street geometry and land use. *Atmospheric Environment*, 30(3), 379-392.

El-Sebaii, A.A., Al-Hazmi, F.S., Al-Ghamdi, A.A. and Yaghmour, S.J. (2010). Global, direct and diffuse solar radiation on horizontal and tilted surfaces in Jeddah, Saudi Arabia. *Applied Energy*, 87(2), 568-576.

Emmel, M.G., Abadie, M.O. and Mendes, N. (2007). New external convective heat transfer coefficient correlations for isolated low-rise buildings. *Energy and Buildings*, 39(3), 335-342.

EnergyPlus 8.0 (2013). *Engineering reference: Outside surface heat balance*. Available at: http://bigladdersoftware.com/epx/docs/8-0/engineering-reference. Accessed on 20th September 2013.

Evins, R., Dorer, V. and Carmeliet, J. (2014). Simulating external longwave radiation exchange for buildings. *Energy and Buildings*, 75, 472-482.

Evseev, E.G. and Kudish, A.I. (2009). The assessment of different models to predict the global solar radiation on a surface tilted to the south. *Solar Energy*, 83(2), 377-388.

Ezekoye, B.A. and Enebe, O.M. (2006). Development and performance evaluation of modified integrated passive solar grain dryer. *The Pacific Journal of Science and Technology*, 7(2), 185-190.

FAO (1998). *Crop evapotranspiration – Guidelines for computing crop water requirements*. Chapter 3: Meteorological data. Available at: http://www.fao.org. Accessed on 15th November 2013.

Ferreira, M.J., de Oliveira, A.P., Soares, J., Codato, G., Bárbaro, E.W. and Escobedo, J.F. (2012). Radiation balance at the surface in the city of São Paulo, Brazil: Diurnal and seasonal variations. *Theoretical and Applied Climatology*, 107(1-2), 229-246.

Flerchinger, G.N., Xaio, W., Marks, D., Sauer, T.J. and Yu, Q. (2009). Comparison of algorithms for incoming atmospheric long-wave radiation. *Water Resources Research*, 45(W03423), 1-13.

Fluke (2009). *Emissivity values of common materials*. Fluke Corporation, Everett, WA, USA. Available at: http://www.fluke.com. Accessed on 14th April 2013.

Formetta, G., Rigon, R. Chávez, J.L. and David, O. (2013). Modeling shortwave solar radiation using the JGrass-NewAge system. *Geoscientific Model Development*, 6(4), 915-928.

Foussier, P. (2006). *From product description to cost: A practical approach*. Volume 2: Building a specific model. Springer-Verlag, London, UK, pp. 133-137.

Garg, H.P. and Prakash, J. (2000). *Solar energy: Fundamentals and applications*. 1st Revised Ed. Tata McGraw-Hill Publishers, New Delhi, India.

Garzoli, K.V. (1984). *Solar greenhouse design and performance*. PhD Thesis, Department of Civil Engineering, University of Melbourne, Australia.

Garzoli, K.V. and Blackwell, J. (1981). An analysis of the nocturnal heat loss from a single skin plastic greenhouse. *Journal of Agricultural Engineering Research*, 26(3), 203-214.

Geoola, F., Kashti, Y., Levi, A. and Brickman, R. (2009). A study of the overall heat transfer coefficient of greenhouse cladding materials with thermal screens using the hot box method. *Polymer Testing*, 28(5), 470-474.

German Weather Service (Deutscher Wetterdienst, DWD). *Web weather request and distribution system (WebWerdis)*. Available at: http://www.dwd.de. Accessed on 9th July 2013.

Giacomelli, G.A. (1999). *Greenhouse glazings: Alternatives under the sun*. Department of Bioresource Engineering, Cook College, Rutgers University, New Brunswick, New Jersey.

Giacomelli, G.A. and Roberts, W.J. (1993). Greenhouse covering systems. *HortTechnology*, 3(1), 50-58.

Gonzalez, C. (2015). What's the difference between conduction, convection, and radiation? Available at: http://machinedesign.com/learning-resources. Accessed on 20th December 2015.

Goswami, D.Y., Kreith, F. and Kreider, J.F. (2000). *Principles of Solar Engineering*. Taylor and Francis, UK.

Gubler, S., Gruber, S. and Purves, R.S. (2012). Uncertainties of parameterized near-surface downward longwave and clear-sky direct radiation. *Atmospheric Chemistry and Physics Discussion*, 12(1), 3357-3407.

Guest, P.S. (1998). Surface longwave radiation conditions in the eastern Weddell Sea during winter. *Journal of Geophysical Research*, 103(C13), 30761-30771.

Gulin, M., Vašak, M. and Baotić, M. (2013). Estimation of the global solar irradiance on tilted surfaces. *17th International Conference on Electrical Drives and Power Electronics (EDPE 2013)*, 2nd–4th October 2013, Dubrovnik, Croatia.

Gupta, M.J. and Chandra, P. (2002). Effect of greenhouse design parameters on conservation of energy for greenhouse environmental control. *Energy*, 27(8), 777-794.

HALCON Version 11.0.3 (2012). *HALCON/HDevelop Reference Manual*. MVTec Software GmbH, München, Germany.

Hamby, D.M. (1994). A review of techniques for parameter sensitivity analysis of environmental models. *Environmental Monitoring and Assessment*, 32(2), 135-154.

Hanan, J.J. (1997). *Greenhouses: Advanced technology for protected horticulture*. Chapter 4: Temperature. CRC Press, Boca Raton, Florida, USA, pp. 191-199.

Hay, J.E. (1979). Calculation of monthly mean solar radiation for horizontal and inclined surfaces. *Solar Energy*, 23(4), 301-307.

Hemming, S., van der Braak, N., Dueck, T., Jongschaap, R. and Marissen, N. (2006). Filtering natural light by the greenhouse covering using model simulations – more production and better plant quality by diffuse light. *Acta Horticulturae*, 711, 105-110.

Holman, J.P. (1986). *Heat Transfer*. 6th Edition, McGraw-Hill Book Company, Singapore, pp. 207-259.

Howard, R. and Stull, R. (2013). Modeling the downwelling longwave radiation over a groomed ski run under clear skies. *Journal of Applied Meteorology and Climatology*, 52(7), 1540-1553.

Howell, J.R., Siegel, R. and Mengüc, M.P. (2011). *Thermal radiation heat transfer*, 5th Edition, CRC Press, Boca Raton, New York, 987 pp.

Howell, J.R. (1982). *A catalog of radiation configuration factors*, McGraw-Hill, New York.

Ibrahim, A., El-Sebaii, A.A., Ramadan, M.R.I. and El-Broullesy, S.M. (2011). Estimation of solar irradiance on inclined surfaces facing south in Tanta, Egypt. *International Journal of Renewable Energy Research*, 1(1), 18-25.

Idso, S.B. (1981). A set of equations for full spectrum and 8 to 14 µm and 10.5 to 12.5 µm thermal radiation from cloudless skies. *Water Resources Research*, 17(2), 295-304.

Idso, S.B. and Jackson, R.D. (1969). Thermal radiation from the atmosphere. *Journal of Geophysical Research*, 74(23), 5397-5403.

IESNA (2000). *The IESNA lighting handbook: Reference and application*. Illuminating Engineering, 9th Edition. New York, USA.

InfraTec (2006). *IRBIS® plus: Thermal image processing software*. User's Manual, InfraTec GmbH, Dresden, Germany.

Institute of Meteorology and Climatology (Institut für Meteorologie und Klimatologie: IMUK). *Measurement data of Hannover Herrenhausen*. Available at: http://www.muk.uni-hannover.de/wetter/datenarchiv/imuk/herrenhausen/2014. Accessed on 13th March 2014.

Iqbal, M. (1983). *An introduction to solar radiation*. Academic Press, Toronto, Canada, 390 pp.

Iziomon, M.G., Mayer, H. and Matzarakis, A. (2003). Downward atmospheric longwave irradiance under clear and cloudy skies: Measurement and parameterization. *Journal of Atmospheric and Solar-Terrestrial Physics*, 65(10), 1107-1116.

Jacobs, J.M., Anderson, M.C., Friess, L.C. and Diak, G.R. (2004). Solar radiation, longwave radiation and emergent wetland evapotranspiration estimates from satellite data in Florida, USA. *Hydrological Sciences Journal*, 49(3), 461-476.

Jacovides, C.P., Tymvios, F.S., Assimakopoulos, V.D. and Kaltsounides, N.A. (2006). Comparative study of various correlations in estimating hourly diffuse fraction of global solar radiation. *Renewable Energy*, 31(15), 2492-2504.

Jawarneh, A.M., Al-Tarawneh, M., Ababneh, M.K. and Tlilan, H. (2012). Solar energy availability on horizontal and tilted surfaces: A case study. *International Review of Mechanical Engineering*, 6(4), 901-917.

Jolliet, O., Danloy, L., Gay, J.-B., Munday, G.L. and Reist, A. (1991). HORTICERN: An improved static model for predicting the energy consumption of a greenhouse. *Agricultural and Forest Meteorology*, 55(3-4), 265-294.

Jones, H.G., Archer, N., Rotenberg, E. and Casa, R. (2003). Radiation measurement for plant ecophysiology. *Journal of Experimental Botany*, 54(384), 879-889.

Jones, H.G. (2014). *Plants and microclimate: A quantitative approach to environmental plant physiology*. 3rd Edition, Cambridge University Press, Cambridge, UK.

Kacira, M. (2012). *Greenhouse structures and design*. UA-CEAC Greenhouse Crop Production and Engineering Design Short Course, 10th April 2012. The University of Arizona, Tucson, Arizona, USA.

Kanthak, D. (1970). Der Einfluß von Heizungssystemen mit unterschiedlichem Strahlungsanteil auf das Klima und den Wärmeverbrauch von Hallenbauten mit großem Glasanteil, speziell von Gewächshäusern. In: *Fortschrittsberichte der VDI-Zeitschrift*, Reihe 6, 28.

Katz, D.M. (2016). *Physics for scientists and engineers: Foundations and connections*. Advance Edition, Volume 2. Cengage Learning, Boston, USA, pp. 1293-1294.

Katsaros, K. and Buettner, K.J.K. (1969). Influence of rainfall on temperature and salinity of the ocean surface. *Journal of Applied Meteorology*, 8(1), 15-18.

Kehrer, M. and Schmidt, T. (2008). Radiation effects on exterior surfaces. In: *Proceedings of 8th Symposium on Building Physics in the Nordic Countries*, 2008, DTU, Copenhagen, Denmark, 1, 207-212.

Kessler, A. and Jaeger, L. (2003). Analysis of long time series of long-wave radiation fluxes above a pine forest. *Theoretical and Applied Climatology*, 74(3-4), 179-189.

Key, E.L. and Minnett, P.J. (2004). Estimating polynya cloudiness. *Gayana (Concepc.) TIProc Concepciòn*, 68(2), 311-316. ISSN: 0717-652X.

Kimball, B.A., Idso, S.B. and Aase, J.K. (1982). A model of thermal radiation from cloudy and overcast skies. *Water Resources Research*, 18(4), 931-936.

Kipp & Zonen (2009). *Instruction manual, CNR 4 net radiometer*. Manual version 1107. Delft, The Netherlands.

Kittas, C. (1986). Greenhouse cover conductances. *Boundary-Layer Meteorology*, 36, 39-54.

Kosmos, S.R., Riskowski, G.L. and Christianson, L.L. (1993). Force and static pressure resulting from airflow through screens. *Transactions of the ASAE*, 36(5), 1467-1472.

Kruk, N.S., Vendrame, I.F., Rocha, H.R., Chou, S.C. and Cabral, O. (2010). Downward longwave radiation estimates for clear and all-sky conditions in the Sertãozinho region of São Paulo, Brazil. *Theoretical and Applied Climatology*, 99(1-2), 115-123.

Kumar, K.S., Tiwari, K.N. and Jha, M.K. (2009). Design technology for greenhouse cooling in tropical and subtropical regions. *Energy and Buildings*, 41(12), 1269-1275.

Kumar, P. and Poehling, M. (2006). UV-blocking plastic films and nets influence vectors and virus transmission on greenhouse tomatoes in the humid tropics. *Journal of Environmental Entomology*, 35(4), 1069-1082.

Langner, F. and Rath, T. (2015). Erfassung der Glastemperatur bei Gewächshäusern. *DGG & BHGL 50th Horticultural Science Conference and International WeGa Symposium*. Freising-Weihenstephan, Germany, 24th–28th February 2015. BHGL Tagungsband 31, ISSN 1613-088X, p. 122.

Langner, F. and Rath, T. (2014). Entwicklung eines differenzierten Widerstandsmodells zur Erstellung vergleichbarer Energiebedarfsberechnung von Gewächshäusern. *DGG & BHGL 49th Horticultural Science Conference*, Dresden, Germany, 5th–8th March 2014. BHGL Tagungsband 30, ISSN 1613-088X, p. 27.

Lehmann, B., Wakili, K.G., Frank, Th. Collado, B.V. and Tanner, Ch. (2013). Effects of individual climatic parameters on the infrared thermography of buildings. *Applied Energy*, 110, 29-43.

Lenhart, T., Eckhardt, K., Fohrer, N. and Frede, H.-G. (2002). Comparison of two different approaches of sensitivity analysis. *Physics and Chemistry of the Earth*, 27(9-10), 645-654.

Li, D., Bou-Zeid, E. and Oppenheimer, M. (2014). The effectiveness of cool and green roofs as urban heat island mitigation strategies. *Environmental Research Letters*, 9(5), 1-16.

Liang, S.L. (2004). *Quantitative remote sensing of land surfaces*. John Wiley & Sons, New Jersey, USA.

Liu, J., Heidarinejad, M., Gracik, S. and Srebric, J. (2015). The impact of exterior surface convective heat transfer coefficients on the building energy consumption in urban neighborhoods with different plan area densities. *Energy and Buildings*, 86, 449-463.

Liu, Y. and Harris, D.J. (2013). Measurements of wind speed and convective coefficient on the external surface of a low-rise building. *International Journal of Ambient Energy*, 36(5), 225-234.

Liu, B.Y.H. and Jordan, R.C. (1960). The interrelationship and characteristic distribution of direct, diffuse and total solar radiation. *Solar Energy*, 4(3), 1-19.

Lonely Planet (2015). *Map of Germany*. Available at: http://www.lonelyplanet.com. Accessed on 3rd August 2015.

Long, C.N. (2005). On the estimation of clear-sky upwelling shortwave and longwave. In: *15th ARM Science Team Meeting Proceedings*, Daytona Beach, Florida, USA, 14th–18th March 2005.

Mammeri, A., Ulmet, L., Petit, C. and Mokhtari, A.M. (2015). Temperature modelling in pavements: The effect of long- and short-wave radiation. *International Journal of Pavement Engineering*, 16(3), 198-213.

Manual PN 27005-90 (1994). *Meteorological instruments: Instructions for model 27005 Gill UVW anemometer*. R. M. Young Company, Michigan, USA.

Marthews, T.R., Malhi, Y. and Iwata, H. (2012). Calculating downward longwave radiation under clear and cloudy conditions over a tropical lowland forest site: An evaluation of model schemes for hourly data. *Theoretical and Applied Climatology*, 107(3-4), 461-477.

Marty, C. and Philipona, R. (2000). The clear-sky index to separate clear-sky from cloudy-sky situations in climate research. *Geophysical Research Letters*, 27(17), 2649-2652.

Mashonjowa, E., Ronsse, F., Milford, J.R. and Pieters, J.G. (2012). Modelling the thermal performance of a naturally ventilated greenhouse in Zimbabwe using a dynamic greenhouse climate model. *Solar Energy*, 91, 381-393.

Max, J.F.J., Reisinger, G., Hofmann, T., Hinken, J., Tantau, H.-J., Ulbrich, A., Lambrecht, S., von Elsner, B. and Schurr, U. (2012). Glass-film combination: Opto-physical properties and energy saving potential of a novel greenhouse glazing system. *Energy and Buildings*, 50, 298-307.

McMullan, R. (2012). *Environmental science in building*. 7th Edition, Palgrave Macmillan, New York, USA, pp. 42-57.

Mesmoudi, K., Soudani, A., Bougoul, S. and Bournet, P.E. (2012). On the determination of the convective heat transfer coefficient at the greenhouse cover under semi air climatic conditions. In: Proceedings of the XXVIII International Horticultural Congress on Science and Horticulture for People. 22nd–27th August 2010, Lisbon, Portugal. *Acta Horticulturae*, 927, 619-626.

Mesmoudi, K., Soudani, A., Zitouni, B., Bournet, P.E. and Serir, L. (2010). Experimental study of the energy balance of unheated greenhouse under hot and arid climates: Study for the night period of winter season. *Journal of the Association of Arab Universities for Basic and Applied Sciences*, 9(1), 27-37.

Meyer, J. (2010). Nomenklatur und Definition. In: *Bericht zur Bestimmung und Bewertung des Energiebedarfs von Gewächshäusern*. KTBL-Workshop, Worms, Germany, 17th September 2008, pp. 14-22.

Miguel, A., Bilbao, J., Aguiar, R., Kambezidis, H. and Negro, E. (2001). Diffuse solar irradiation model evaluation in the north Mediterranean belt area. *Solar Energy*, 70(2), 143-153.

Millington, J., Wainwright, J., Perry, G.L., Romero-Calcerrada, R. and Malamud, B.D. (2009). Modelling Mediterranean landscape succession-disturbance dynamics: A landscape fire-succession model. *Environmental Modelling and Software*, 24(10), 1196-1208.

Minkina, W. and Dudzik, S. (2009). *Infrared thermography: Errors and uncertainties*. John Wiley & Sons Ltd, Chichester, UK.

Moene, A.F. and van Dam, J.C. (2014). *Transport in the atmosphere-vegetation-soil continuum*. Cambridge University Press, New York, USA.

Mutwiwa, U.N. (2007). Effects of different cooling methods on microclimate and plant growth in greenhouses in the tropics. PhD Thesis, *Gartenbautechnische Informationen*, Heft 66, Gottfried Wilhelm Leibniz Universität Hannover, Germany.

Nasrollahi, F. (2009). *Climate and energy responsive housing in continental climates: The suitability of passive houses for Iran's dry and cold climate*. Universitätsverlag der TU Berlin, Germany. ISBN: 9783798321441.

Naud, C.N., Chen, Y., Rangwala, I. and Miller, J.R. (2013). Sensitivity of downward longwave surface radiation to moisture and cloud changes in a high-elevation region. *Journal of Geophysical Research: Atmospheres*, 118(17), 10072-10081.

Nie, D., Demetriades-Shah, T. and Kanemasu, E.T. (1992). Surface energy fluxes on four slope sites during FIFE 1988. *Journal of Geophysical Research*, 97(D17), 18641-18649.

Nijskens, J., Deltour, J., Coutisse, S. and Nisen, A. (1984). Heat transfer through covering materials of greenhouses. *Agricultural and Forest Meteorology*, 33(2-3), 193-214.

NovaLynx (2013). *Weather monitoring instruments and systems*. Catalog, NovaLynx Corporation, California, USA.

Nunez, M., Eliasson, I. and Lindgren, J. (2000). Spatial air temperature variations of incoming longwave radiation in Göteborg, Sweden. *Theoretical and Applied Climatology*, 67(3), 181-192.

Oerke, E.-C, Lindenthal, M., Fröhling, P. and Steiner, U. (2005). Digital infrared thermography for the assessment of leaf pathogens. In: Stafford, J.V. (Ed.), *Precision agriculture '05*. Wageningen, The Netherlands: Wageningen University Press, pp. 91-98.

Offerle, B., Grimmond, C.S.B. and Oke, T.R. (2003). Parameterization of net all-wave radiation for urban areas. *Journal of Applied Meteorology*, 42(8), 1157-1173.

Oliveti, G., Arcuri, N., De Simone, M. and Bruno, R. (2012). Experimental evaluations of the building shell radiant exchange in clear sky conditions. *Solar Energy*, 86(6), 1785-1795.

Papadakis, G., Briassoulis, D., Mugnozza, G.S., Vox, G., Feuilloley, P. and Stoffers, J.A. (2000). Radiometric and thermal properties of, and testing methods for, greenhouse covering materials. *Journal of Agricultural Engineering Research*, 77(1), 7-38.

Papadakis, G., Frangoudakis, A. and Kyritsis, S. (1992). Mixed, forced and free convection heat transfer at the greenhouse cover. *Journal of Agricultural Engineering Research*, 51, 191-205.

Pedersen, C.O., Fisher, D.E. and Liesen, R.J. (1997). Development of a heat balance procedure for calculating cooling loads. *Transactions of the American Society of Heating, Refrigerating and Air Conditioning Engineers*, 103(2), 459-468.

Petty, G.W. (2006). *A first course in atmospheric radiation*. 2nd Edition, Sundog Publishing, Madison, WI, 459 pp.

Pidwirny, M. (2006). *Fundamentals of Physical Geography*. 2nd Edition, Chapter 6: Energy and matter – The nature of radiation. Available at: http://www.physicalgeography.net/fundamentals/6f.html. Accessed on 10th June 2013.

Pollet, I.V., Pieters, J.G. and Verschoore, R. (2002). Impact of water drops on the visible radiation transmittance of glazings under outside radiant conditions. *Solar Energy*, 73(5), 327-335.

Porson, A., Clark, P.A., Harman, I.N., Best, M.J. and Belcher, S.E. (2010). Implementation of a new urban energy budget scheme in the MetUM. Part I: Description and idealized simulations. *Quarterly Journal of the Royal Meteorological Society*, 136(651), 1514-1529.

Prata, A.J. (1996). A new long-wave formula for estimating downward clear-sky radiation at the surface. *Quarterly Journal of the Royal Meteorological Society*, 122(533), 1127-1151.

prEN 13031-1 (1997). *Greenhouses: Design and construction*. Part 1: Commercial production greenhouses. CEN, Brussels, Belgium (final draft of CEN/TC 284).

Honsberg, C and Bowden, S. (2012). *PVCDROM: Properties of sunlight – solar time*. Available at: http://www.pveducation.org. Accessed on 15th November 2013.

Rath, T. (1992). Einsatz wissensbasierter systeme zur modellierung und darstellung von gartenbautechnischem fachwissen am beispiel des hybriden expertensystems HORTEX. Dissertation, *Gartenbautechnische Informationen*, Heft 34, Institut für Technik in Gartenbau und Landwirtschaft, Universität Hannover, Germany.

Rizou, M. and Nnadi, F. (2007). Land use feedback on clear sky downward longwave radiation: a land use adapted model. *International Journal of Climatology*, 27(11), 1479-1496.

Ryu, Y., Kang, S., Moon, S.K. and Kim, J. (2008). Evaluation of land surface radiation balance derived from moderate resolution imaging spectroradiometer (MODIS) over complex terrain and heterogeneous landscape on clear sky days. *Agricultural and Forest Meteorology*, 148(10), 1538-1552.

Romila, C. (2012). Night radiation effect on energy performance of ventilated facades. *Bulletin of the Polytechnic Institute of Jassy (Construction, Architecture Section)*, 58(62), 2, 21-28.

Ronoh, E.K. and Rath, T. (2015a). Modelling of longwave radiation exchange at greenhouse surfaces under all-sky conditions. *Agricultural Engineering International: CIGR Journal*, 17(4), 23-35.

Ronoh, E.K. and Rath, T. (2015b). Effects of greenhouse surface inclination and orientation on longwave radiation exchange. *DGG & BHGL 50th Horticultural Science Conference and International WeGa Symposium*. Freising-Weihenstephan, Germany, 24th–28th February 2015. BHGL Tagungsband 31, ISSN 1613-088X, p. 127.

Ronoh, E.K., Langner, F. and Rath, T. (2015). Significance of convective and radiative heat transfer coefficients in U_{cs}-value at glass-covered greenhouse surfaces. *DGG & BHGL 50th Horticultural Science Conference and International WeGa Symposium*. Freising-Weihenstephan, Germany, 24th–28th February 2015. BHGL Tagungsband 31, ISSN 1613-088X, p. 126.

Ronoh, E.K. and Rath, T. (2014). Investigations on the external thermal radiation exchanges between the glass-covered greenhouse surfaces and the sky. *DGG-Proceedings*, 4(6), 1-5. DOI: 10.5288/dgg-pr-04-06-er-2014.

Roy, J.C., Boulard, T., Kittas, C., Wang, S. (2002). Convective and ventilation transfers in greenhouses, Part 1: The greenhouse considered as a perfectly stirred tank. *Biosystems Engineering*, 83(1), 1-20.

Sahin, A.D. and Sen, Z. (2008). Solar irradiation estimation methods from sunshine and cloud cover data. Chapter 6, In: Badescu, V. (Ed.), *Modeling solar radiation at the earth's surface: Recent advances*. Springer-Verlag Berlin Heidelberg, pp. 145-149.

Saltelli, A., Annoni, P., Azzini, I., Campolongo, F., Ratto, M. and Tarantola, S. (2010). Variance based sensitivity analysis of model output: Design and estimator for the total sensitivity index. *Computer Physics Communications*, 181(2), 259-270.

Saltelli, A., Tarantola, S., Campolongo, F. and Ratto, M. (2004). *Sensitivity analysis in practice: A guide to assessing scientific models*. John Wiley & Sons Ltd, West Sussex, England, pp. 1-219.

Sanford, S. (2011). *Reducing greenhouse energy consumption: An overview*. Energy Efficiency in Greenhouses, Series A3907-01, Madison, WI, USA. Available at: http://www.learningstore.uwex.edu. Accessed on 12th November 2014.

Sawhney, G.S. (2010). *Heat and mass transfer*. 2nd Edition, I.K. International Publishing House Pvt. Ltd., New Delhi, India.

Scharmer, K. and Greif, J. (2000). *European Solar Radiation Atlas: Fundamentals and maps*. Ecole des Mines de Paris, Paris, France.

Sedlar, J. and Hock, R. (2009). Testing longwave radiation parameterizations under clear and overcast skies at Storglaciären, Sweden. *The Cryosphere*, 3(1), 75-84.

Shamim, M.A., Remesan, R., Bray, M. and Han, D. (2015). An improved technique for global solar radiation estimation using numerical weather prediction. *Journal of Atmospheric and Solar-Terrestrial Physics*, 129, 13-22.

Sharma, A.K., Velusamy, K. and Balaji, C. (2008). Interaction of turbulent natural convection and surface thermal radiation in inclined square enclosures. *Heat and Mass Transfer*, 44(10), 1153-1170.

Sharples, S. (1984). Full-scale measurements of convective energy losses from exterior building surfaces. *Building Environment*, 19(1), 31-39.

Sicart, J.E., Pomeroy, J.W., Essery, R.L.H. and Bewley, D. (2006). Incoming longwave radiation to melting snow: Observations, sensitivity and estimation in Northern environments. *Hydrological Processes*, 20(17), 3697-3708.

Sparrow, E.M. and Cess, R.D. (1967). *Radiation heat transfer*. Brooks/Cole Publishing Company, Belmont, California, USA, pp. 32-33.

Sridhar, V. and Elliott, R. L. (2002). On the development of a simple downwelling longwave radiation scheme. *Agricultural and Forest Meteorology*, 112(3-4), 237-243.

Staley, D.O. and Jurica, G.M. (1972). Effective atmospheric emissivity under clear skies. *Journal of Applied Meteorology*, 11(2), 349-356.

Sugita, M. and Brutsaert, W. (1993). Cloud effect in the estimation of instantaneous downward longwave radiation. *Water Resources Research*, 29(3), 599-605.

Suhardiyanto, H. and Romdhonah, Y. (2008). Determination of convective coefficient at the outside cover of a monitor greenhouse in Indonesia. *Journal of Applied Sciences in Environmental Sanitation*, 3(1), 37-46.

Sukhatme, S.P. (2003). *Solar energy: Principles of thermal collection and storage*. 2nd Edition, Tata McGraw-Hill Publishing, New Delhi.

Svensson, M.K. (2004). Sky view factor analysis – implications for urban air temperature differences. *Meteorological Applications*, 11(3), 201-211.

Swinbank, W.C. (1963). Longwave radiation from clear skies. *Quarterly Journal of the Royal Meteorological Society*, 89(381), 339-348.

Taha, A.T.H. (2003). Simulation model of energy fluxes in passive solar greenhouses with a concrete north-wall. PhD Thesis, *Gartenbautechnische Informationen*, Heft 57, Gottfried Wilhelm Leibniz Universität Hannover, Germany.

Tang, B.H. and Li, Z.L. (2008). Estimation of instantaneous net surface longwave radiation from MODIS cloud-free data. *Remote Sensing of Environment*, 112(9), 3482-3492.

Tantau, H.-J. (2013). Heat requirement of greenhouse including latent heat flux. *Landtechnik*, 68(1), 43-49.

Tantau, H.-J. (1983). *Heizungsanlage im Gartenbau (Heating systems in horticulture)*. In: Handbuch des Erwerbgärtners. Ulmer, Stuttgart, pp. 245-252.

Tantau, H.-J. (1975). Der Einfluß von Einfach- und Doppelbedachungen auf das Klima und den Wärmehaushalt von Gewächshäusern. PhD Thesis, *Gartenbautechnische Informationen*, Heft 4, Universität Hannover.

Tsirogiannis, I.L. (1996). *Greenhouse types in Greece; causes of damage and failure*. Diploma thesis, Dept. of Agricultural Engineering, Agricultural University of Athens, Athens, Greece (in Greek).

Twidell, J. and Weir, T. (2005). *Renewable energy resources*. 2nd Edition, Taylor & Francis, New York, USA, 624 pp.

Vadivambal, R. and Jayas, D.S. (2011). Applications of thermal imaging in agriculture and food industry – a review. *Food and Bioprocess Technology*, 4(2), 186-199.

Van de Braak, N.J. (1995). Greenhouse construction and equipment. Chapter 4.2, In: Bakker, J.C., Bot, G.P.A., Challa, H. and Van de Braak, N.J. (Eds.), *Greenhouse climate control: An integrated approach*. Wageningen Pers, Wageningen, The Netherlands, pp. 161-170.

Van der Veen, S.H. (2013). Improving NWP model cloud forecasts using meteosat second-generation imagery. *Monthly Weather Review*, 141(5), 1545-1557.

Van Thanh, T. (1973). *Thermal radiation exchange between the sun and sky, and the earth*. Thesis, University of Canterbury, Christchurch, New Zealand.

Varioscan Manual (2000). *Varioscan high resolution: Models 3021, 3021-ST and 3022*. Jenoptik Laser, Optik, Systeme GmbH, Jena, Germany.

Viúdez-Mora, A. (2011). *Atmospheric downwelling longwave radiation at the surface during cloudless and overcast conditions: Measurements and modeling*. PhD Thesis, Universitat de Girona, Spain. ISBN: 978-84-694-5001-7.

Voigtländer, J., Tuch, T., Birmili, W. and Wiedensohler, A. (2006). Correlation between traffic density and particle size distribution in a street canyon and the dependence on wind direction. *Atmospheric Chemistry and Physics*, 6(12), 4275-4286.

Vollebregt, H.J.M. and van de Braak, N.J. (1995). Analysis of radiative and convective heat exchange at greenhouse walls. *Journal of Agricultural Engineering Research*, 60(2), 99-106.

Von Elsner, B., Briassoulis, D., Waaijenberg, D., Mistriotis, A., von Zabeltitz, C., Gratraud, J., Russo, G. and Suay-Cortes, R. (2000). Review of structural and functional characteristics of greenhouses in European Union countries, Part II: Typical designs. *Journal of Agricultural Engineering Research*, 75(2), 111-126.

Von Elsner, B. (2006). Interference pigments in photo selective shading paint for greenhouses. *Acta Horticulturae*, 711, 417-422.

Von Elsner, B. (1982). Das Kleinklima und der Wärmeverbrauch von geschlossenen Gewächshäusern: Ein Simulationsmodell zur gartenbautechnischen Bewertung unter Berücksichtigung des Einflusses von Standortklima, Pflanzenbestand und Gewächshauskonstruktion. PhD Thesis, *Gartenbautechnische Informationen*, Heft 12, Institut für Technik in Gartenbau und Landwirtschaft, Universität Hannover, Germany.

Von Zabeltitz, C. (2011). *Integrated greenhouse systems for mild climates*. Springer-Verlag Berlin Heidelberg, Germany.

Von Zabeltitz, C. (1986). *Gewächshäuser: Planung und Bau*. Ulmer Verlag, Stuttgart, Germany, p. 182.

Vukicevic, T., Greenwald, T., Zupanski, M., Zupanski, D., Vonder Haar, T. and Jones, A.S. (2004): Mesoscale cloud state estimation from visible and infrared satellite radiances. *Monthly Weather Review*, 132(12), 3066-3077.

Walton, G.N. (1983). *Thermal analysis research program reference manual*. NBSSIR 83-2655. National Bureau of Standards.

Wang, W., Liang, S. and Augustine, J.A. (2009). Estimating high spatial resolution clear-sky land surface upwelling longwave radiation from MODIS data. *IEEE Transactions on Geoscience and Remote Sensing*, 47(5), 1559-1570.

Weather Online (WetterOnline). *Weather maps - clouds, rain and snow at a glance*. Available at: http://www.wetteronline.de. Accessed on 9th July 2013.

Wong, L.T. and Chow, W.K. (2001). Solar radiation model. *Applied Energy*, 69(3), 191-224.

Worley, J. (2014). *Greenhouses: heating, cooling and ventilation*. Bulletin 792, College of Agricultural and Environmental sciences, The University of Georgia, USA. Available at: http://extension.uga.edu/publications/detail.cfm?number=B792. Accessed on 12th April 2015.

Wu, H., Zhang, X., Liang, S., Yang, H. and Zhou, G. (2012). Estimation of clear-sky land surface longwave radiation from MODIS data products by merging multiple models. *Journal of Geophysical Research*, 117(D22107), 1-15.

Yang, Y., Li, G. and Tang, R. (2012). On the estimation of daily beam radiation on tilted surfaces. *Energy Procedia*, 16(C), 1570-1578.

Yang, K., He, J., Tang, W., Qin, J. and Cheng, C.C.K. (2010). On downward shortwave and longwave radiations over high altitude regions: Observation and modeling in the Tibetan Plateau. *Agricultural and Forest Meteorology*, 150(1), 38-46.

APPENDICES

A: Physics of Radiation

Basics

Radiation transfer is one of the three modes of transferring thermal energy. Conduction and convection energy transfer are significantly different from radiation transfer at macroscales, where dimensions are much larger than those for atoms and molecules. At atomic levels, these three phenomena have similar equations based on statistical thermodynamics (Howell et al., 2011). Radiative energy is transmitted between the distant elements without requiring a medium between them. The concept for radiation is that all materials are constantly emitting infrared radiation that is absorbed by other materials. Thermal radiation is the electronic radiation emitted by a body due to its temperature. The radiant of the thermal radiation is therefore temperature-dependent. The thermal radiation is confined to the infrared, visible, and ultraviolet regions (wavelength: 100 nm to 100000 nm) of the electromagnetic spectrum (Howell et al., 2011; Bahrami, 2005).

Radiation is mostly important when the radiating surface is at a higher temperature than the receiving object. Apart from temperature, the heat transferred into or out of an object by thermal radiation is a function of other several components. These include its surface reflectivity, emissivity, surface area, and geometric orientation with respect to other thermally participating objects. In turn, an object's surface reflectivity and emissivity is a function of its surface conditions (roughness, finish, etc.) and composition. Like light, heat radiation follows a straight line and is either reflected, transmitted or absorbed upon striking an object. Radiant energy must be absorbed to be converted to heat (Worley, 2014). Radiation heat transfer between surfaces depends on the orientation of the surfaces relative to each other as well as their radiation properties and temperatures. A view factor (or shape factor) is a purely geometrical parameter that accounts for the effects of orientation on radiation between surfaces (Bahrami, 2005). The view factor ranges between 0 and 1. If only two surfaces are involved, radiating and absorbing from each other with an emissivity ε equal to 1, the net flux density Q_{rad} from the surface with temperature T_1 to that with T_2 will be the difference between emitted and absorbed radiation given by (Vollebregt and van de Braak, 1995):

$$Q_{rad} = \varepsilon \cdot \sigma \cdot A_s \cdot F \cdot \left(T_1{}^4 - T_2{}^4 \right) \qquad\qquad\qquad \text{(A-1)}$$

where,

Q_{rad}	: net flux density from the surface	[W m^{-2}]
ε	: emissivity (ε = 1 for a blackbody)	[-]
σ	: Stefan-Boltzmann constant = $5.67 \cdot 10^{-8}$	[W m^{-2} K^{-4}]
A_s	: total surface area	[m^2]
F	: geometrical factor	[-]
T_1	: absolute temperature of surface 1	[K]
T_2	: absolute temperature of surface 2	[K]

Thermal Radiation Properties at Interfaces

The radiative behaviour of a real body depends on many factors such as composition, surface finish, temperature, radiation wavelength, opacity, angle at which radiation is either emitted or intercepted, and spectral distribution of the incident radiation. To describe this radiative behaviour relative to blackbody behaviour, the spectral, directional, or averaged emissive, absorptive, and reflective properties are needed (Howell et al., 2011; Sparrow and Cess, 1967).

a) Emission

Every material at finite temperature emits radiative energy. In principle, emission is directional in nature, and is a function of the local material properties and temperature. An ideal body would emit the maximum amount of energy uniformly in all directions and at each wavelength interval (Howell et al., 2011). Emissivity indicates how efficiently the surface emits energy relative to a black body (no reflection) and it ranges between 0 and 1. The emissivity of a real surface varies as a function of the surface temperature, the wavelength, and the direction of the emitted radiation. According to Howell et al. (2011), the emissivity values averaged with respect to all wavelengths are termed *total* quantities; averages with respect to all directions are termed *hemispherical* quantities.

The fundamental emissivity of a surface at a given temperature is the spectral directional emissivity, which is defined as the ratio of the intensity of radiation emitted by the surface

at a specified wavelength and direction (Q_λ) to that emitted by a blackbody under the same conditions (Q_λ^*). The wavelength-dependent emissivity (ε_λ) is simply expressed as (Howell et al., 2011):

$$\varepsilon_\lambda = \frac{Q_\lambda}{Q_\lambda^*}$$ (A-2)

where,

      ε_λ : wavelength-dependent emissivity   [-]

      Q_λ : radiation emitted by the surface at a specific wavelength   [W m^{-2}]

      Q_λ^* : blackbody radiation emitted at a specific wavelength   [W m^{-2}]

The total directional emissivity is defined in the same fashion by using the total intensities integrated over all wavelengths. In practice a more convenient method is used, hemispherical properties. These properties are spectrally and directionally averaged. The emissivity of a surface at a specified wavelength may vary as temperature changes since the spectral distribution of emitted radiation changes with temperature. Finally the total hemispherical emissivity is defined in terms of the radiation energy emitted over all wavelengths in all directions (Cengel, 2007; Edwards, 1981). In a greenhouse, the various surfaces of the different components (crop leaves, cover, soil surface and heating pipes) are at an absolute temperature of about 300 K. The surfaces then emit thermal radiation with a wavelength ranging from 5000 nm to 50000 nm and absorb radiation emitted in the same wavelength from the other surfaces (Bakker et al., 1995). If the emissivities are not equal to 1, multiple reflections between surfaces will occur. The effective emissivity ε_{12} between the surfaces depends on the individual emissivities ε_1 and ε_2 and the geometry of the surfaces. For large parallel surfaces a relatively simple relation is expressed by (Howell et al., 2011):

$$\varepsilon_{12} = \left(\frac{1}{\varepsilon_1} + \frac{1}{\varepsilon_2} - 1 \right)^{-1}$$ (A-3)

where,

      ε_{12} : effective emissivity between the surfaces   [-]

      ε_1 : emissivity of surface 1   [-]

      ε_2 : emissivity of surface 2   [-]

b) Absorptivity

The absorptivity is defined as the fraction of the energy incident on a body that is absorbed by the body. The incident radiation depends on the radiative conditions (spectral intensity) at the source of the incident energy. The spectral distribution of the incident radiation is independent of the temperature or physical nature of the absorbing surface unless radiation emitted from the surface is partially reflected from the source or surrounding back to the surface. A blackbody absorbs all the electromagnetic radiation incident on it and thus the absorptivity is equal to the emissivity. Compared with emissivity, the absorptivity has additional complexities because directional and spectral characteristics of the incident radiation must be included along with the absorbing surface temperature (Howell et al., 2011).

c) Reflectivity

Reflectance is the fraction of incident electromagnetic power that is reflected at an interface. The reflective properties of a surface are more complicated to specify than the emissivity or absorptivity. This is because reflected energy depends not only on the angle at which the incident energy impinges on the surfaces but also on the direction being considered for the reflected energy (Howell et al., 2011). Real surfaces reflect part of the incident radiation which can be measured by a radiometer, first measuring the irradiance (radiant flux incident on the surface by unit area) and thence the radiance (radiant flux exiting the surface by unit area and unit solid angle). For opaque surfaces, what is absorbed is reflected while transparent surfaces reflect a small fraction of incident radiation due to the difference in refractive index. Reflection at real surfaces always has some scattering. In general, the scattering process occurs when the particles (material or electromagnetic) travelling along a given direction are deflected as a result of collision with other particles.

d) Transmissivity

Transmittance at an interface is the fraction of incident radiation energy that propagates to the rear of the interface. The transmissivity of radiation across an interface depends on the angle of incidence on the interface, the direction at which the radiation is transmitted after crossing the surface, and the wavelength of the radiation. Generally for opaque

surfaces, the transmissivity across a surface of the material is not needed in radiative transfer calculations (Howell et al., 2011). An energy balance indicates that, at any interface, absorption plus reflectance plus transmittance must equal unity.

Radiation Laws

Everything radiates and absorbs electromagnetic radiation. All objects above the temperature of absolute zero (-273.15 °C) radiate energy to their surrounding environment (Pidwirny, 2006). The radiation laws apply when the radiating body is a blackbody radiator.

1) Planck's law

The law describes the amount of radiation emitted by a blackbody at each wavelength as a function of temperature. The monochromatic irradiance is expressed as (Burke, 1996):

$$Q_\lambda^* = \frac{C_1}{\lambda^5 \cdot \left(\exp\left(\dfrac{C_2}{\lambda \cdot T} \right) - 1 \right)} \tag{A-4}$$

where,

Q_λ^*	: blackbody radiation	[W m^{-2}]
λ	: wavelength	[m]
T	: absolute temperature	[K]
C_1	: coefficient = 3.74 · 10^{-16} (Burke, 1996)	[W m^3]
C_2	: coefficient = 1.44 · 10^{-2} (Burke, 1996)	[m K]

In the case of Max Planck's concept or quantum theory, heat transfer in the form of photon or quanta of energy takes place from a body when its temperature is above absolute zero (Sawhney, 2010). The photon has energy expressed as:

$$Q_p = h \cdot f \tag{A-5}$$

where,

Q_p	: energy of a photon	[J]
h	: Planck's constant = 6.626 · 10^{-34}	[J s]
f	: frequency of photon	[s^{-1}]

2) Stefan-Boltzmann law

The total amount of radiant energy emitted by a blackbody is proportional to the fourth power of the absolute temperature such that (Howell et al., 2011):

$$Q^* = \sigma \cdot T^4 \qquad (A-6)$$

where,

Q^* : amount of radiation emitted by a blackbody [W m^{-2}]

σ : Stefan-Boltzmann constant = 5.67 · 10^{-8} [W m^{-2} K^{-4}]

T : absolute temperature   [K]

3) Wien's displacement law

A useful quantity is the wavelength (λ_{max}) at which the blackbody intensity is maximum for a given temperature. This maximum shifts toward shorter wavelengths at the temperature is increased. The law shows that there is a wide separation between solar radiation (shortwave) and terrestrial radiation (longwave). The value of $\lambda_{max} \cdot T$ is at the peak of the spectral distribution curve and is obtained by differentiating Planck's distribution with respect to λT (Howell et al., 2011). Its solution is a constant (approximately 3000 µm K) and is given by (Howell et al., 2011):

$$\lambda_{max} = \frac{x_\lambda}{T} \qquad (A-7)$$

where,

λ_{max} : maximum wavelength   [µm]

x_λ : coefficient = 2897 (Howell et al., 2011)   [µm K]

T : absolute temperature   [K]

4) Kirchhoff's law

The law relates the emitting and absorbing abilities of a body (Howell et al., 2011). Materials that are strong emitters at a particular wavelength are also strong absorbers at that wavelength such that:

$$\varepsilon_\lambda = \alpha_\lambda \qquad (A-8)$$

where,

ε_λ : emissivity at a particular wavelength   [-]

α_λ : absorptivity at a given wavelength   [-]

5) Lambert's cosine law

The law holds that the radiation per unit solid angle (the radiant intensity) from a flat surface varies with the cosine of the angle to the surface normal. Such a surface has the same radiance when viewed from any angle. When an area element is radiating as a result of being illuminated by an external source, the irradiance landing on that area element will be proportional to the cosine of the angle between the illuminating source and the normal. Thus, the radiation emitted from the surface at a given angle is given by (IESNA, 2000):

$$Q_\theta = Q_n \cdot \cos \theta \qquad \text{(A-9)}$$

where,

Q_θ	: emitted radiation at an angle θ	[W m^{-2}]
Q_n	: emitted radiation normal to the surface	[W m^{-2}]
θ	: angle of incidence	[°]

A surface which obeys Lambert's law is said to be Lambertian, and exhibits Lambertian reflectance. The emission of a Lambertian radiator does not depend upon the amount of incident radiation, but rather from radiation originating in the emitting body itself. A blackbody is an example of a Lambertian radiator. The measurement of the radiation falling on a surface (also known as irradiance or radiative flux) is based on two assumptions: (a) the sensor surface is spectrally black - i.e. that it absorbs all radiation from all wavelengths, and (b) that it has a true field of view of 180°. These two properties, taken together, with which the net radiometer needs to comply, are generally known as the 'cosine response'. A perfect cosine response will show maximum sensitivity at an angle of incidence of 0° (perpendicular to the sensor surface) and zero sensitivity at an angle of incidence of 90° (radiation passing over the sensor surface). At any angle between 0° and 90° the sensitivity should be proportional to the cosine of the angle of incidence. It is important that radiation sensors (such as net radiometers) closely approximate this ideal cosine response in order to avoid a biased estimate of irradiance (Jones et al., 2003).

B: Tables

Table B1. Cosine correction factors for the Gill UVW anemometer.

COSINE CORRECTION FACTORS FOR MODEL 08254 AND MODEL 08274 PROPELLERS
Corrections are indexed as a function of the cosine of the angle between the propeller axis and the wind vector.

COS	08254	08274	COS	08254	08274	COS	08254	08274	COS	08254	08274
-1.00	1.05	1.04	-0.50	1.21	1.26	0.00	1.00	1.00	0.50	1.25	1.32
-0.98	1.08	1.05	-0.48	1.20	1.26	0.02	1.00	1.00	0.52	1.25	1.31
-0.96	1.07	1.05	-0.46	1.19	1.25	0.04	1.03	1.09	0.54	1.26	1.30
-0.94	1.07	1.05	-0.44	1.17	1.25	0.06	1.13	1.46	0.56	1.26	1.29
-0.92	1.07	1.05	-0.42	1.16	1.25	0.08	1.18	1.62	0.58	1.26	1.28
-0.90	1.08	1.05	-0.40	1.15	1.26	0.10	1.18	1.55	0.60	1.25	1.27
-0.88	1.09	1.06	-0.38	1.15	1.27	0.12	1.18	1.52	0.62	1.25	1.26
-0.86	1.10	1.07	-0.36	1.14	1.28	0.14	1.18	1.51	0.64	1.24	1.25
-0.84	1.11	1.07	-0.34	1.13	1.29	0.16	1.18	1.51	0.66	1.23	1.22
-0.82	1.12	1.08	-0.32	1.12	1.29	0.18	1.18	1.51	0.68	1.22	1.20
-0.80	1.13	1.09	-0.30	1.11	1.29	0.20	1.18	1.50	0.70	1.21	1.18
-0.78	1.14	1.10	-0.28	1.09	1.28	0.22	1.18	1.50	0.72	1.20	1.16
-0.76	1.15	1.11	-0.26	1.08	1.29	0.24	1.17	1.50	0.74	1.18	1.14
-0.74	1.16	1.12	-0.24	1.06	1.30	0.26	1.19	1.49	0.76	1.17	1.12
-0.72	1.18	1.13	-0.22	1.04	1.29	0.28	1.22	1.47	0.78	1.15	1.10
-0.70	1.19	1.15	-0.20	1.02	1.27	0.30	1.24	1.46	0.80	1.13	1.09
-0.68	1.20	1.16	-0.18	1.00	1.24	0.32	1.27	1.48	0.82	1.11	1.08
-0.66	1.21	1.18	-0.16	0.96	1.22	0.34	1.32	1.50	0.84	1.10	1.07
-0.64	1.22	1.19	-0.14	0.92	1.19	0.36	1.32	1.49	0.86	1.08	1.06
-0.62	1.23	1.21	-0.12	0.89	1.16	0.38	1.31	1.47	0.88	1.07	1.05
-0.60	1.23	1.23	-0.10	0.86	1.12	0.40	1.31	1.44	0.90	1.05	1.04
-0.58	1.24	1.24	-0.08	0.83	1.06	0.42	1.30	1.42	0.92	1.04	1.03
-0.56	1.24	1.25	-0.06	0.82	1.00	0.44	1.29	1.40	0.94	1.03	1.02
-0.54	1.23	1.25	-0.04	0.82	0.94	0.46	1.28	1.37	0.96	1.02	1.02
-0.52	1.22	1.26	-0.02	0.90	0.96	0.48	1.26	1.34	0.98	1.01	1.01
									1.00	1.00	1.00

COSINE CORRECTION ALGORITHM

The algorithm begins by applying wind tunnel derived correction factors to the uncorrected UVW values. Using the most recently corrected UVW values, the magnitude of the resultant vector and the cosine of its angle relative to each axis is calculated. The cosine is used as an index to look up a new correction factor. This process continues until two successive sets of cosine values do not change by more than 0.02 or six iterations have occurred.

Since the correction for each wind component is a function of the angle between the propeller axis and the wind vector and since the correct wind vector may have an orientation different than that of the uncorrected wind vector, an iterative scheme must be used until the results converge.

```
void
correction( ) {
    n = 0;
    while (n<6) {
        u = raw_u * corrrection_factor[i];
        v = raw_v * correction_factor[j];
        w = raw_w * correction_factor[k];
        s = sqrt(u*u + v*v + w*w);

        ii = (int)(u * 50.0/s) + 50;
        jj = (int)(v * 50.0/s) + 50;
        kk = (int)(w * -50.0/s) + 50;     /* incoming w signal is neg for front flow */


        if (abs(ii-i)<2) {
            if (abs(jj-j)<2) {
                if (abs(kk-k)<2) break;
            }
        }

        n++;
        i=ii;
        j=jj;
        k=kk;
    }
}
```
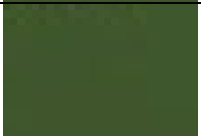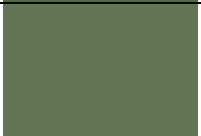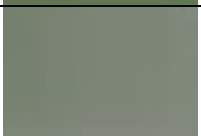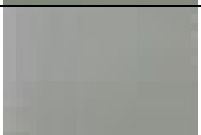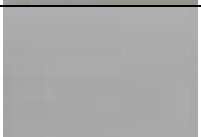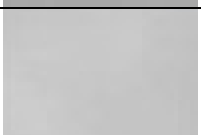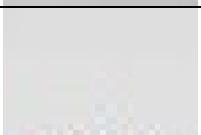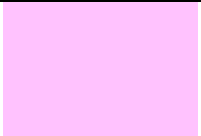
(Source: Manual PN 27005-90, 1994)

Table B2. Cloudiness factors derived from sample weather maps and octas.

Weather map*ᵃ	Average RGB values	Cloudiness factor (from analysed weather maps)	Cloudiness in octas*ᵇ	Cloudiness factor (from octas)
	(52, 77, 35)	0	0	0
	(59, 82, 36)	0.005	0	0
	(81, 112, 55)	0.091	1	0.125
	(100, 117, 85)	0.318	2	0.25
	(122, 130, 115)	0.405	3	0.375
	(147, 149, 144)	0.523	4	0.5
	(170, 170, 170)	0.609	5	0.625
	(199, 199, 199)	0.745	6	0.75
	(223, 223, 225)	0.864	7	0.875
	(43, 169, 253)	0.991	8	1
	(255, 194, 254)	0.995	8	1

*ᵃ Source: Weather radar from Weather Online (www.wetteronline.de)

*ᵇ Source: German Weather Service (www.dwd.de)

C: Figures

Fig. C1. Experimental setup for the net radiation measurement between two surfaces.

Fig. C2. Back of the CNR 4 with the connector for sensor outputs (left), the temperature connector (right) and the mounting rod (middle).
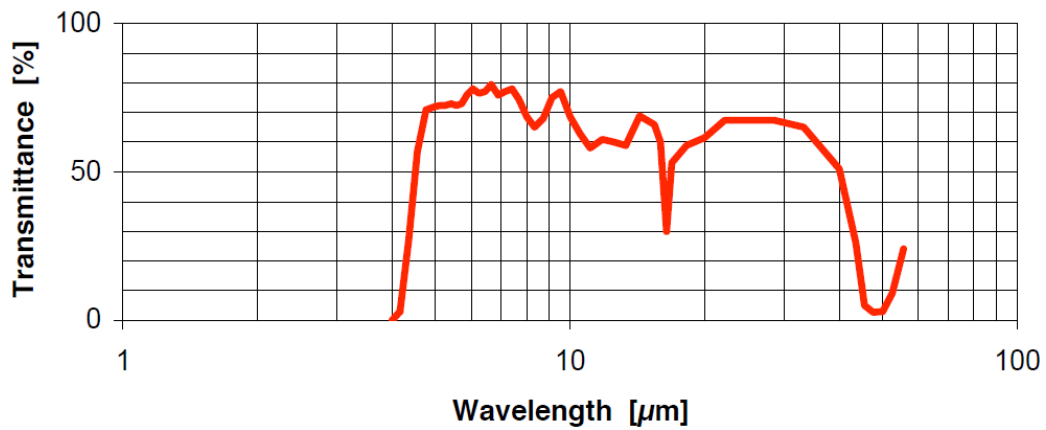

Fig. C3. The spectral sensitivity of the pyrgeometer window (Source: Kipp & Zonen, 2009).
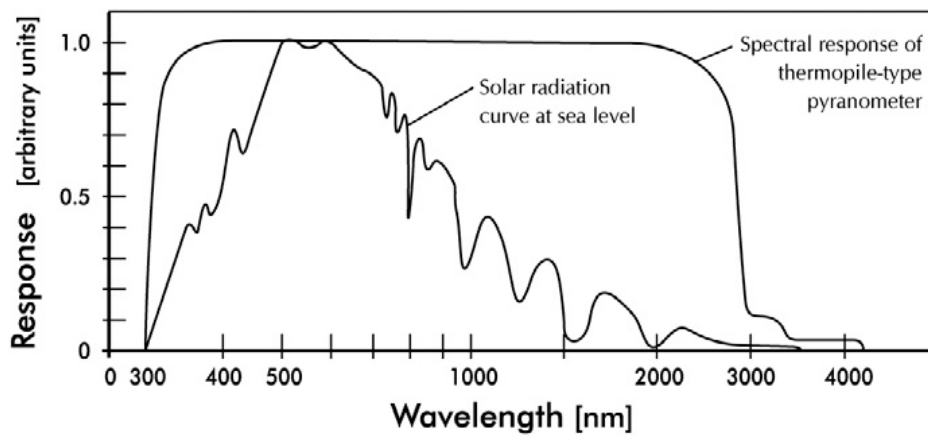

Fig. C4. The spectral sensitivity of the pyranometer in combination with the spectrum of the sun under a clear sky (Source: Kipp & Zonen, 2009).
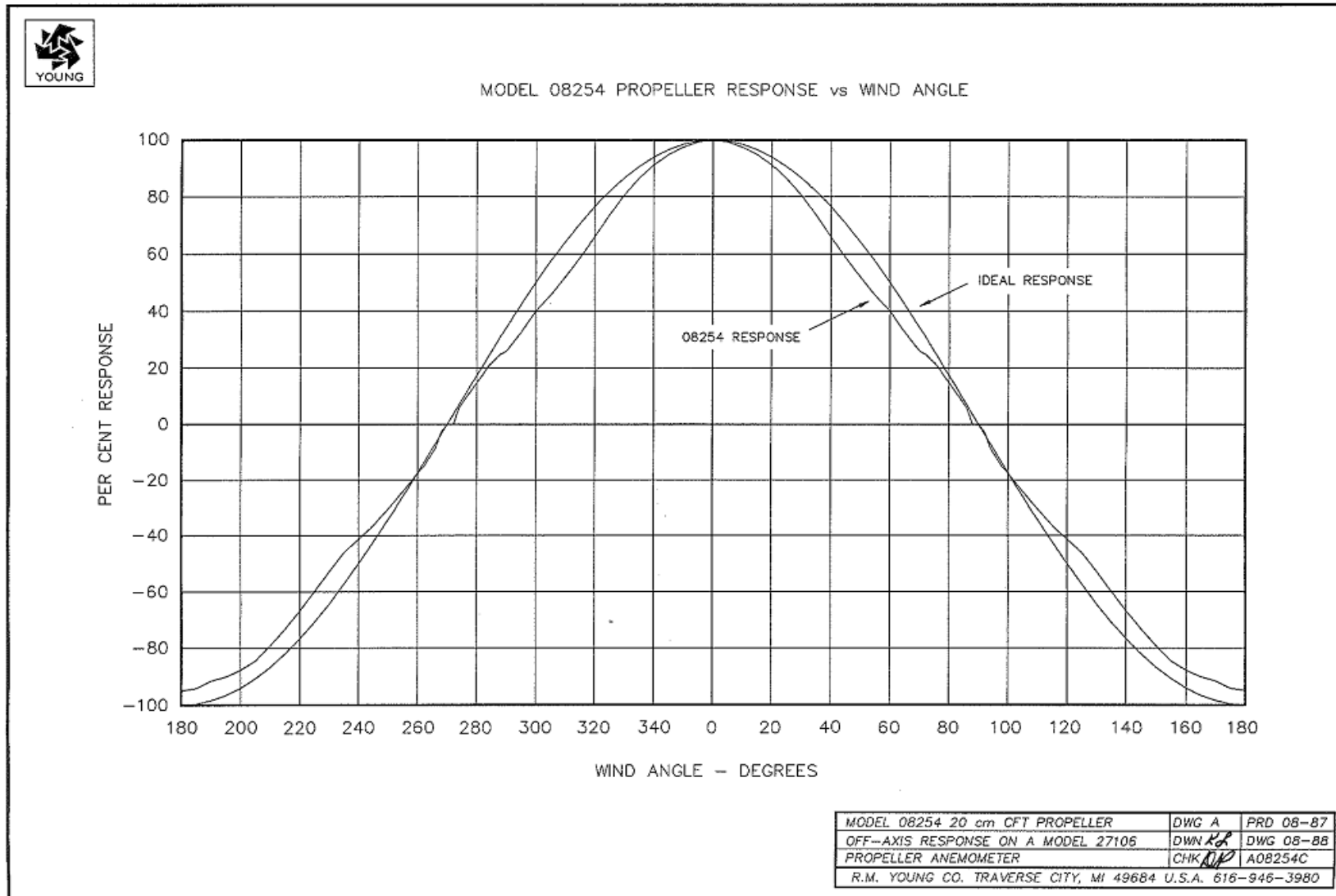
Fig. C5. The propeller response as a function of the wind angle (Source: Manual PN 27005-90, 1994).

Fig. C6. Setup for mounting the thermal camera above the thermal box: (a) Ladder, and

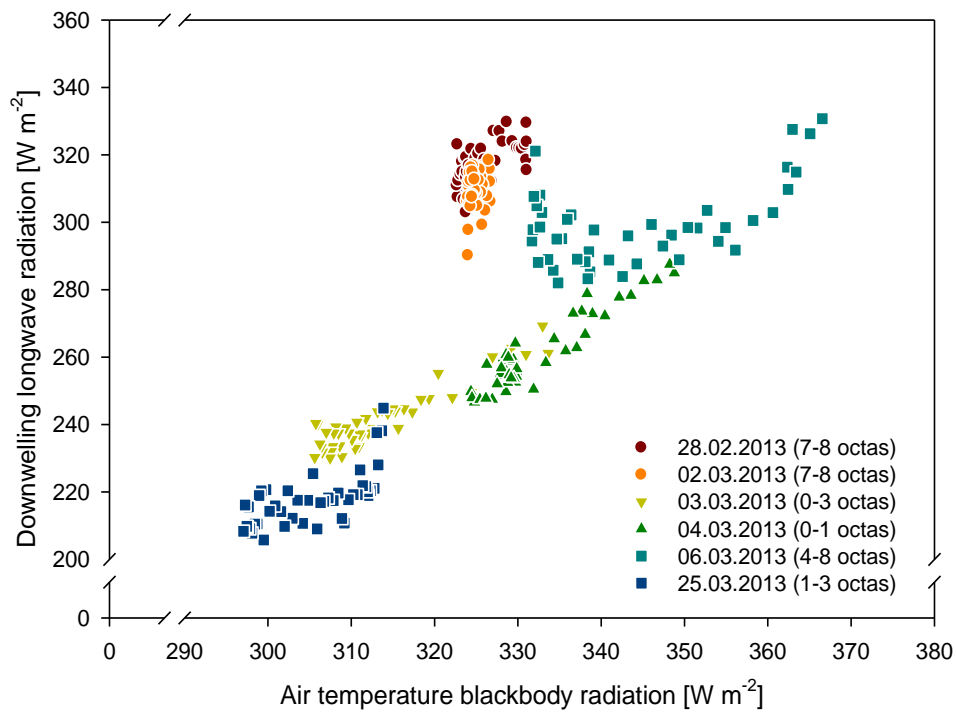(b) Hama air bulb remote control release for capturing images.

Fig. C7. Downwelling longwave radiation as a function of the sky condition and the air

temperature blackbody radiation (n = 45).

D: Halcon Algorithm for Vision-Based Analysis of Weather Maps

```
1    dev_close_window()
2    #* choose the right folder in the next command line
3    list_image_files ('C:/Users/EKR/Desktop/WetterMaps', 'default', [], ImageFiles)
4    i:=0
5    tuple_length(ImageFiles,length)
6    file:=ImageFiles[0]+'.txt'
7    open_file (file, 'append', FileHandle)
8    fwrite_string (FileHandle,
9    'year'+'\t'+'month'+'\t'+'day'+'\t'+'hour'+'\t'+'minute'+'\t'+'cloudiness1'+'\t'+'cloudiness2'+'\t'+'cloudiness3')
10   fnew_line(FileHandle)
11   close_file(FileHandle)
12   for i:=0 to length-1 by 1
13     read_image(Image,ImageFiles[i])
14     get_image_pointer1(Image,Pointer,Type,Width,Height)
15     dev_open_window (0,0,Width/3, Height/3, 'black', WindowHandle)
16     dev_display (Image)
17     gen_rectangle1 (Rectangle1, 472, 699, 473, 701)
18     gen_rectangle1 (Rectangle2, 482, 695, 483, 697)
19     gen_rectangle1 (Rectangle3, 483, 703, 485, 705)
20     access_channel (Image, Image1, 3)
21     gray_features (Rectangle1, Image1, 'mean', Value1)
22     gray_features (Rectangle2, Image1, 'mean', Value2)
23     gray_features (Rectangle3, Image1, 'mean', Value3)
24     cloudiness1:=(Value1-35)/(255-35)
25     cloudiness2:=(Value2-35)/(255-35)
26     cloudiness3:=(Value3-35)/(255-35)
27     tuple_strrstr (ImageFiles[i],'.jpg', Position)
28     tuple_str_first_n (ImageFiles[i], Position-1, imgname1)
29     tuple_str_last_n (imgname1, Position-2, minute)
30     tuple_str_first_n (ImageFiles[i], Position-3, imgname2)
31     tuple_str_last_n (imgname2, Position-4, hour)
32     tuple_str_first_n (ImageFiles[i], Position-5, imgname3)
33     tuple_str_last_n (imgname3, Position-6, day)
34     tuple_str_first_n (ImageFiles[i], Position-7, imgname4)
35     tuple_str_last_n (imgname4, Position-8, month)
36     tuple_str_first_n (ImageFiles[i], Position-9, imgname5)
37     tuple_str_last_n (imgname5, Position-10, year)
38     open_file (file, 'append', FileHandle)
39     fwrite_string (FileHandle, year+'\t')
40     fwrite_string (FileHandle, month+'\t')
41     fwrite_string (FileHandle, day+'\t')
42     fwrite_string (FileHandle, hour+'\t')
43     fwrite_string (FileHandle, minute+'\t')
44     fwrite_string (FileHandle, cloudiness1+'\t')
45     fwrite_string (FileHandle, cloudiness2+'\t')
46     fwrite_string (FileHandle, cloudiness3)
47     fnew_line (FileHandle)
48     close_file (FileHandle)
49     dev_close_window ()
50   endfor
```

Curriculum Vitae

Personal data

Name   Erick Kiplangat Ronoh

Date of birth   20.06.1982

Place of birth Sotik, Kenya

Marital status Married, 1 child

Education

04/2012 – 06/2016 Gottfried Wilhelm Leibniz Universität Hannover, Biosystems Engineering Section, Hannover, Germany: PhD studies (Dr. rer. hort)

09/2007 – 05/2010 Jomo Kenyatta University of Agriculture and Technology (JKUAT), Juja, Kenya: M.Sc. Agricultural Processing Engineering

04/2001 – 04/2006 JKUAT, Juja, Kenya: B.Sc. Agricultural Engineering

02/1996 – 11/1999 Koiwa High School, Litein, Kenya: KCSE

01/1987 – 11/1995 Tembwo Primary School, Sotik, Kenya: KCPE

Awards

02/2015   BHGL poster prize for young researchers (position 2), 50th Horticultural Science Conference (DGG, BHGL & WeGa), TU München and HS Weihenstephan-Triesdorf, Freising, Germany, 24th–28th February 2015

04/2012 – 12/2015 PhD joint scholarship framework between the National Commission for Science, Technology and Innovation (NACOSTI), Kenya and the German Academic Exchange Service (DAAD), Germany

09/2008 – 08/2009 In-country scholarship (DAAD)

10/2002 – 02/2006 Babaroa Trust awards of academic excellence (2001/2002–2004/2005)

Work experience

11/2010 – Date Assistant Lecturer, Biomechanical and Environmental Engineering Department (BEED), JKUAT, Juja, Kenya (study leave: 2012 – 2016)

04/2012 – 06/2016 Research Associate, Biosystems Engineering Section, Leibniz Universität Hannover, Germany

06/2007 – 11/2010 Teaching Assistant, BEED, JKUAT, Juja, Kenya

05/2007 – 06/2007 Field Assistant, Arroket Estate, Sotik Tea Company Limited, Sotik, Kenya

09/2006 – 03/2007 Sales Executive, G. North & Son Limited, Nairobi, Kenya

Lebenslauf

Persönliche Daten

Name   Erick Kiplangat Ronoh

Geboren am   20.06.1982

Gerburtsort   Sotik, Kenia

Familienstand   verheiratet, 1 Kind

Ausbildung

04/2012 – 06/2016   Gottfried Wilhelm Leibniz Universität Hannover, Abteilung Biosystem-technik, Hannover, Deutschland: Promotionsstudium (Dr. rer. hort)

09/2007 – 05/2010   Jomo Kenyatta University of Agriculture and Technology (JKUAT), Juja, Kenia: M.Sc. Agrarwissenschaftliche Verfahrenstechnik

04/2001 – 04/2006   JKUAT, Juja, Kenia: B.Sc. Agrartechnik

02/1996 – 11/1999   Koiwa High School, Litein, Kenia: KCSE

01/1987 – 11/1995   Tembwo Primary School, Sotik, Kenia: KCPE

Auszeichnungen

02/2015   BHGL-Posterpreis für Nachwuchswissenschaftler (Platz 2), 50. Garten-bauwissenschaftliche Tagung (DGG, BHGL & WeGa), TU München und HS Weihenstephan-Triesdorf, Freising, Deutschland, 24.–28.02.2015

04/2012 – 12/2015   PhD Stipendium – Kooperation der Nationalen Kommission für Wissenschaft, Technologie und Innovation (NACOSTI), Kenia and dem Deutschen Akademischen Austausch Dienst (DAAD), Deutschland

09/2008 – 08/2009   Stipendium (DAAD)

10/2002 – 02/2006   Babaroa Trust Auszeichnungen für akademische Exzellenz (für den Zeitraum 2001/2002 – 2004/2005)

Berufliche Tätigkeit

Seit 11/2010   Juniordozent, Biomechanical and Environmental Engineering Department (BEED), JKUAT, Juja, Kenia (freigestellt: 2012 – 2016)

04/2012 – 06/2016   wissenschaftlicher Mitarbeiter, Abteilung Biosystemtechnik, Leibniz Universität Hannover, Deutschland

06/2007 – 11/2010   Lehrauftrag, BEED, JKUAT, Juja, Kenia

05/2007 – 06/2007   Assistent, Arroket Estate, Sotik Tea Company Limited, Sotik, Kenia

09/2006 – 03/2007   Verkaufsleiter, G. North & Son Limited, Nairobi, Kenia

Publications Derived from this Work

<u>**Peer-Reviewed Papers**</u>

a) Journal

Ronoh, E.K. and Rath, T. (2015). Modelling of longwave radiation exchange at greenhouse surfaces under all-sky conditions. *Agricultural Engineering International: CIGR Journal*, 17(4), 23-35.

b) Proceedings

Ronoh, E.K. and Rath, T. (2014). Investigations on the external thermal radiation exchanges between the glass-covered greenhouse surfaces and the sky. *DGG-Proceedings*, 4(6): 1-5. DOI: 10.5288/dgg-pr-04-06-er-2014.

<u>**Conference Presentations**</u>

Ronoh, E.K., Langner, F. and Rath, T. (2015). Significance of convective and radiative heat transfer coefficients in U_{cs}-value at glass-covered greenhouse surfaces. DGG & BHGL 50th Horticultural Science Conference and International WeGa Symposium. Freising-Weihenstephan, Germany, 24th–28th February 2015. *BHGL Tagungsband* 31, ISSN 1613-088X, p. 126.

Ronoh, E.K. and Rath, T. (2015). Effects of greenhouse surface inclination and orientation on longwave radiation exchange. DGG & BHGL 50th Horticultural Science Conference and International WeGa Symposium. Freising-Weihenstephan, Germany, 24th–28th February 2015. *BHGL Tagungsband* 31, ISSN 1613-088X, p. 127.

Ronoh, E.K. and Rath, T. (2014). Vision-based estimation of cloudiness from weather maps for agricultural modelling. 20th Workshop Computer Image Analysis in Agriculture, Hochschule Osnabrück, Germany, 26th May 2014. *Bornimer Agrartechnische Berichte*, Heft 88, ISSN 0947-7314, p. 178.

Ronoh, E.K. and Rath, T. (2014). Investigations on the external thermal radiation exchanges between the glass-covered greenhouse surfaces and the sky. DGG & BHGL 49th Horticultural Science Conference, Dresden, Germany, 5th–8th March 2014. *BHGL Tagungsband* 30, ISSN 1613-088X, p. 128.

Acknowledgements

The objective spirit of academics has been my greatest admiration and I thank God for guiding me on this scientific path. I am delighted to have had the opportunity to explore a tiny bit of Him. It was an incredible experience that meant all the difference in my life.

This journey would have been impossible had I not received the unwavering guidance of Prof. Dr. Thomas Rath, my advisor (*Doktorvater*). I sincerely thank him for his advice, understanding, patience, and most importantly, his friendship during my studies at the Biosystems Engineering Section (BGT), Leibniz Universitat Hannover. I found his comments, suggestions, insights and knowledge very helpful in broadening my knowledge. Even after moving to his new workplace in 2013 (Biosystems Engineering Laboratory (BLab), Osnabrück University of Applied Sciences), he was always available whenever I needed his contributions. I am also very grateful to the doctoral committee and wish to thank Prof. Dr. Hartmut Stützel and Prof. Dr. Moritz Knoche for their engagement.

I am grateful to the joint scholarship framework between the German Academic Exchange Service (Deutscher Akademischer Austausch Dienst, DAAD, Germany) and the National Commission for Science, Technology and Innovation (NACOSTI, Kenya). It was a great honour to have been a recipient of this scholarship and I am thankful for all the financial and non-material support. Thanks too to my employer, Jomo Kenyatta University of Agriculture and Technology (JKUAT), for granting me a study leave that made it possible to fully engage in my research.

All friends and colleagues truly made the journey extremely enriching. Working as a team at the BGT reminded me of the fact that two heads are better than one. Special thanks to Dr. Stefanie Grade for her valuable support and cooperation in different ways during my studies. I am also grateful to Prof. a.D. Dr. Hans-Jürgen Tantau (retired) and Dr. -Ing. Bukhard von Elsner (retired) for their scientific advice. Thanks too to Bettina, Rita and Edda for their assistance at the BGT. I appreciate the fruitful consultations with former PhD colleagues (Julio, Sebastian, Holger, Christian and Anne) and the present team (Gökhan, Klaus, Serge, Sandra, Felix, Frederik, Johannes and Indera). Thanks Frederik for all the support and endless discussions we had while working together. My special thanks

go out to my office mate, Sandra, for her support in learning the ins and outs of the German society, culture and language. For the support in all technical matters, I thank the workshop team (Werner (retired), Andreas, Norbert and Niko). My sincere gratitude to the other BLab members (Maryam, Diedrich, Josef). I wish you all the best for the future.

Special thanks to Dipl. -Ing. Holger Schilke (Institute of Meteorology and Climatology (IMUK), Leibniz Universität Hannover) for his assistance in accessing the weather maps from Weather Online and providing other meteorological data. I am grateful as well to Ulrich Hering (Mechatronics Engineer, Vegetable Systems Modelling Section, Institute of Horticultural Production Systems) for his electrical skills and assistance. His ideas provided a solution to a challenging temperature regulation task in the data logging setup for one of my experiments. I also acknowledge the support I received from the Faculty of Architecture and Landscape Sciences, Leibniz Universität Hannover through Dr. Christian Brischke, Institute of Vocational Sciences in the Building Trade (IBW). He willingly facilitated acquisition of an appropriate space for my work at the rooftop of their building.

Life in Germany has taught me gamut of new things, punctuality and time management being the best examples. The concept of timeliness is deeply embedded in the German culture, and this is seen as a manifestation of a responsible nature. The German work culture is quite admiring as it helps in leading a more balanced life. Additionally, I enjoyed the liveliness of St. Maria Catholic church choir, Hannover and I thank all those amazing people from different countries who made this experience possible for me.

Another indispensable teammate was indeed my wife, Joyce. Needless to mention, this work would not have been realized without her support, encouragement and unwavering love. I have a full life to thank her and I plan to utilize every bit of it. Stefanie, my daughter, also supported our pursuits as a family and she kept reminding us of our enormous duties. Back in Kenya, my parents, family members and friends have played their special role in the most exemplary manner. Thanks all for your endless support and faith in me.

It would be a long list to mention all the other friends I am indebted to. I gratefully thank all of them.

Declaration / Erklärung zur Dissertation

Hiermit erkläre ich, dass ich meine Dissertation mit dem Titel „**Modelling of Thermal Radiation Exchange at Glass-Covered Greenhouse Surfaces under Different Climatic Conditions**" selbständig verfasst und die benutzten Hilfsmittel und Quellen sowie gegebenenfalls die zu Hilfsleistungen herangezogenen Institutionen vollständig angegeben habe. Die Dissertation wurde nicht schon als Masterarbeit, Diplomarbeit oder ähnliche Prüfungsarbeit verwendet.

Hannover, 2016

Erick Kiplangat Ronoh, M.Sc. (Kenia)